2015

Geomechanical Characterization of Marcellus Shale

Rafael Villamor Lora
University of Vermont

GEOMECHANICAL CHARACTERIZATION OF MARCELLUS SHALE.

A Thesis Presented

by

Rafael Villamor Lora

to

The Faculty of the Graduate College

of

The University of Vermont

In Partial Fullfillment of the Requirements
for the Degree of Master of Science
Specializing in Civil Engineering

October, 2015

Defense Date: May 15, 2015

Thesis Examination Committee:
Ehsan Ghazanfari, PhD., Advisor
Dryver R. Huston, Ph.D., Chairperson
George F. Pinder, Ph.D.
Mandar Dewoolkar, Ph.D.
Cynthia J. Forehand, Ph.D., Dean of the Graduate College

Abstract

Given their potential applications for a number of engineering purposes, the geomechanics of shale reservoirs is becoming one of the most important issues in modern geomechanics. Borehole stability modeling, geophysics, shale oil and shale gas reservoirs, and underground storage of CO_2 and nuclear waste are some of these potential applications to name a few. The growing interest in these reservoirs, as a source for hydrocarbons production, has resulted in an increasing demand for fundamental material property data. Laboratory analysis and constitutive models have shown that rock elastic and deformational properties are not single-value, well-defined parameters for a given rock. Finding suitable values for these parameters is of vital importance in many geomechanical applications. For instance, Poisson's ratio is often used within geophysics in the identification of lithology from seismic data and the Amplitude Versus Offset (AVO) analysis. Furthermore, current practices in the oil industry involves the evaluation of the brittleness of the shale formation as a deciding factor for identifying prospect intervals for fracturing stimulation.

In this thesis an extensive experimental program to explore geomechanical properties of shale was developed. A series of triaxial tests were performed in order to evaluate the elasticity, yielding, and failure response of Marcellus shale specimens as a function of pressure, temperature, and bedding angle. Additional characterization includes mineralogy, porosity, and fabric. Rock samples used in this study came from three different locations and depths: one actual reservoir ($\sim$7,500 ft. deep), and two outcrops ($\sim$300 ft. and $\sim$0 ft.).

Acknowledgements

The years I spent at the University of Vermont were filled with fruitful experiences and I owe many thanks to the people who have helped me grow both academically and personally.

First, I would like to thank all those professors who have made it possible for me to be here. Starting with Dr. Enrique Asanza who encouraged me to focus my professional career on Environmental and Energy Geotechnics, and, specially, to do an exchange academic year in the United States. At that time, three years ago now, I had the fortune of knowing Dr. George Pinder and Dr. Mandar Dewoolkar whose courses greatly contributed to reinforce my interest in geotechnical engineering. Attending UVM during my senior year was a pleasure, most rewarding and highly educational. Thanks to my advisor, Dr. Ehsan Ghazanfari for his guidance and encouragement, and for giving me the opportunity to work on such a fascinating area. I'm also grateful to Dr. Huston, for serving in my thesis committee.

Also, I would like to thank professor Terry Engelder (Geosciences Department, Penn State University) for providing the shale samples used in this study. I appreciate the help and assistance of professors Nicolas Perdrial and Julia Perdrial (Geology Department, University of Vermont), who helped me with the sample characterization. I would like to acknowledge the National Science Foundation Grant 1429252 for equipment support, as well to thanks Max Graves and Lucas Howard for their assistance with X-ray tomography.

Thanks to all my office mates for creating a constructive and fun environment, and to all those friends I made in these three years.

Por último, quisiera dar gracias a mis padres, a mis hermanos y a Isabela. Por animarme y apoyarme tanto todo este tiempo. Es gracias a ellos por lo que estoy aquí.

Table of Contents

List of Figures

List of Tables

Chapter 1

Introduction

1.1 Motivation

A few months ago, Charles Fairhurst, one of the fathers of rock mechanics, published an essay entitled "Thinking Deeper" (Fairhurst 2014). This made an extensive review of Earth Resources Engineering and global challenges. Current projections state that Earth's population is expected to rise at a rapid rate over the next decades, resulting in a population of 9.6 billion people by the year 2050, and nearly 11 billion by the year 2100. Alongside this, the increase in average standard of living will result in a greater consumption of energy and planetary resources. As civil engineers, we should play a leading role to the preparation of our planet for such population growth so that it can be achieved in an economically and environmentally sustainable manner.

How can we provide accessible, affordable, and secure energy while protecting the planet? There is no doubt that renewable energy is the answer. But we are going to need at least

50 more years until renewable energy technologies are mature enough to supply the energy demand. During this transition, we should move towards cleaner energy sources.

Given their potential applications for a number of engineering purposes, the geomechanics of shale reservoirs is becoming one of the most important issues in modern geomechanics. Borehole stability modeling, geophysics, shale oil and shale gas reservoirs, and underground storage of CO_2 and nuclear waste are some of these potential applications to name a few. The growing interest in these reservoirs, as a source for hydrocarbons production, has resulted in an increasing demand for fundamental material property data.

Laboratory analysis and constitutive models have shown that for a given type of rock, elastic and deformational properties are not single-value, well-defined parameters. Finding suitable values for these parameters is of vital importance in many geomechanical applications. For instance, Poisson's ratio is often used within geophysics in the identification of lithology from seismic data and the Amplitude Versus Offset (AVO) analysis. Furthermore, current practices in the oil industry involves the evaluation of the brittleness of the shale formation as a deciding factor for identifying prospect intervals for fracturing stimulation.

1.2 Research Objectives

Shale gas rocks are known to be non-linear materials. There are many factors, such as induced cracks and their orientation, partial saturation, viscoelastic effects, or temperature that may impact the geomechanical behavior of these shales. Potential challenges in

characterization of shale rocks are related with geochemistry, anisotropy, petrophysical and geomechanical properties, and transport properties.

The goal of this work was to generate a rich dataset on shales, and to analyze the data to obtain their geomechanical properties. A series of triaxial tests were performed in order to evaluate the elasticity, viscoplasticity, yielding, and failure response of Marcellus shale specimens as a function of pressure, temperature, and bedding angle. Additional characterization includes mineralogy, porosity, and fabric. Rock samples used in this study were retrieved from three different locations and depths: one actual reservoir (7,500 ft. deep), and two outcrops (300 ft. and 0 ft.).

Primary objectives of this research included:

(1) *Full characterization of the solid rock skeleton*: A 'zero data set' was generated for future studies and comparisons.

(2) *Investigation of suitability for multi-stage triaxial tests*: Sample scarcity and variability are major issues in reservoir geomechanics laboratory testing. Obtaining the full failure envelope from a single core is of fundamental importance, but appropriateness must be verified first.The suitability of multi-stage triaxial tests for Marcellus shale samples were investigated.

(3) *Exploring rock anisotropy*: As many other sedimentary rocks, shales are known to be vertical transverse isotropic (VTI) materials. Laboratory characterization of the full elastic tensor is challenging, but a necessary step for reservoir modeling. This was achieved using a coupling model since all rock plugs were cored in the same direction.

(4) *Investigation of creep behavior*: Identified as a major contributor to the permeability decrease and, therefore, production decline, creep behavior is one of the most important parameters for reservoir modeling. Creep behavior of Marcellus samples was investigated at different temperature ranges,

(5) *Testing under reservoir conditions*: A series of triaxial tests were conducted under different temperature conditions, and the results were compared to the 'zero data set'.

1.3 Thesis Outline

This thesis focuses on the laboratory characterization of geomechanical behavior of shale rocks, and is organized as follows:

Chapter 2 presents a comprehensive literature review on the topic. Chapter 3 is the main body of the thesis, in the form of a draft of a journal article manuscript. Chapter 4 discusses conclusions and recommendations to extend the present research, followed by a comprehensive bibliography. Lastly, a series of appendices summarizing additional experimental work that will serve as a basis for future research are included.

Chapter 2

Literature Review

2.1 The Shale Gas Revolution

Hydrocarbon production from unconventional shale gas reservoirs has attracted more attention in recent years due to its notable contribution to the increase of the nation's gas proved reserves (EIA, 2013). Advances in technology, especially in horizontal drilling and hydraulic fracturing, have enabled economic production from these formations. These unconventional reservoirs are characterized by extremely small grain sizes, elevated total organic carbon, and low natural permeability, which usually range in the nano-Darcy scale (Vermylen 2011, Ghassemi 2012). Therefore, achieving economic gas production requires hydraulic fracturing stimulation of the reservoir to create a large surface area for gas to flow to the wellbore. Optimizing this production strongly depends on the ability of the hydraulic stimulation to activate an extensive fracture network (Maxwell 2011). The major problem here is the variability and unpredictability of the outcome from these fracturing operations.

CHAPTER 2. LITERATURE REVIEW

Current industrial practice involves the evaluation of the brittleness of the shale formation as a deciding factor for identifying prospect intervals for fracturing stimulation (Rickman et al., 2008). However, this practice is not based on the geomechanical behavior of shale reservoirs, which ultimately is controlled by the conjunction of in-situ state of stresses and deformational properties.

One of the major concerns about hydraulic fracturing is the possibility for fractures to extend to the deepest aquifers causing groundwater contamination. During fracturing operations, fractures propagate in the direction perpendicular to the minimum principal stress. In addition, a significant number of shear failures are generated in the surrounding intact reservoir rock (Vermylen 2011). Despite this basic framework, the mechanism of hydraulic fracturing is poorly understood, and mathematical models cannot yet precisely predict fracture growth (Vermylen 2011, Davies et al. 2012). In fact, the knowledge about the propagation of fractures at in situ conditions comes from industry experience (King et al. 2008, Davies et al. 2012). Furthermore, rock fracture is also controlled by the in situ state of stresses, estimation of which is challenging and cannot be completely accomplished by direct means. Here, the role of geo-mechanics is the determination of the growth pattern and extent of hydraulically induced fractures in shale formations under a range of conditions and material properties. Thereby, before we can accurately predict the facture network resulting from a specific injection, we need to understand the factors and rock properties that control the variability in hydraulic fracture networks (Maxwell 2011).

Another issue that has a major economic impact on gas production is the loss of productive fracture area and fracture conductivity in shale formations (Ghassemi and Suarez-Rivera 2012). As gas is initially produced, pore pressure is drawn down resulting in an increase in

the effective pressure that eventually leads to the closure of fractures and microfractures resulting in a reduction of permeability on multiple scales (Vermylen 2011, Ghassemi and Suarez-Rivera 2012). On the other hand, creep deformation also affects the transport properties in the long term as well as the regional stress state that has a major impact in hydraulic fracturing success. Therefore, understanding the causes and the rate of decline of production/permeability is a key factor in the management and operational design of shale gas reservoirs.

To date, many researchers have pointed the importance of understanding deformational properties to better optimize operational procedures in shale gas reservoirs (Jacobi et al. 2008, Britt et al. 2009, Sone 2012, Ghassemi and Suarez-Rivera 2012). Rock cores are the principal sources for such characterization. However, they are not always available since their extraction is complicated. Also, they do not fully represent the target formation as they come from discrete levels. Actually, a characteristic feature of these formations is their high vertical variability. Although shale gas formations can be hundreds of meters thick, large ranges in lithology are observed at vertical scale of few tens of centimeters. This vertical heterogeneity is directly tied back to geologic and biotic conditions when deposited (Passey et al. 2010). In the field, elastic properties are often measured by dynamic techniques, which are capable to characterize large areas (Jacobi et al. 2008). Nevertheless, geophysical investigations cannot capture deformational properties. From a geomechanical perspective, linking between the small-strain elastic properties and the large-strain deformational properties of shale gas is crucial for the exploitation of shale gas reservoirs (Sone 2012).

2.2 Laboratory Characterization of Shale Properties

Shales have been widely characterized in the past years due to their role in a number of petroleum related issues (e.g. top seal evaluation, overpressure prediction, or wellbore stability). Nevertheless, the development of unconventional shale gas reservoirs has required adapting the traditional laboratory characterization techniques to the complex properties of these rocks. Shale rocks, more properly referred to as mudstones, are composed of extremely fine-grained particles (typically less than 4 μm in diameter), although they may contain variable amount of silt-size particles (up to 62 μm). Their mineralogy composition exhibits a wide range in composition (clay, quartz, feldspar, heavy minerals, etc.), even though when, to the naked eye, many mudstones look similar (Passey et al. 2010). Specific properties of importance for shale gas include silt content, organic matter abundance and type, static and dynamic mechanical properties (brittleness), micro/macro-fabrics, porosity, permeability, petrophysical properties and anisotropy. Workflows for systematic shale characterization in the laboratory (Dewhurst and Siggins 2006, Britt et al. 2009, Dewhurst et al. 2011, Josh et al. 2012) usually include a full suite of non-destructive petrophysical methods before destructive geomechanical testing.

These rocks are usually envisioned as a multi-scale media composed of an anisotropic clay matrix surrounding multiple inclusions such as stiffer minerals, kerogen and microfractures (Sarout and Guéguen 2008b). The origin of anisotropy in shales has been largely discussed (Dewhurst and Siggins 2006, Dewhurst et al. 2011, Sone and Zoback 2013a, Salager et al. 2012). In the microscale, fabric anisotropy is usually defined by the preferential

orientation of clay matrix, along with the grain arrangements and the alignment of various elongated inclusions (Sone and Zoback 2013a). At larger scales, bedding, schistosity, cleavage or foliation may also affect the anisotropic behavior of these rocks. Moreover, induced anisotropy may occur after the application of anisotropic stresses, yielding to the development of void preferential orientations, fractures, shear planes, and faults or joints (Salager et al. 2012, Kuila et al. 2011).

A smart way to study both intrinsic and stress-induced anisotropy is through the single core plug method utilizing pulse transmission (Dewhurst and Siggins 2006, Sarout and Guéguen 2008a, Dewhurst et al. 2011, Kuila et al. 2011). This experimental methodology allows for the identification of the whole dynamic elastic stiffness tensor of a transversely isotropic medium from a single cylindrical sample under triaxial loading conditions, using elastic wave velocity measurements. These tests are conducted either in dry, drained or undrained conditions, and usually consists on multiple confining stages. Multistage triaxial testing assures homogeneity for better interpretation of the measurements, since these tests eliminate the serious variability in measurements introduced by heterogeneity between core plugs. The trade-off is that such tests may fatigue the sample, reflecting the core a weaker behavior.

To date, many researchers have pointed the importance of understanding the linking between the small-strain elastic properties and the large-strain deformational properties of shale to better optimize operational procedures in unconventional gas reservoirs (Sone 2012, Ghassemi and Suarez-Rivera 2012, Britt et al. 2009, Jacobi et al. 2008). Sone and Zoback (2013a, 2013b) conducted a series of triaxial tests on shale samples in order to study the correlation between deformational properties and elastics properties, as well as their relationship to anisotropy (Sone and Zoback 2013a, Sone and Zoback 2013b).

Elastic properties of gas shales were reported to be strongly anisotropic, and the degree of anisotropy found to be correlated with the clay and organic content of the rock (Sone and Zoback 2013a). This study, elastic properties were studied using both static and dynamic methods.

Considerable effort has been also spent in the investigation of deformational properties of shale formations through characterization of their viscoelastic-plastic behavior. Ghassemi ans Suarez Rivera (2012) and Sone and Zoback (2013a) found that creep strain is correlated with Young's modulus, and clay and organic content (Ghassemi and Suarez-Rivera 2012, Sone and Zoback 2013b). Results from these studies showed that creep behavior can be described using a power-law strain-time model during both hydrostatic and triaxial stage. Nevertheless, during triaxial stage creep behavior is better described by a mechanical system known as Burgers model. This system is composed of a series of springs and dashpots, which are able to reproduce the elastic and viscous response of creep. Both studies also observed that creep strain is smaller in the radial direction indicating a volume loss, most likely accommodated by microcrack and pore closure.

On the other hand, thermo-mechanical behavior of shale rocks is attracting considerable attention in the recent years. Experimental results and theoretical considerations have shown that temperature may play an important role on shale geomechanics (Horsrud 2001, Eseme et al. 2007, Ghassemi and Suarez-Rivera 2012, Islam and Skalle 2013, Mohamadi et al. 2013, Bauer et al. 2014). At high temperature, mechanical behavior of shales is complex. At the onset of heating, pore fluids (free and bound water, and light hydrocarbons) vaporize, and thermal expansion of minerals, as well as softening of kerogen and development of pore pressure occur. At higher temperatures, kerogen deforms

plastically and ultimately decomposes into bitumen that may flow into pores. Strength, elastic moduli and acoustic velocities of shales decrease with increasing temperature. Also, an increase in temperature beyond 150 ^{o}C leads to a thermally-activated softening of the kerogen, and have an important effect on creep behavior (Eseme et al. 2007). Actually, under the conditions of high pressure and high temperature (HPHT) rocks show ductile behavior, behaving more like a metal rather than a brittle material, as they do under normal conditions (Zahoor 2014).

As a consequence of the shale energy revolution, a rising number of works addressing shale rock characterization can be found in the literature. Sone (2012) pointed out the important inter-and intra-variability of these reservoirs. This study generated a large volume of geomechanical data from laboratory analysis using samples from Barnett, Haynesville, Eagle Ford, and Fort St. John shale gas plays. However, this study did not include any data from the most expansive shale reservoir in the U.S.A.: the Marcellus Shale. These black, organic-rich shales are estimated to hold about 489 trillion cubit feet (Tcf) of natural gas (Engelder and Lash, 2008; Engerlder, 2009; Kargbo Fjaer et al., 2010). Therefore, many researchers are currently focusing on this play, and the demand for fundamental rock property data is constantly increasing.

Chapter 3

Geomechanical Characterization of Marcellus Shale

3.1 Introduction

Hydrocarbon production from unconventional shale gas reservoirs has attracted more attention in recent years due to its notable contribution to the increase of the nation's gas proved reserves (EIA, 2013). Advances in technology, especially in horizontal drilling and hydraulic fracturing, have enabled economic production from these formations. Shale rocks, more properly referred to as mudstones, are composed by extremely fine-grain (typically less than 4 μm in diameter), clay-like particles, which yields to a extremely low natural permeability ranging in the nano-Darcy scale (Britt et al. 2009, Vermylen 2011, Ghassemi 2012). Moreover, their mineralogy and total organic content (TOC) exhibit

a wide range in composition, even though many shales look similar to the naked eye (Passey et al. 2010, Sone and Zoback 2013a).

Achieving economic gas production in these unconventional plays requires hydraulic fracturing stimulation of the reservoir to create a large surface area for gas to flow to the wellbore. Optimizing this production depends strongly on the ability of the hydraulic stimulation to activate an extensive fracture network (Maxwell 2011). The major problem here is the variability and unpredictability of the outcome from these fracturing operations. Current industrial practice involves the evaluation of the brittleness of the shale formation as a deciding factor for identifying prospect intervals for fracturing stimulation (Rickman et al. 2008). However, this practice is not based on the geomechanical behavior of shale reservoirs, which ultimately is controlled by the conjunction of in-situ state of stresses and deformational properties (Sone 2012).

One of the major concerns about hydraulic fracturing is the possibility for fractures to extend to the deepest aquifers causing groundwater contamination. During fracturing operations, fractures propagate in the direction perpendicular to the minimum principal stress. In addition, a significant number of shear failures are generated in the surrounding intact reservoir rock (Vermylen 2011). Despite this basic framework, the mechanism of hydraulic fracturing is poorly understood, and mathematical models cannot yet precisely predict fracture growth (Vermylen 2011, Davies et al. 2012). In fact, the knowledge about the propagation of fractures at in situ conditions comes from industry experience (King et al. 2008, Davies et al. 2012). Furthermore, rock fracture is also controlled by the in situ state of stresses, estimation of which is challenging and cannot be completely accomplished by direct means. Here, the role of geomechanics is the determination of the

growth pattern and extent of hydraulically induced fractures in shale formations under a range of conditions and material properties. Thereby, before we can accurately predict the fracture network resulting from a specific injection, we need to understand the factors and rock properties that control the variability in hydraulic fracture networks (Maxwell 2011).

To date, many researchers have pointed the importance of understanding deformational properties to better optimize operational procedures in shale gas reservoirs (Jacobi et al. 2008, Britt et al. 2009, Sone 2012, Ghassemi and Suarez-Rivera 2012). Elastic properties of gas shales were reported to be strongly anisotropic. Moreover, laboratory analysis and constitutive models have shown that rock elastic and deformational properties are not single-value, well-defined parameters for a given rock (Islam and Skalle 2013). Finding suitable values for these parameters is of vital importance in many geomechanical applications.

As a consequence of the shale energy revolution, a rising number of works addressing shale rock characterization can be found in the literature. Sone and Zoback (2013a, 2013b) pointed out the important inter-and intra-variability of these reservoirs (Sone and Zoback 2013a, Sone and Zoback 2013b). They generated a large volume of rock mechanical data from laboratory analysis using samples from Barnett, Haynesville, Eagle Ford, and Fort St. John shale gas plays. However, these studies did not include any data from the most expansive shale reservoir in the United States: the Marcellus Shale. These black, organic-rich shales are estimated to hold about 489 trillion cubit feet (Tcf) (Engelder 2009, Kargbo et al. 2010). Therefore, many researchers are currently focusing on this play, and therefore, the demand of fundamental rock property data is constantly increasing.

3.2 Materials and Methods

3.2.1 Materials and Samples

Shale samples used in this study came from a shallow well located at State Game Lands 252, Lycoming and Union counties, Allenwood, Pennsylvania. The rock plugs were retrieved in 2009 by Department of Geosciences at Pennsylvania State University, and stored at room temperature and humidity conditions. All cores are oriented perpendicular to the bedding (vertical samples), hindering characterization of anisotropy. Residual fluid content in these shales was found to be below 2%, and it is considered low enough so that poroelastic effects can assumed to be negligible. Neither rehydration or oven-drying were attempted in order to preserve mechanical properties. Although resaturation of shales is possible under a controlled humidity atmosphere (Schmitt et al. 1994), such processes may change the internal structure and properties of the shale even when the manufactured pore fluid is assumed to match the original pore water chemical composition (Fjær. et al. 2008). On the other hand, oven-drying may have lead to the loss of the clay-bound water possibly leading to drastic changes in mechanical properties.

3.2.2 Sample Characterization

Mineralogy, Organic Content and Porosity

Mineralogy and petrological properties were studied via X-ray diffraction (XRD), and Total Organic Carbon (TOC) was measured by sample combustion. TOC is a fundamental

parameter in assessing shale reservoirs potential, since it correlates the total porosity and gas content in the rock (Passey et al. 2010). Porosity was estimated by comparison of the bulk density of the rock with the average grain density (Mavko et al. 2009) determined from the XRD and TOC tests. Average material composition is summarized in Table 3.1.

Table 3.1: **Material Composition**

Bulk Density	**Mineralogy (%)**			**TOC**	**Porosity**
(g/cc)	*Tectosilicates*	*Carbonates*	*Clays*	**(%)**	**(%)**
2.58	35.9	3.7	57.7	2.7	5.0

For this study, shale samples were selected from a depth between 315 and 370 feet. Bulk density is fairly consistent within the interval with an average value of 2.58 $\pm$ 0.05 g/cm^3. These Marcellus shale samples have moderate organic content, being the measured TOC percentage weight rougly 2.7%. Porosity was estimated to be close to 5 %, which is in good agreement with the trends found by Sone and Zoback (2013) given the clay/kerogen content of the tested samples (Sone and Zoback 2013a). Moreover, porosity in organic rich shales is believed to reside within the kerogen and/or clay minerals platelets (Sondergeld et al. 2010, Loucks et al. 2009, Sone and Zoback 2013a, Passey et al. 2010).

The XRD test revealed that clay and quartz minerals are the major constituents of these samples (see Apendix A). Clay minerals in our shales were mostly from the mica group. Based on these laboratory results, this shale, with a clay content in excess of 40%, is not likely to be prospective due to both a reduced permeability and excess of ductility (Britt et al. 2009). Prospective gas shales are dominated by carbonates and quartz, and due to their brittle nature are often sought as target intervals for hydraulic fracturing (Dewhurst et al. 2013, Sone and Zoback 2013a).

CHAPTER 3. GEOMECHANICAL CHARACTERIZATION OF MARCELLUS SHALE

Multi-scale Visualuzation

It is well known that the elastic and mechanical behavior of shales is largely controlled by their microstructure (Josh et al. 2012). Due to their large heterogeneity at different scales, microstructure characterization of shales requires different multi-scale visualization techniques. Rock fabric was studied via both scanning electron (secondary and backscattered analysis) and optical microscopes with polarized light. Besides, post-mortem analysis of the cores were carried out using X-ray tomograhy for inspection of resulting fracture patterns.

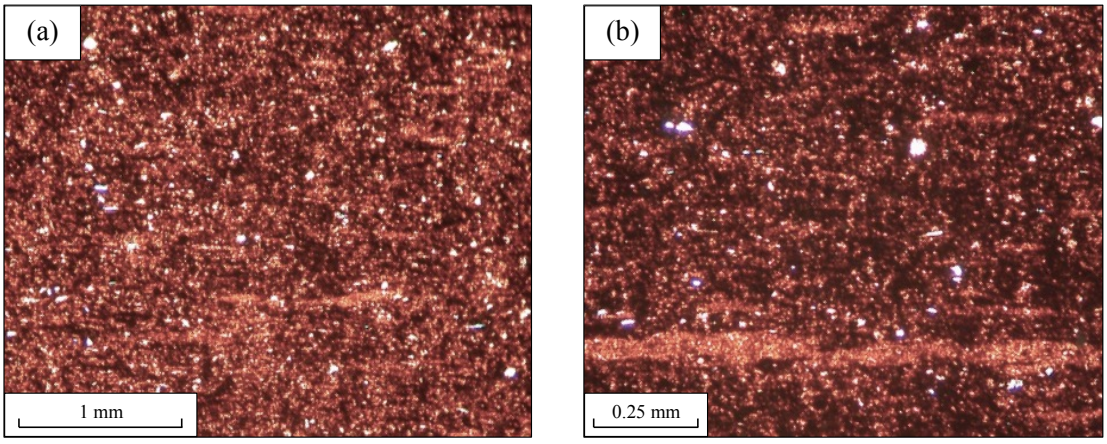

Figure 3.1: **Optical microscope images of Marcellus Shale (vh plane).**

Optical microscope images (Figure 3.1) exhibit macroscopic primary foliation (bedding) at different scales. On the other hand, SEM images (Figure 3.2) reveal a microstructure consisting of a clayey matrix with silt grains and other various-shape inclusions. Note that the preferential (sub-parallel to bedding) orientation in these shales is preserved across scales. Figure 3.2(b) shows stress-relief microcracks oriented subparallel to bedding. These horizontal fractures tend to increase the compliance in the direction perpendicular to the

bedding, being also responsible for the initial nonlinear mechanical behavior. Moreover, porosity is not visible at this scale. Previous studies have shown that maximum pore throat in shales is in the nanometer scale (Loucks et al. 2009, Sondergeld et al. 2010, Passey et al. 2010, Josh et al. 2012).

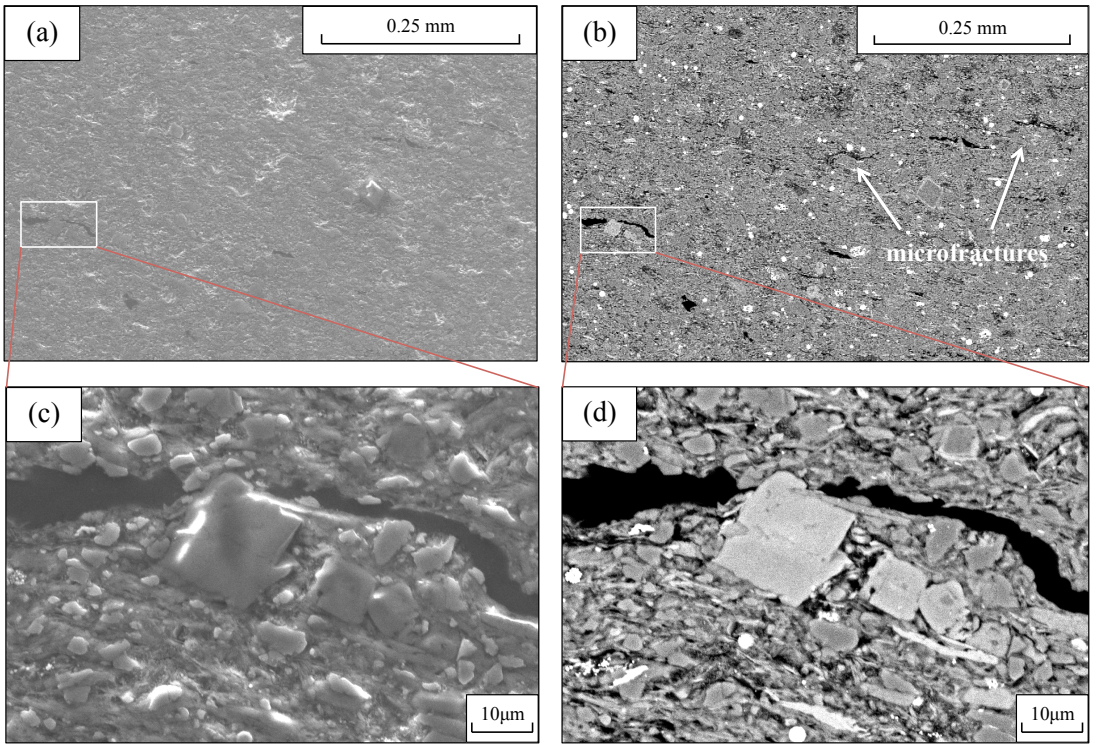

Figure 3.2: **Comparison of Secondary (a and c) and Backscattered (b and d) electron microscope images of Marcellus Shale. Contrast in grey level in backscattered analysis reflect different material density. (c) and (d) correspond to regions delimited by white rectangles in images (a) and (b)**

3.2.3 Laboratory Procedures

High Pressure Triaxial Apparatus

A series of triaxial compression experiments was conducted using a fully servo-controlled triaxial apparatus AutoLab 1500. The experimental program used cylindrical samples of rock plugs 2-in. diameter with horizontal bedding planes (i.e. cylinder axis perpendicular to material deposition planes). Length/diameter aspect ratio was kept as close to 2 as possible. Although international standards recommend a core length twice the diameter, lower ratios are still acceptable as confining pressure rapidly suppresses the effect of size on failure strength at high pressure levels (Moronkeji et al. 2014). Deformation was measured by axial and radial strain gauges installed on a copper sleeve. This copper sleeve also acts as a barrier between the sample and the confining fluid. A maximum of four strain gauges were used simultaneously, usually 2 pairs consisting of 1 axial plus 1 radial gauges. These pairs of gauges were placed 90^o with respect to each other as shown in Figure 3.3(b). In addition, a Linear Variable Differential Transformer (LVDT) measured piston displacement, which was used to backup axial strain when no strain gauge data were available.

Heating of the speciments up to 120 ^{o}C is also possible thanks to the external furnace embedded in the equipment. The temperature was measured using a thermal couple inside the cell in contact with the confining fluid. Strain readings did not require any post-processing as self-temperature-compensated strain gauges were used in our experiments.

Although the triaxial system includes pore pressure control, mechanical tests were run under dry conditions because of two main reasons. Firstly, available shale samples were

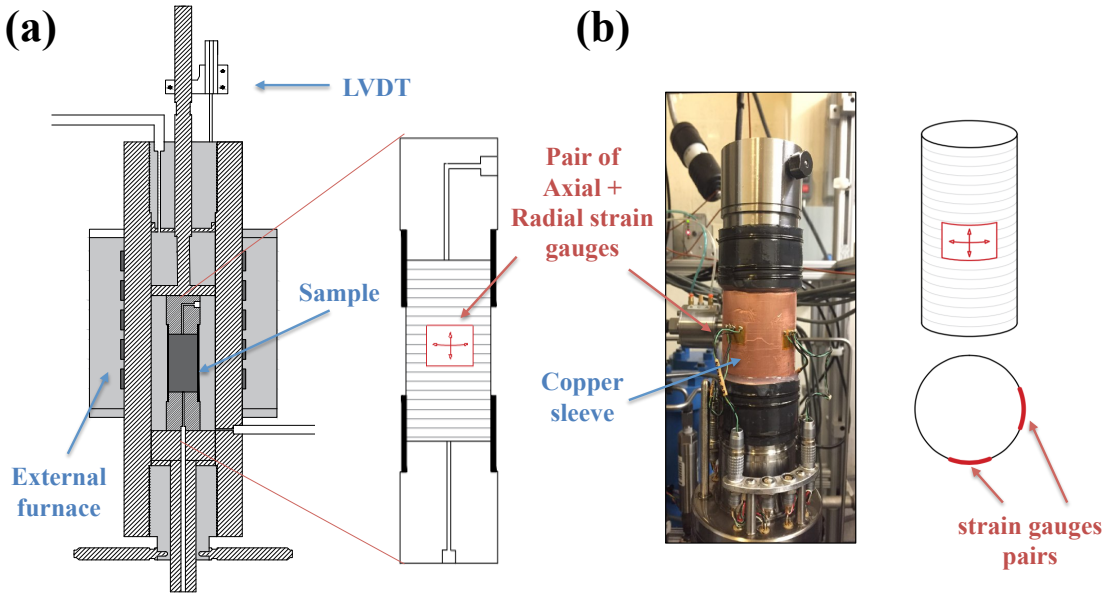

Figure 3.3: **(a) Layout of the triaxial apparatus used in the experiments. (b) Two pairs (axial + radial) of strain gauges installed on the copper sleeve.**

room-dried and re-saturation process is complicate and may damage the rock. Secondly, due to the low permeability of shales, a single drained test may take several weeks, even months (Islam and Skalle 2013, Dewhurst and Siggins 2006).

Single Stage Triaxial

The objective of this first set of tests was to study the geomechanical behavior of Marcellus shale samples under constant axial strain rate loading. A series of seven Single Stage (SS) triaxial tests at different confining pressures (0, 5, 15, 20, 27.5 , 35 and 70 MPa) were performed where rock samples were taken to failure under triaxial loading at a constant axial strain rate of $10^{-5}s^{-1}$ to measure elastic, plastic and strength properties.

Figure 3.4(a) shows the typical stress path followed in the experiments. At the beginning of each test (Hydrostatic Stage), the confining pressure, σ_3, was increased up to the target level following a multistep-wise loading increments of 5 MPa at a constant rate of 0.33 MPa/s. After each loading step, σ_3 was held for an hour to ensure uniform consolidation. Then the sample was taken to failure (Triaxial Stage) at a constant axial strain rate to measure intact strength properties. Elastic parameters were estimated from initial modulus (see section 3.3).

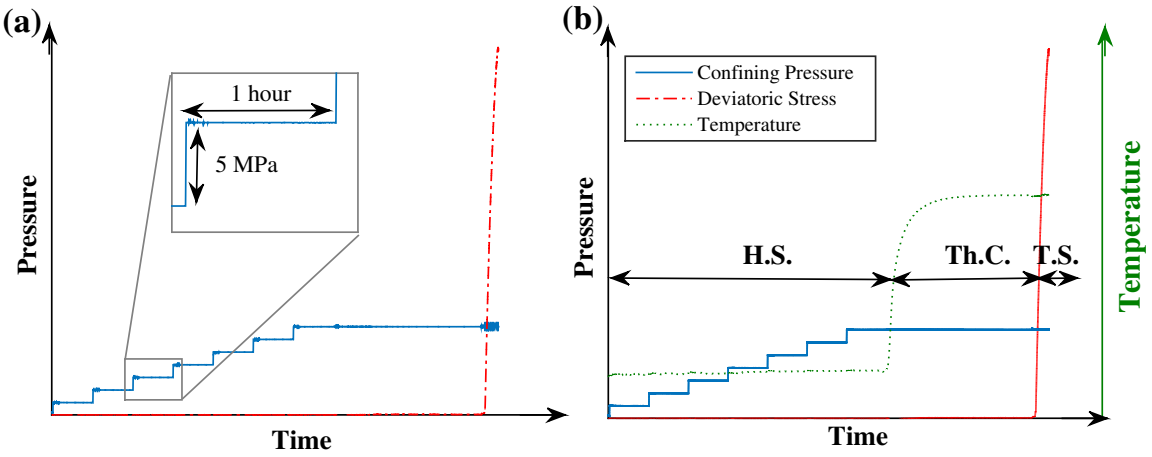

Figure 3.4: **Example of stress path followed during single stage triaxial tests under (a) room temperature and (b) high temperature. H.S. = Hydrostatic Stage; Th.C. = Thermal Consolidation Stage; T.S. = Triaxial Stage**

High Temperature Tests

Thermo-mechanical behavior of shale rocks is attracting considerable attention in the recent years. Experimental results and theoretical analysis have shown that temperature may play an important role on shale mechanical response(Horsrud 2001, Eseme et al. 2007, Ghassemi and Suarez-Rivera 2012, Islam and Skalle 2013, Mohamadi et al.

2013, Bauer et al. 2014). The high temperature tests conducted in this study includes two Single Stage triaxial tests at different temperature levels (60 ^{o}C and 120 ^{o}C). These tests (SST) were performed as regular SS tests at 35 MPa of confining pressure, but involved one more phase between the hydrostatic and triaxial stages: the thermal consolidation stage (Th.C.). During this new phase, the temperature was increased to the desired value, and axial strains were allowed to stabilize before application of any deviatoric load, q. Figure 3.4(b) shows the stress path followed in the test.

Multi Stage Triaxial Tests

Sample scarcity and variability is one of the main issues in reservoir geomechanics laboratory testing (Fjær. et al. 2008, Yang 2012, Islam and Skalle 2013). Obtaining the full suite of geomechanical parameters from a single core is of crucial importance. Two tests were performed in this experiment:

(A) *Elastic Multi-Stage Triaxial* (MSE): Shale gas rocks are known to be non-linear materials, and the characterization of their static properties requires performing unloading-reloading cycles at different stress levels in order to interpret the elastic moduli from the stress-strain response (Fjær. et al. 2008). This test consisted of 9 stages at different confinement levels ranging from 5 MPa to 70 MPa. At the beginning of each stage, σ_3 was increased following a multistep-wise loading up to the target confining pressure. Then the deviatoric load, q, was applied in 1-4 cycles increasing the load from one cycle to the next using a loading rate of 0.33 MPa/s (stress-controlled), and always maintaining q below 50% UCS and three times the

CP, so the sample stays within the elastic range. Figure 3.6 shows the stress path followed in the test.

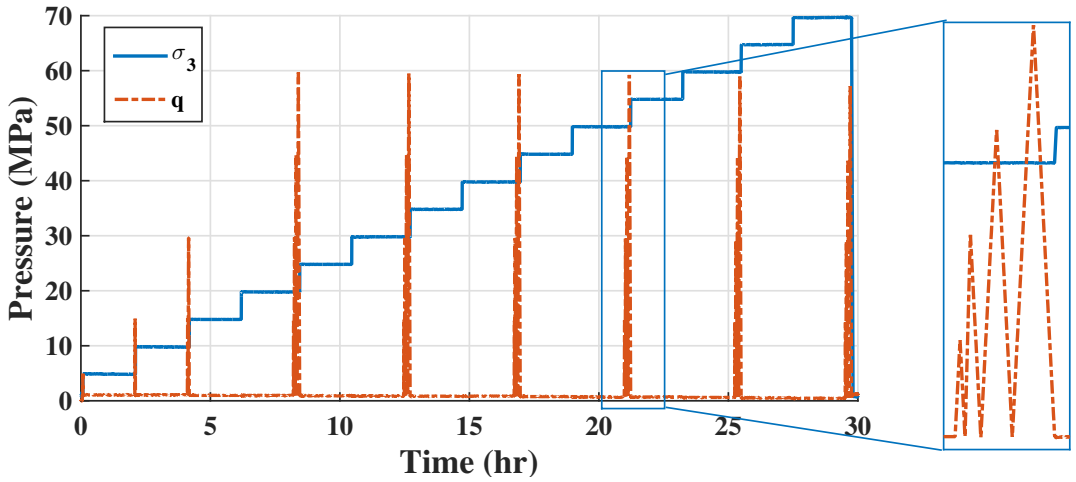

Figure 3.5: **Elastic Multi-Stage Triaxial Experiment (σ_3 = 5-70 MPa, q = 0-60 MPa)**

(B) *Failure Multi-Stage Triaxial* (MSF): Multi-stage triaxial compression experiments are not only validated alternatives for the construction of failure envelopes with only one rock core, but also good methods to eliminate specimen variability (Kovari and Tisa 1975, Bro 1997, Youn and Tonon 2010, Yang 2012). The goal of this test was to investigate the feasibility of predicting single-stage triaxial strength of Marcellus shale using multi-stage triaxial data. The test was started as a single stage triaxial test (consolidation stage + triaxial loading at constant strain rate) at σ_3 = 5 MPa. When failure was detected by a significant change in the slope of the stress-strain plot, q was removed and σ_3 increased to the next level. Finally, at the last stage the sample was taken to failure. Figure 3.6 illustrates the typical stress path and stress-strain relation of a multistage triaxial test (note that unloading curves are not shown for clarity). Loading steps were performed under strain-control conditions (axial strain rate of $10^{-5}s^{-1}$).

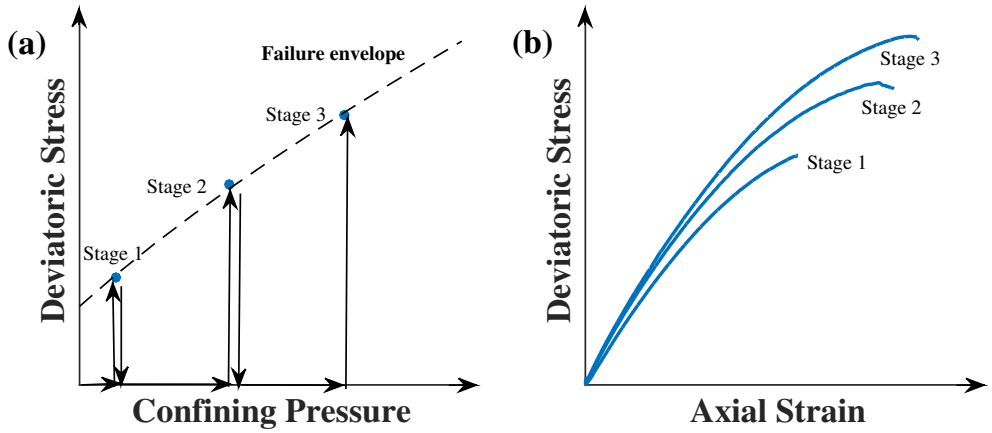

Figure 3.6: **(a) Stress Path and (b) stress-strain relation of a multistage triaxial test**

3.3 Theory

3.3.1 Transverse Isotropy

Shales are usually envisioned as a multi-scale media composed of an anisotropic clay matrix surrounding multiple inclusions such as stiffer minerals, kerogen and microfractures (Sarout and Guéguen 2008b). The origin of anisotropy in shales has been extensively discussed in the literature (Dewhurst and Siggins 2006, Dewhurst et al. 2011, Sone and Zoback 2013a, Salager et al. 2012). In the microscale, fabric anisotropy is usually defined by the preferential orientation of clay matrix, along with the grain arrangements and the alignment of various elongated inclusions (Sone and Zoback 2013a). At larger scales, bedding, schistosity, cleavage or foliation may also affect the anisotropic behavior of these rocks. Moreover, induced anisotropy may occur after the application of anisotropic stresses, yielding to the development of void preferential orientations, fractures, shear planes, and faults or joints (Salager et al. 2012, Kuila et al. 2011).

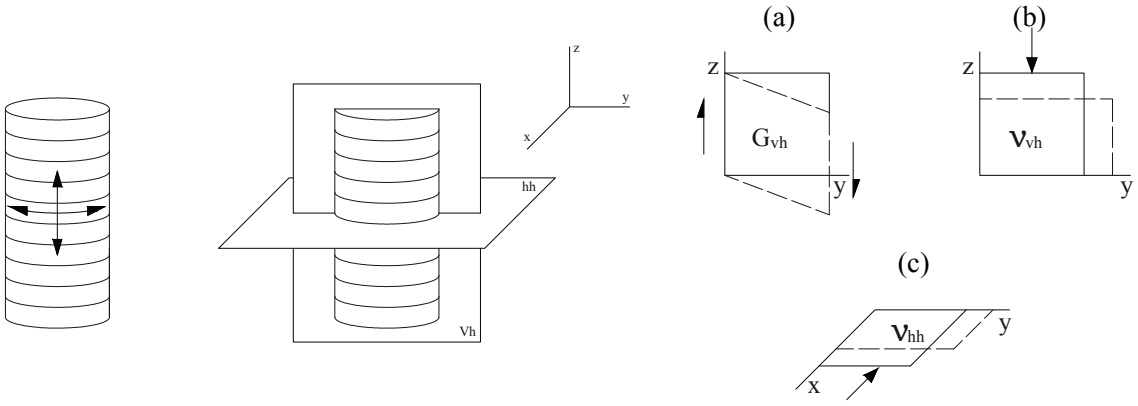

Figure 3.7: **Independent modes of shearing for Vertical Transversely Isotropic media. (a) Shearing in a vertical plane. Poisson's ratios for strains in the horizontal direction caused by (b) a vertical and (c) a orthogonal horizontal compressions. After Wood (2004).**

As many other sedimentary rocks, shales can be modeled as Vertical Transversely Isotopic (VTI) media at the macroscopic scale. This means that the mechanical properties are equal in all directions within a horizontal plane, but different in the other directions (Figure 3.7). Although, all our samples were cored perpendicular to the bedding, and full characterization of anisotropy is not possible, in this study we still treat the shale as a VTI medium with the z-axis being the axis of symmetry. The linear elastic VTI model can be expressed in terms of five independent parameters, with the compliance matrix as follows:

$$\begin{Bmatrix} \epsilon_{xx} \\ \epsilon_{yy} \\ \epsilon_{zz} \\ \epsilon_{xy} \\ \epsilon_{yz} \\ \epsilon_{xz} \end{Bmatrix} = \begin{bmatrix} \frac{1}{E_h} & -\frac{\nu_{hh}}{E_h} & -\frac{\nu_{vh}}{E_v} & 0 & 0 & 0 \\ -\frac{\nu_{hh}}{E_h} & \frac{1}{E_h} & -\frac{\nu_{vh}}{E_v} & 0 & 0 & 0 \\ -\frac{\nu_{vh}}{E_v} & -\frac{\nu_{vh}}{E_v} & \frac{1}{E_v} & 0 & 0 & 0 \\ 0 & 0 & 0 & \frac{1}{G_{vh}} & 0 & 0 \\ 0 & 0 & 0 & 0 & \frac{1}{G_{vh}} & 0 \\ 0 & 0 & 0 & 0 & 0 & \frac{2(1+\nu_{hh})}{E_h} \end{bmatrix} \begin{Bmatrix} \sigma_{xx} \\ \sigma_{yy} \\ \sigma_{zz} \\ \sigma_{xy} \\ \sigma_{yz} \\ \sigma_{xz} \end{Bmatrix} \tag{3.1}$$

where E_h and E_v are the Young's moduli for unconfined compression in the horizontal and vertical directions respectively; G_{vh} is the shear modulus for shearing in a vertical plane; and ν_{hh} and ν_{vh} represent the Poisson's ratios for strains in the horizontal direction caused by a orthogonal horizontal and vertical compressions respectively. In the context of triaxial space, Equation 3.1 can be reduced to:

$$\begin{Bmatrix} \delta\epsilon_a \\ \delta\epsilon_r \end{Bmatrix} = \begin{bmatrix} \frac{1}{E_v} & -\frac{2\nu_{vh}}{E_v} \\ -\frac{\nu_{vh}}{E_v} & -\frac{1-\nu_{hh}}{E_h} \end{bmatrix} \begin{Bmatrix} \delta\sigma_a \\ \delta\sigma_r \end{Bmatrix} \tag{3.2}$$

Note that the compliance matrix is not symmetric since the strain increment and the stress quantities are not properly work conjugate. Also, one can only determine E_v and ν_{vh}, but not E_h or ν_{hh} since they only appear in the composite stiffness $E_h/(1-\nu_{hh})$ (Lings et al. 2000, Wood 2004).

Furthermore, Equation 3.2 can be rewritten using the definitions of the triaxial strains and stresses as shown by Puzrin (Puzrin 2012):

$$\begin{Bmatrix} \delta\epsilon_v \\ \delta\epsilon_s \end{Bmatrix} = \begin{bmatrix} \frac{1}{K} & -\frac{1}{J} \\ -\frac{1}{J} & \frac{1}{3G} \end{bmatrix} \begin{Bmatrix} \delta p \\ \delta q \end{Bmatrix} \tag{3.3}$$

where, K stands for the bulk modulus during isotropic compression ($\delta q = 0$); G is the shear modulus for pure shear ($\delta p = 0$); and J is the coupling modulus. These three new parameters can be defined in terms of the original five VTI independent parameters:

$$\frac{1}{K} = 2\frac{1-\nu_{hh}}{E_h} + \frac{1-4\nu_{vh}}{E_v} \tag{3.4}$$

$$\frac{1}{J} = \frac{2}{3}\left(\frac{1-\nu_{hh}}{E_h} - \frac{1-\nu_{vh}}{E_v}\right) \tag{3.5}$$

$$\frac{1}{G} = \frac{2}{3}\left(\frac{1-\nu_{hh}}{E_h} + 2\frac{1+2nu_{vh}}{E_v}\right) \tag{3.6}$$

Compliance matrix in Equation 3.3 is symmetric (material is elastic and satisfies the law of energy conservation), and the non-zero off-diagonal terms highlight the ability of the model to reproduce both coupling between volumetric and distortional effects, and the stress path dependency of stiffness (Puzrin 2012). However, this model is only correct in the context of the triaxial test, and only if the symmetry axis stays vertical. If one wants to model the transversely isotropy in a boundary value problem, model shown in Equation 3.1 has to be used instead.

3.3.2 Triaxial Tests

Assessment of geomechanical parameters of gas shales is of fundamental importance in order to evaluate whether they will be suitable for hydraulic fracturing and keep the resulting fracture network open, or not (Britt et al. 2009, Josh et al. 2012). Important geomechanical parameters for these rocks include Young's modulus, Poisson's ratio, friction coefficient, unconfined compression strength, and cohesion strength. The estimation of such parameters is typically addressed through a series of triaxial compression tests.

Reversible behavior parameters

Defining how the interpretation of elastic moduli from the stress-strain response is accomplished becomes essential if one intends to compare moduli from different sources. Commonly accepted alternatives include secant modulus, tangent modulus, or average modulus of a linear portion of the stress-strain response (Fjær. et al. 2008). In this study, we used tangent modulus, which is preferred over the secant, due to its ability to describe the material response from the current state (Wood 2004). Among the group of elastic parameters defined above, we will address the analysis of E_v, ν_{vh}, K, J, and G.

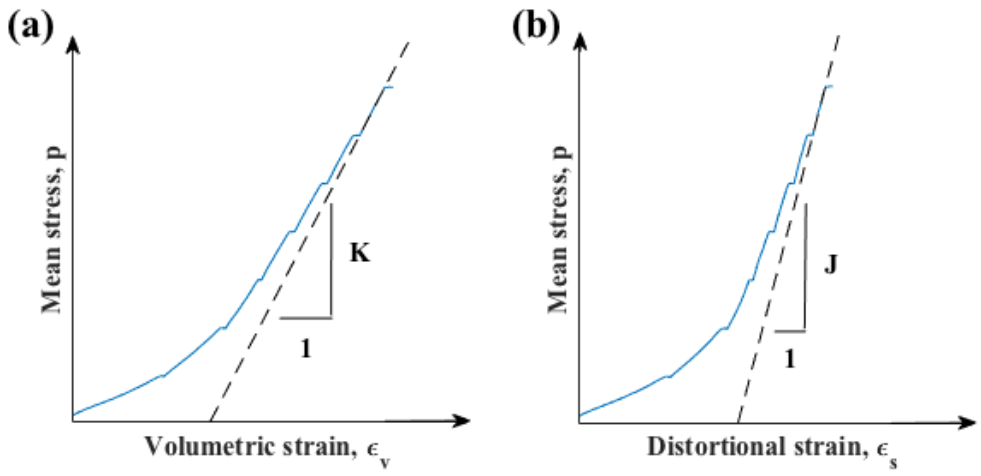

Figure 3.8: **Elastic moduli estimation from the hydrostatic stage: (a) Bulk modulus and (b) Coupling modulus. Moduli are estimated using the tangent modulus from the stress-strain response.**

From the hydrostatic stage (i.e. isotropy compression, $\delta q = 0$), we can determine both bulk and coupling moduli using Equation 3.3, as shown in Figure 3.8. Note the high non-linear behavior, and the importance of proper interpretation of the modulus. For both K and J, the slope was estimated from the last loading stage during consolidation.

On the other hand, E_v and ν_{vh} were determined from the triaxial stage (Figure 3.9) using Equation 3.2. The shear modulus, G, defined in Equation 3.3 can be only estimated after determining J.

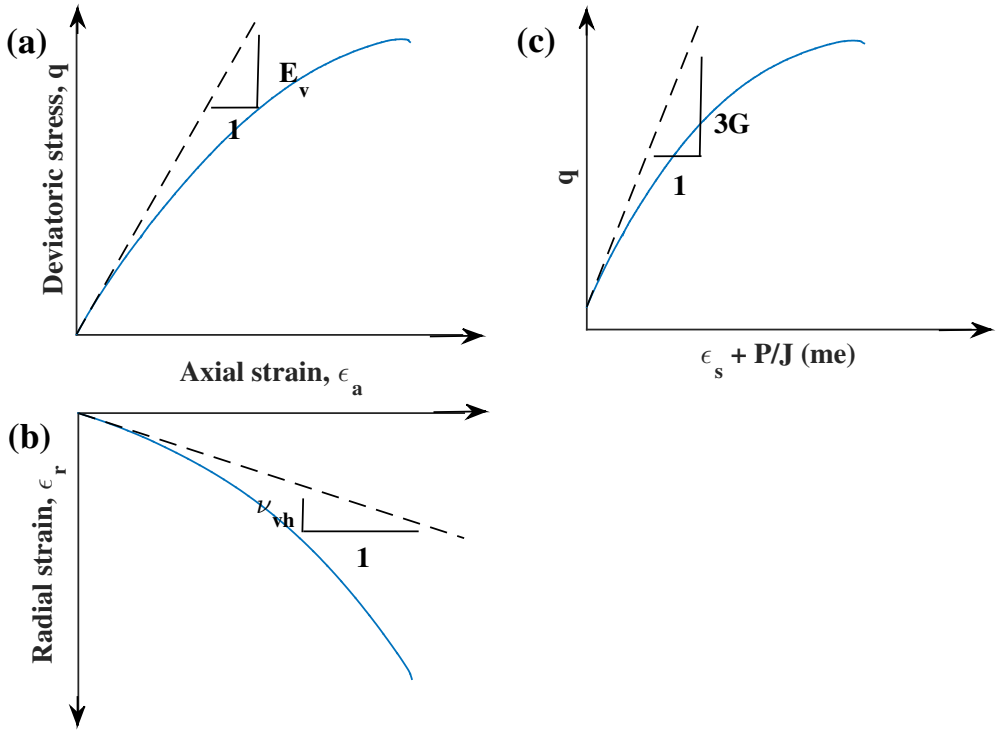

Figure 3.9: **Elastic moduli estimation from the triaxial stage: (a) Young's modulus, (b) Poisson's ratio, and (c) Shear modulus. Moduli are estimated using the tangent modulus from initial portion the stress-strain response (i.e. after closure of stress-relief microcracks).**

When the curve is strongly non-linear (as it is), complete information can only be given if the entire curve is presented. For non-linear materials, the estimation of the elastic moduli requires to perform multiple unloading-reloading cycles at different stress levels, and interpret the elastic moduli from the stress-strain response of such cycles (Fjær. et al. 2008). This is not possible for the Single Stage triaxial tests (monotonic loading), but

is possible for the Elastic Multi Stage test. Figure 3.10 shows an example of a loading-unloading-reloading cycle. For this, the applied stress is decreased after the 1^{st}-loading, and then increased again.

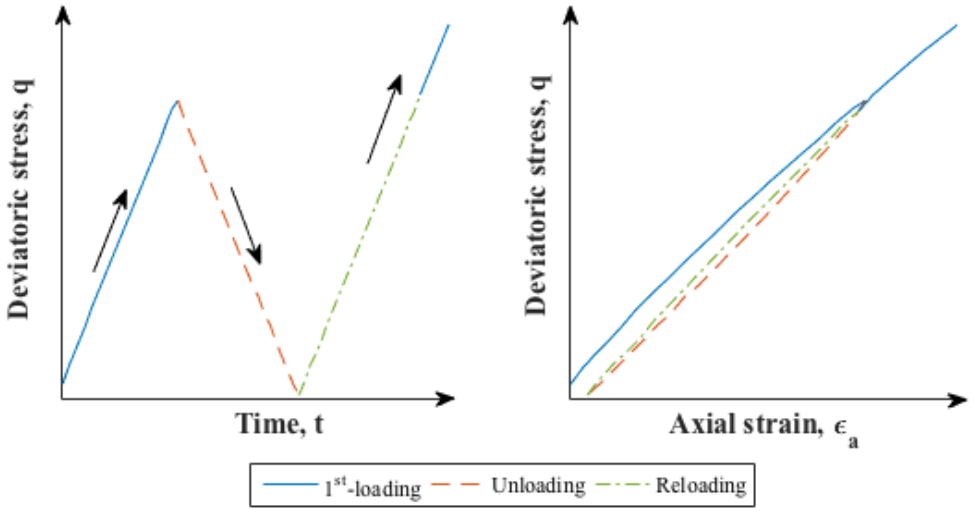

Figure 3.10: **Elastic moduli estimation from a loading-unloading-reloading cycle. Unloading-reloading behavior show higher stiffness. Also, note that some plastic deformation occurs within the cycle.**

Lastly, we should acknowledge that some irreversible deformation also occurs at small deviatoric stress levels (as seen in Figure 3.10), and therefore we should refer to the above measured quantities as *static* moduli, avoiding the term *elastic* moduli.

Irreversible behavior parameters

In general, the failure process of a rock sample subjected to uniaxial compression can be divided into several stages (Xue et al. 2014). Figure 3.11 shows a typical mechanical response during the triaxial stage. Typically, both axial and radial strains increase with

differential stress until failure. Volumetric strain is initially dominated by compaction behavior until the crack damage threshold (σ_d) is reached. Then, the volumetric strain follows a second phase of dilatancy-dominated behavior. The crack damage threshold represents the stress level where permanent damage occurs due to crack damage inside the specimen.

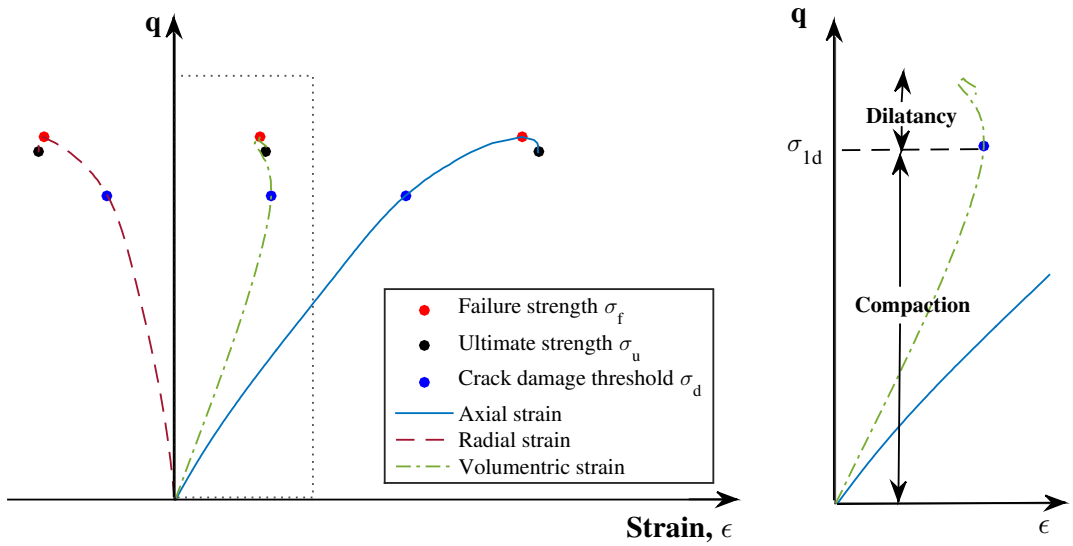

Figure 3.11: **Elastic moduli estimation from a loading-unloading-reloading cycle. Unloading-reloading behavior shows higher stiffness. Also, note that some plastic deformation occurs within the cycle.**

The dilatancy-dominated phase is characterized by unstable crack growth that leads to rock failure. Depending on the ductility of the rock, failure plane formation may not occur immediately after the peak strength (σ_f) is reached. In this case, the ultimate strength (σ_u) represents the stress level at macroscopic failure.

Failure Criteria

Two well-known and widely used criteria in rocks mechanics are the Linearized Mohr-Coulomb (Jaeger and Cook 1979) and the Empirical Hoek-Brown (Hoek and Brown 1980) models. Although the slope of Mohr failure envelope decreases as confining pressure increases, for most rocks, strength pressure dependence can be expressed in terms of a linearized Mohr-Coulomb failure envelope (Equation 3.3.2):

$$\tau = S_0 + \mu_i \sigma_n \tag{3.7}$$

Here, μ_i is the coefficient of internal friction, and S_0 is the inherent shear strength (or cohesion). Since the cohesion is not a physical measurable parameter, the latter expression is commonly written in terms of the Unconfined Compressive Strength (UCS or C_0) as shown in Equation 3.3.2:

$$\sigma_1 = C_0 + \sigma_3 tan^2\beta \tag{3.8}$$

where σ_1 and σ_3 are the maximum and minimum principal stresses at failure, respectively (Mohr-Coulomb criterion is independent of the intermediate principal stress, σ_2). The angle β gives the orientation of the failure plane with respect the maximum principal stress (i.e. the angle between the plane normal and σ_1), which is independent of the confining stress (special feature for the Mohr-Coulomb criterion).

Hoek and Brown (1980) proposed an empirical strength criterion for fractured rocks, according to which the mechanical behavior of rock masses depends on both the properties of the fractures and the properties of intact material. A special feature of this non-linear

failure criterion, shown in Equation 3.3.2, is its ability to capture the change in the slope of the failure envelope at different confining stresses.

$$\sigma_1 = \sigma_3 + \sqrt{mC_0\sigma_3 + sC_0^2} \tag{3.9}$$

This criterion uses three model parameters, where C_0 is the unconfined compressive strength of the intact (i.e. unfractured) rock, and m and s are dimensionless parameters depending on the intact material properties (Hoek and Brown 1997) and the fracture system, respectively. The parameter s represents the degree of fracturing, and it is estimated by visual inspection ranging from 0 (completely granulated specimen) to one (intact material). One drawback of this model is the lack of correlations in the literature relating m to commonly measured geophysical parameters, neither the widely used angle of internal friction (Zoback 2007). As in the case of Mohr-Coulomb criteria, this empirical criterion neglects the impact of σ_2 on rock strength.

3.4 Results

3.4.1 Single Stage Triaxial Tests

A summary of the test specimens for room and high temperature tests, along with the elastic and strength parameters results are presented in Tables 3.2 and 3.3. Due to strain gauge loss during single stage tests at 0 and 15 MPa of confining pressure (SS00 and SS15), no radial strain data are available for these tests (axial strain was estimated from the external LVDT readings) preventing the estimation of some of the elastic and strength parameters. On

the other hand, SS70 sample was not taken to failure due to equipment limitations and, therefore, only elastic behavior was characterized at this confining pressure.

Table 3.2: **Single Stage (room and high temperature) triaxial tests results: Static moduli. Note that bulk modulus was estimated from hydrostatic stage (i.e. prior any deviatoric/thermal load). Static moduli are estimated from initial slope.**

Test ID	**Core**			**Test Conditions**		**Static Moduli**				
	Ratio L:D	ρ (g/cc)	Depth (ft)	σ_3 (MPa)	T (^{o}C)	E_v (GPa)	ν_{vh}	K (GPa)	G (GPa)	J (GPa)
SS00	1.7	2.6	358	0	30	13	-	-	-	-
SS05	1.8	2.57	370	5	30	15	0.13	5	23	-9
SS15	1.8	2.43	368	15	30	17	-	-	-	-
SS20	1.8	2.56	358	20	30	18	0.13	20	9	-52
SS27	1.8	2.6	330	27.5	30	17	0.12	17	9	-54
SS35	1.9	2.61	327	35	30	19	0.15	19	10	-77
SS70	1.7	2.6	358	70	30	19	0.20	21	9	-90
SS-T60	1.7	2.61	324	35	60	19	0.15	19	9	-70
SS-T120	1.6	2.61	324	35	120	20	0.17	19	10	-69

Hydrostatic Stage

Figure 3.12(a) shows the mechanical behavior during isotropic compression of Marcellus Shale. An increase in stiffness is observed as expected from the consolidation process and the closure of microcracks. The initial behavior is characterized by high non-linearity, reflecting the closure of soft pore spaces and microcracks that may have opened as a result of the stress and pore pressure released during core extraction and sample preparation. Due to their low permeability, fractures are likely to occur in these rocks during coring and retrieval phases, leading to macroscopic and/or microscopic fractures that may significantly impact mechanical rock behavior (Fjær. et al. 2008). Although, it is not part of the five

Table 3.3: **Single Stage (room and high temperature) triaxial tests results: Strength parameters.**

Test ID	Test Conditions		Strength				
	σ_3 (MPa)	T (^{o}C)	σ_{1d} (MPa)	σ_{1f} (MPa)	σ_{1u} (MPa)	ϵ_{af} (me)	ϵ_{rf} (me)
SS00	0	30	-	100.9	94.4	8.93	-
SS05	5	30	111.9	117	117	11.02	-3.3
SS15	15	30	-	147.9	147.8	12.52	-
SS20	20	30	163.4	167.2	164.2	15.2	-4.63
SS27	27	30	179.5	186.1	180.5	16.01	-4.82
SS35	35	30	192.8	204.8	203.2	16.83	-6.37
SS-T60	35	30	175	188.3	186.5	16.74	-5.76
SS-T120	35	30	174.2	179.8	179.5	16.29	-5.94

independent parameters of the VTI model (and it is only valid in triaxial space with vertical symmetry axis) the bulk modulus was derived from the hydrostatic stage (Figure 3.12(b)). This is a good index of the stiffness of the sample prior to any deviatoric/thermal load, and shows pretty consistent behavior among the tested samples. Initial non-linearity occurs at low confining pressures (0-15 MPa), i.e. at significantly higher pressure levels than in-situ stress ($\sim$3 MPa). At higher confinement levels (15-70 MPa), monotonic increase in stiffness reveals further microfracture closure and compaction of organic matter.

Triaxial Stage

Figure 3.13 shows experimental stress-strain plots for single stage triaxial experiments at room temperature. For clarity, the post-ultimate portion of the data are not reported here. Both axial (ϵ_a) and radial (ϵ_r) strains scale with confining pressure. No trend is observed for volumetric strain (ϵ_v) . Also, note the initial non-linear behavior, and the small curvature of ϵ_a under no confinement (SS00).

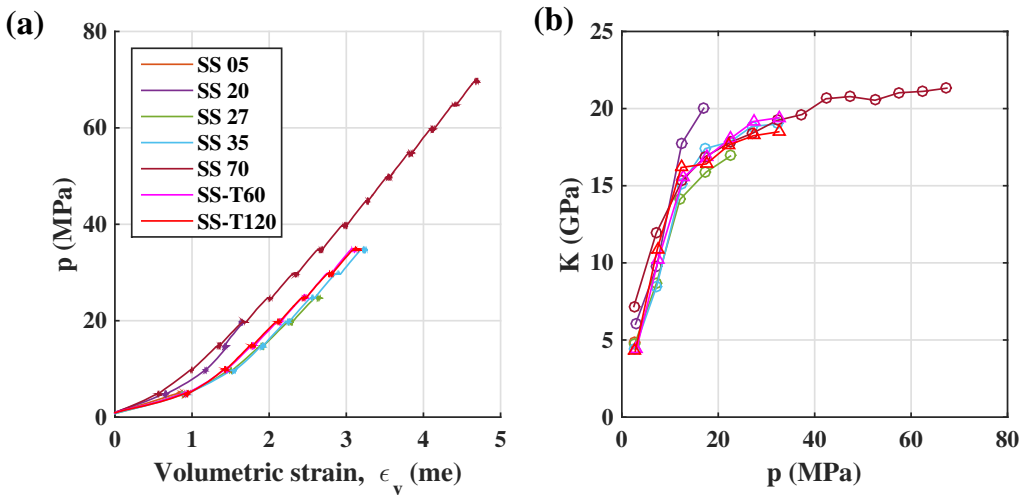

Figure 3.12: **Hydrostatic stage of Marcellus Shale triaxial experiments**

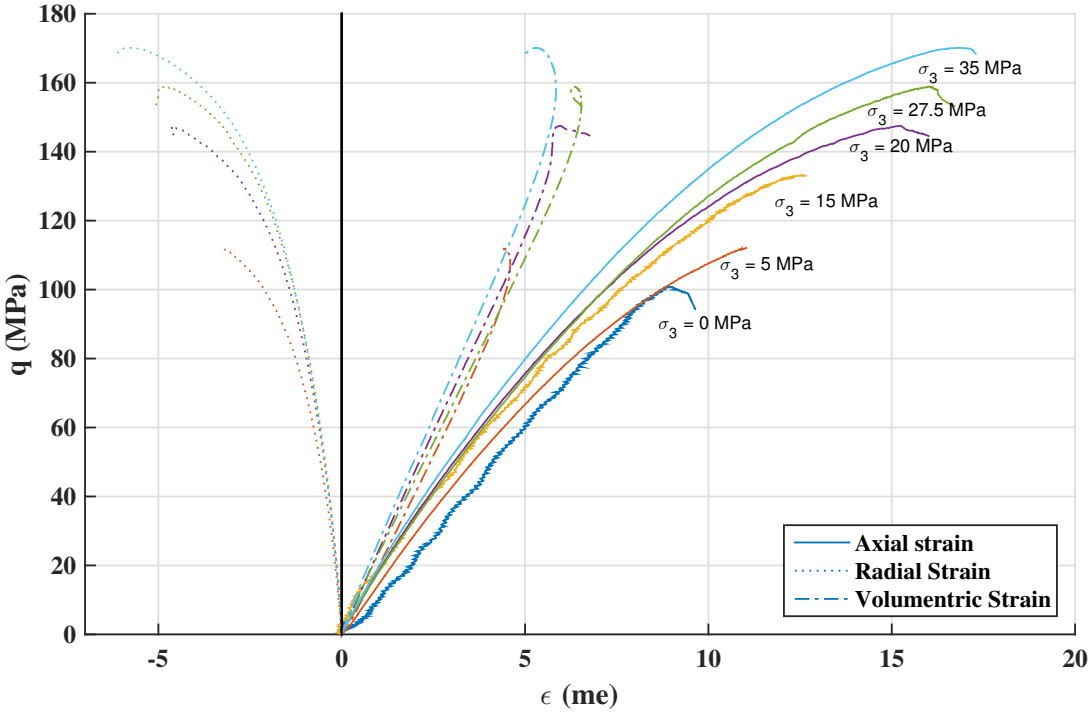

Figure 3.13: **Single Stage triaxial experimental results of Marcellus Shale at room temperature**

Static moduli E_v and ν_{vh} were estimated from initial modulus as shown in Figure 3.9. Monotonic increase is observed for Young's modulus E_v with increasing hydrostatic pressure (Figure 3.14), reaching a plateau around $\sigma_3 \sim 25$ MPa, where E_v ~19 GPa. It is commonly accepted that the occurrence of cracks in rocks reduces the effective Young's modulus, since stress cannot be transferred across the crack itself (Fjær. et al. 2008). As pressure increases, more and more cracks close and, eventually, effective Young's modulus reaches a constant value. Poisson's ratio ν_{vh}, on the other hand, does not show any dependence with hydrostatic pressure (Figure 3.14), exhibiting a mean value of ν_{vh} ~0.15.

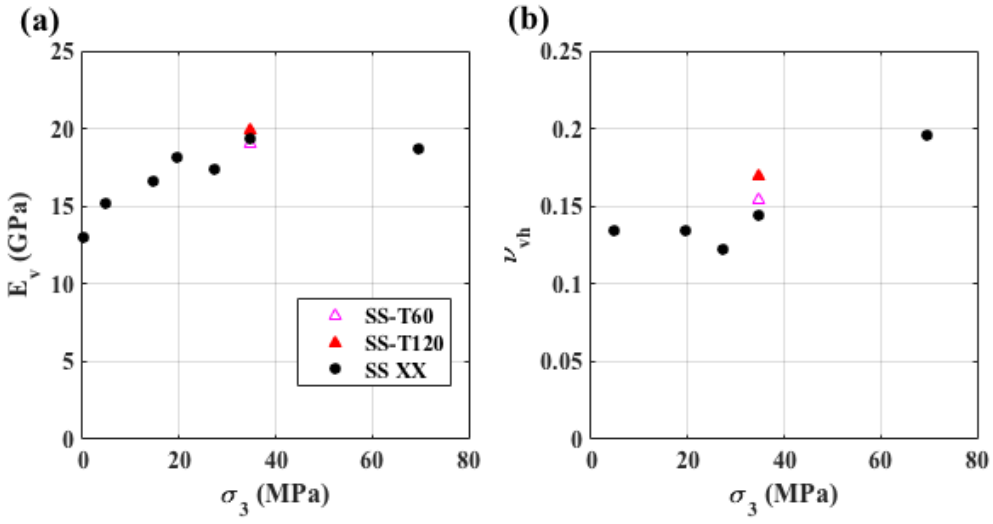

Figure 3.14: **Effect of confining pressure on static moduli of Marcellus Shale. (a) Young's modulus and (b) Poisson's ratio vs. confining pressure. Initial moduli are estimated by linear regression from Single Stage triaxial tests.**

Failure in these shales was found to be brittle. Except for SS27, catastrophic failure occurred during shear band formation, accompanied by a significant drop in differential pressure. Strength data for individual tests can be found in Table 3.3. Figure 3.15(a) presents the effect of confining pressure on both crack damage threshold (σ_{1d}) and failure

strength (σ_{1f}). While intact strength of the rock increases linearly with confinement, the non linear trend of σ_{1d} amplifies the stress difference between the onset of rock volume dilation and the failure point (i.e. $\sigma_{1f} - \sigma_{1d}$). This suggests that, under relatively low confinement conditions, failure occurs as soon as new fractures are opened (resulting from application of deviatoric load), whereas increasing confining stress prevent the rapid coalesce of newly-created microfractures and, therefore, delay failure. The brittle nature of these rocks is reflected in the small difference between σ_{1f} and σ_{1u}. Moreover, from Figure3.15(b) one can see that both axial and radial peaks have a good linear relation with the confining pressure.

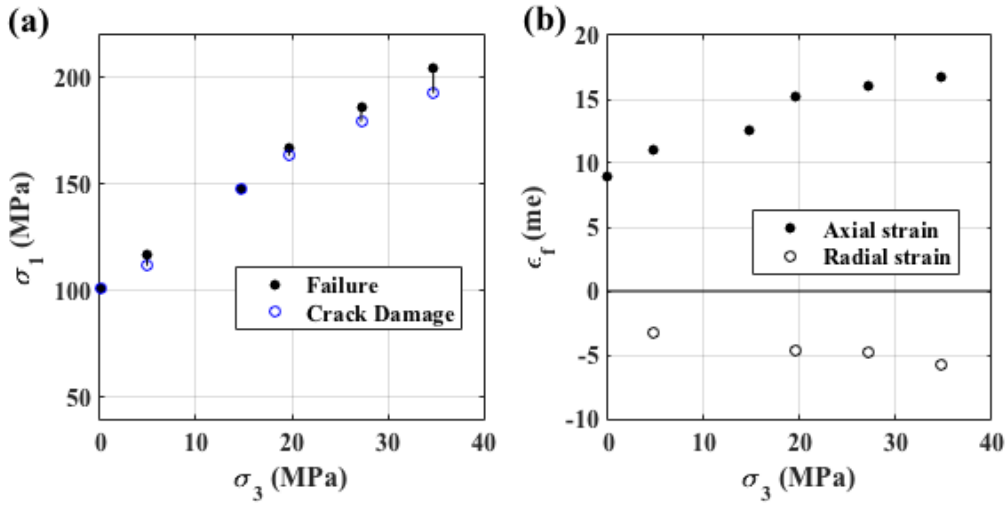

Figure 3.15: **Effect of confining pressure on strength of Marcellus Shale. (a) Crack damage threshold, Failure strength, and (b) Strain at failure vs. confining pressure. Vertical solid lines in (a) illustrates how the difference $\sigma_{1f} - \sigma_{1d}$ grows with increasing confinement**

Post-mortem analysis of the cores were conducted through X-ray Computed Tomography (CT-scans). Figure 3.16 shows CT-scans images for three single stage tests at 0, 20 and 35 MPa of confining pressure. The orientation of the failure plane (β) relative to the major

principal stress (coincident with cylindrical axis) was measured from these images, and found to be approximately 63^o. Fracture patterns reveal that under unconfined conditions failure occurs by a combination of tensile and shear mechanisms, whereas shear is the principal fracture mechanisms under confinement. This suggests that confining stress prevents the aperture of vertical tensile fractures. Important to note, is the presence of planes of weakness parallel to bedding.

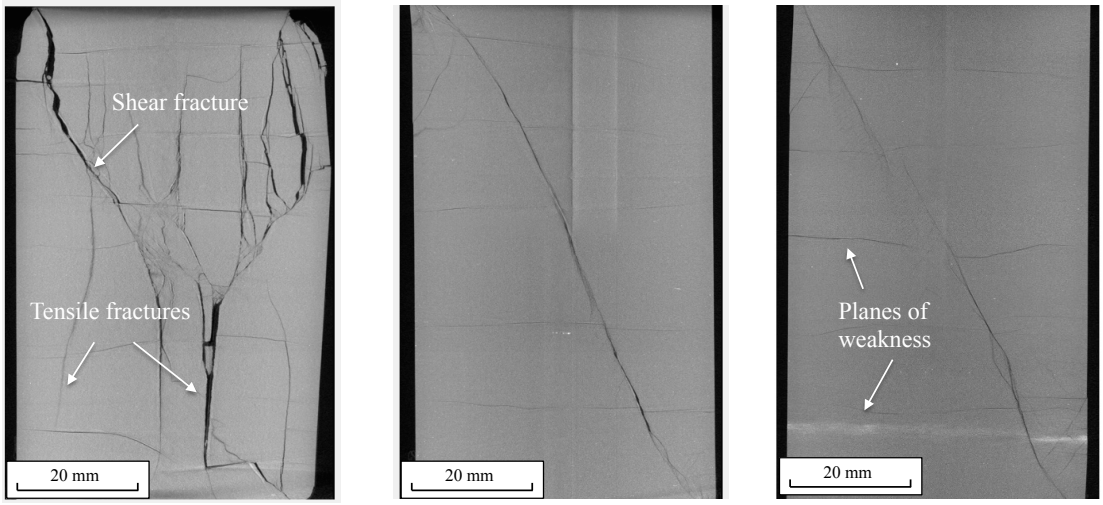

Figure 3.16: **Post-mortem X-ray CT- scanning images of Marcellus Shale after Single Stage triaxial compression experiments (room temperature). Failure under unconfined conditions occurs by a combination of tensile and shear mechanisms, whereas shear is the principal fracture mechanism under confinement. Note the presence of planes of weakness parallel to bedding.**

3.4.2 High Temperature Tests

Results of high temperature single stage triaxial tests are shown in Tables 3.2 and 3.3, and Figures 3.12, 3.14, 3.17 and 3.19. Prior triaxial loading, and after confining pressure was increased to 35 MPa following a multistep-wise loading path (Figure 3.12(a)), temperature was ramped to 60 ^{o}C and 120 ^{o}C during the thermal consolidation stage. Figure 3.17 shows the results of this thermal consolidation stage for both high temperature tests (SS-T60 and SS-T120). By inspection of the strain-time history, one can notice the small strain response to temperate of these rocks. Initially, both samples expands axially but, even before temperature stabilizes, expansion trend turns into compaction. On the contrary, radial strains only show compaction. This is probably a combination of the residual effect of the hydrostatic stage, and the shale small response to temperature.

Figure 3.18 further explores the impact of temperature on mechanical response to deviatoric load. Both tests, SS-T60 and SS-T120, are compared with SS35 (room-temperature). All strength parameters (σ_{1d}, σ_{1f}, and σ_{1u}) are found to decrease with increasing temperature. Fracture patterns (Figure 3.19) are very similar to those identified in SS tests, and failure angles were found to be roughly 57^o and 66^o. On the other hand, temperature does not seem to affect static moduli (Figure 3.14). We believe that any change in mechanical behavior during SS-T60 and SS-T120 tests (compared to SS35), can be directly attributed to temperature effects since both samples showed exactly the same stiffness as SS35 during isotropic compression (Figure 3.12(a)) , and therefore sample variability can be dismissed.

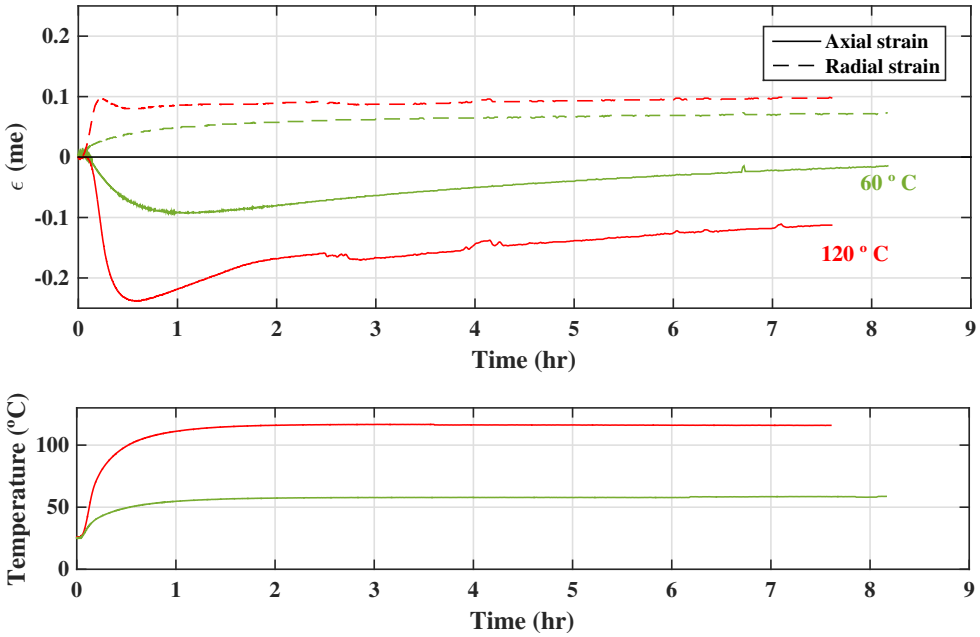

Figure 3.17: **Thermal Consolidation Stage**

3.4.3 Multi-stage Triaxial Tests

Sample variability, indeed, may prevent the assessment of the impact of reservoir conditions (e.g. pressure, temperature, saturation, etc.) on the geomechanical behavior. Multi stage tests may help us to eliminate that sample variability. The Elastic Multi-Stage (MSE) triaxial test was designed in order to study the effect of confining pressure on the non-linear elastic behavior of shale rocks, through a number of loading and unloading cycles at different confining levels. Meanwhile, Failure Multi-Stage (MSF) triaxial aimed for the full estimation of the failure envelope from a single sample. A summary of test specimens and results is included in Tables 3.4 and 3.5 for elastic and failure multi-stage test respectively.

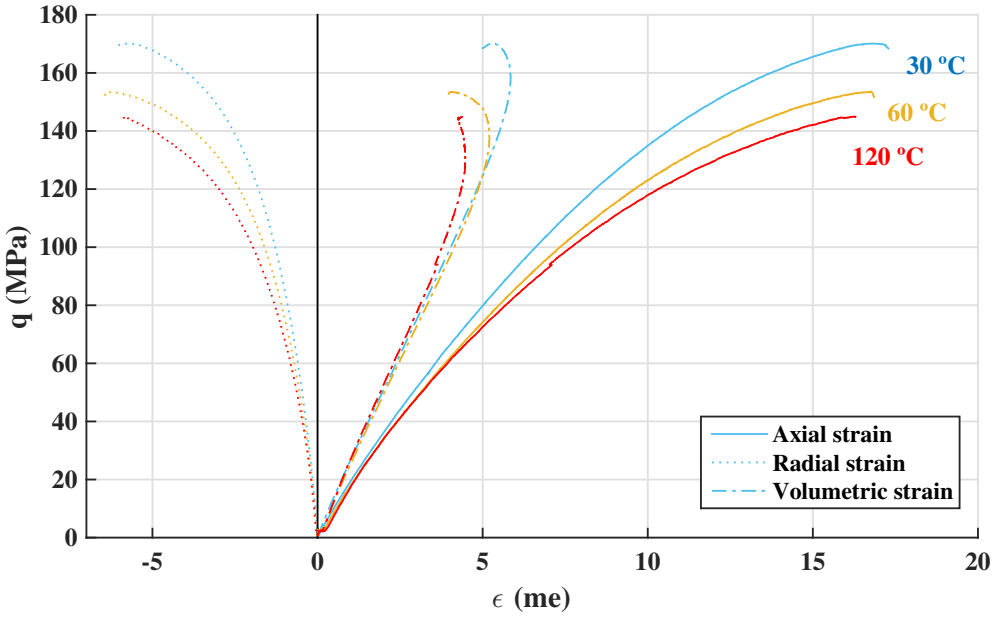

Figure 3.18: **Single Stage triaxial experimental results of Marcellus Shale at high temperature**

(A) Elastic Multi-Stage Triaxial

A preliminary analysis of stress-strain plots in Figure 3.20 reveals a significant non-linear behavior in these shales, especially at low confinement levels. Here, the stress-strain plots are presented for all 9 stages (i.e. σ_3 = 0, 5, 10, 20, 30, 40, 50, 60, and 70 MPa). First, the initial non-linear behavior resulting from the closure of soft pore spaces and microcracks is significant. This behavior is attenuated as confining pressure increases, leading to the closure of microcracks prior experiencing any deviatoric loading. Moreover, permanent plastic deformation seems to be reduced for subsequent stages. This may be due to increasing confining pressure, successive cycling, or a combination of both. Higher confinement also decreases the non-linear behavior at higher deviatoric stress levels (this

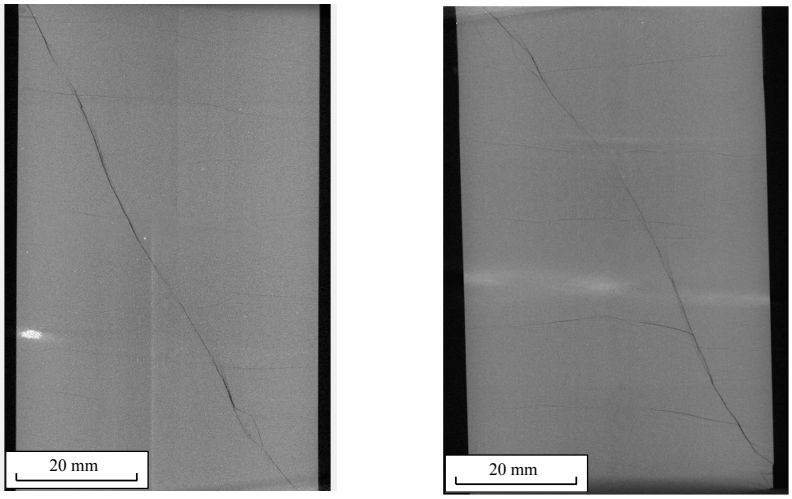

Figure 3.19: **Post-mortem X-ray CT- scanning images of Marcellus Shale after single stage triaxial compression experiments at High Temperature.**

can be easily seen in the reduction of the area enclosed between loading and unloading curves). Finally, larger Young's modulus is observed with increasing confining pressure.

Figure 3.21(a) shows initial Young's modulus versus confining pressure (i.e. estimated from $q \in$ [5,15 MPa], non-linear initial portion of the curve is neglected). As expected, E_v increases with σ_3. However, unlike single stage tests, no plateau is reached but a monotonic increase in Young's modulus is observed at high confining levels. This is in good agreement with what was observed for the bulk modulus. We believe that this trend was not observed during single stage experiements due to sample variability.

Table 3.4: **Elastic Multi-Stage Triaxial test results. Static moduli are estimated from the first cycle (loading-unloading-reloading) of each pressure stage**

Test ID	Core			Test Conditions		Static Moduli	
	Ratio L:D	ρ (g/cc)	Depth (ft)	σ_3 (MPa)	T (^{o}C)	E_v (GPa)	ν_{vh}
MSE	1.8	2.59	360	0	30	7 - 7	-
				5		11 - 15	0.07 - 0.08
				10		16 - 20 - 18	0.10 - 0.12 - 0.12
				20		20 - 24 - 22	0.14 - 0.15 - 0.14
				30		20 - 25 - 23	0.15 - 0.16 - 0.15
				40		21 - 25 - 23	0.16 - 0.16 - 0.16
				50		22 - 25 - 24	0.16 - 0.16 - 0.16
				60		23 - 25 - 25	0.16 - 0.16 - 0.16
				70		23 - 26 - 25	0.16 - 0.16 - 0.16

Table 3.5: **Failure Multi-Stage Triaxial test results**

Test ID	Core			Test Conditions		Static Moduli		Strength			
	Ratio L:D	ρ (g/cc)	Depth (ft)	CP (MPa)	T (^{o}C)	E_v (GPa)	ν_{vh}	σ_{1d} (MPa)	σ_{1f} (MPa)	ϵ_{af} (me)	σ_{rf} (me)
MSF	1.8	2.59	325	5	30	16	0.12	-	112.5	8.1	-1.6
				20		20	0.14	-	161.6	10.8	-2.8
				27.5		20	0.14	180.8	185.8	13.0	-4.0

Even though when they are estimated over the same deviatoric pressure amplitude, Young's modulus upon unloading is systematically higher than upon loading. Loading introduces both elastic and inelastic strains, which are not recovered upon unloading where mostly elastic deformation occurs. Hence, the unloading stiffnesses are higher that loading ones, and quite similar to dynamic estimates (Zoback 2007).

For our samples, Poisson's ratio (Figure 3.21(b)) seems to be very pressure independent once retrieval and sample preparation induced microfractures are closed, in conformity with single stage tests. Low ν_{vh} values observed at initial stages are likely due to the initial

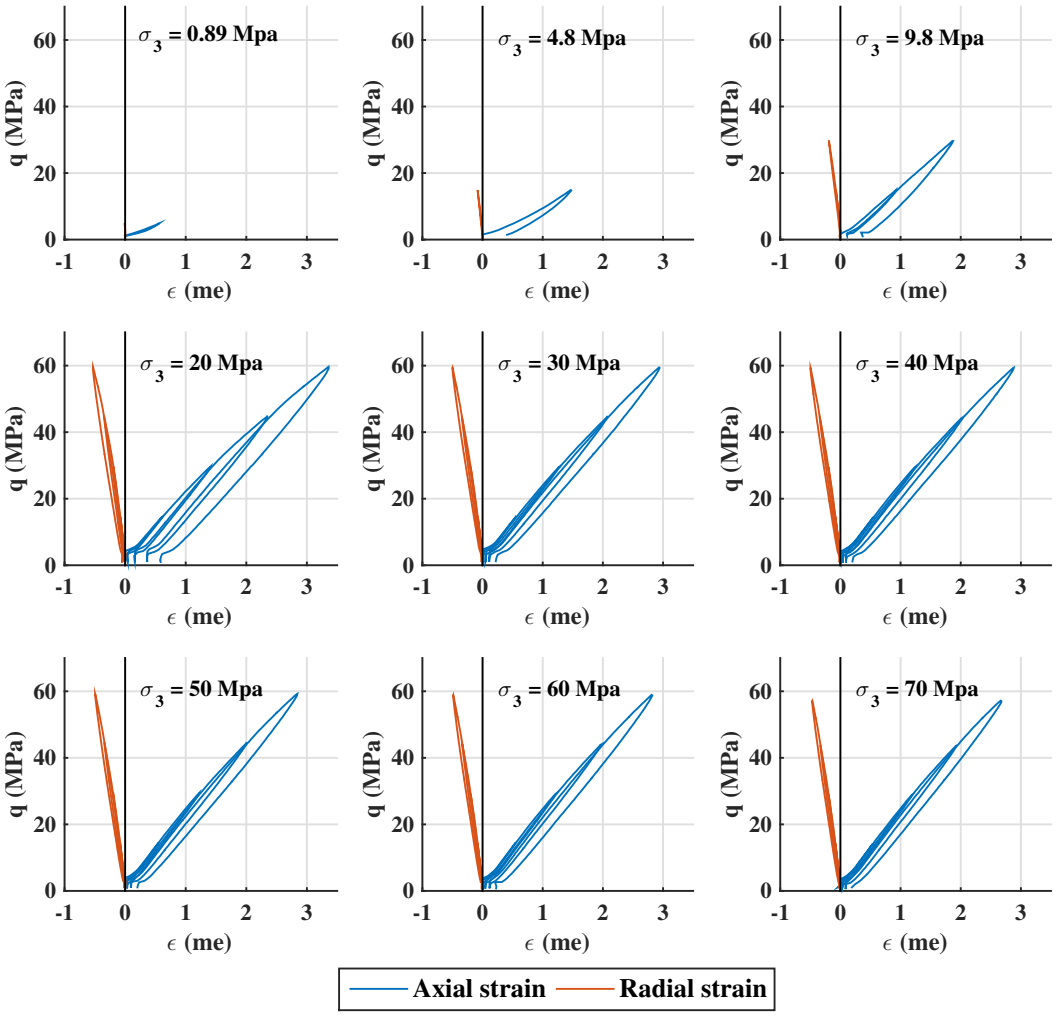

Figure 3.20: **Elastic Multi-Stage triaxial test results. Stress-strain plots for all 9 stages ($\sigma_3 = 0 - 70$ MPa).**

closure of horizontal induced fractures. At these stages, radial strain is almost negligible compared with axial strain. No significant difference was observed among Poisson's ratios estimated upon loading, unloading or reloading.

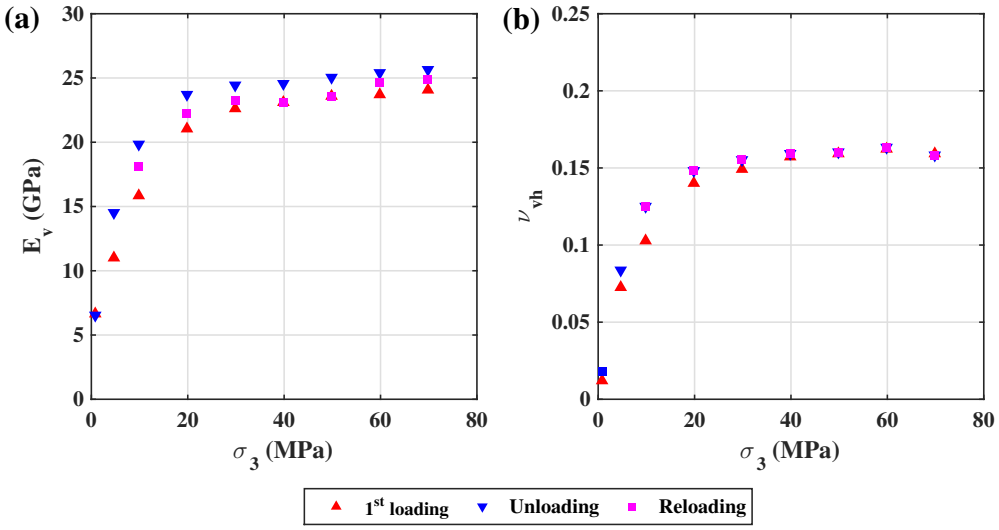

Figure 3.21: **Elastic moduli from Elastic Multi-Stage test (MSE). (a) Young's modulus and (b) Poisson's ratio vs. confining pressure. 1st-loading and unloading parameters are estimated by linear regression from the first cycle of each stage (i.e. DS = 5-15 MPa), while reloading parameters correspond to initial moduli of the second cycle.**

(B) Failure Multi-Stage Triaxial

Results from Failure Multi-Stage (MSF) triaxial compression test can be found in Table 3.5 and Figures 3.22, 3.23 and 3.25. Given the brittle nature of these shales, execution of this test was very difficult. Hence, data from only three stages (σ_3 = 5, 20 and 27.5 MPa) were recovered. Failure identification was based on visual inspection of the $\sigma_1 - \epsilon_a$ curves (Figure 3.22). Sample and test specifications, along with experimental results, are summarized in Table. 3.5. Elastic moduli are in close agreement with those estimated from SS and MSE tests. Strength parameters (3.23) followed similar trends to those obtained from SS tests (Figure 3.15), and peak strength values fall within expected range. The post-mortem CT-scan image of MSF test (Figure 3.25) shows a more fractured sample compared to the

SS test, exhibiting both shear (β = 62^o) and horizontal fractures coinciding with planes of weakness.

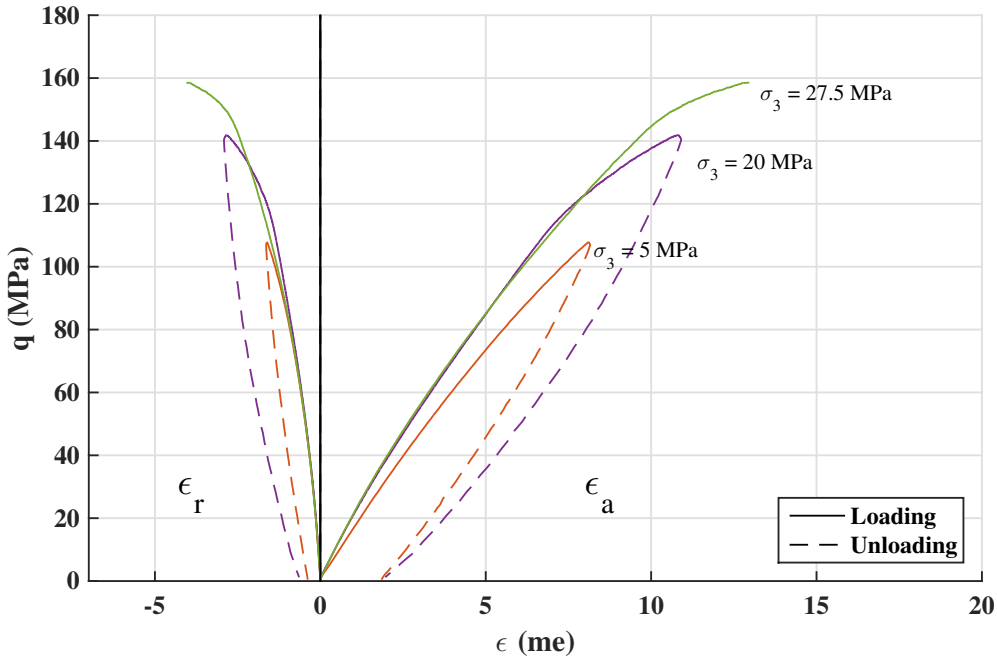

Figure 3.22: **Failure Multi-Stage triaxial test results. Deviatoric stress vs. Axial and Radial strain curves for 3 different confinement levels (σ_3 = 5, 20 and 27.5 MPa). The sample was taken to failure at last stage.**

The crack damage threshold could not be obtained from the two first stages (σ_3 = 5 and 20 MPa) since deviatoric load was removed prematurely. Nevertheless, we are confident that the sample was very close to failure as this occurs immediately after σ_{1d} at at low confinement levels (Figure 3.15), and we believe that the deviatoric load was removed just in the vicinity of this value (Figure 3.24).

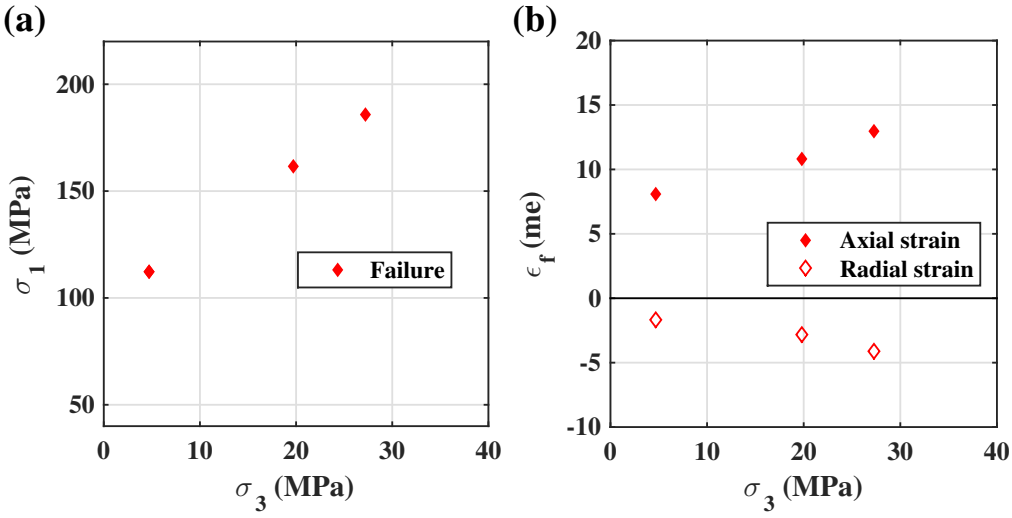

Figure 3.23: **Strength parameters from Failure Multi-Stage test (MSF). (a) Failure strength, and (b) Strain at failure vs. confining pressure.**

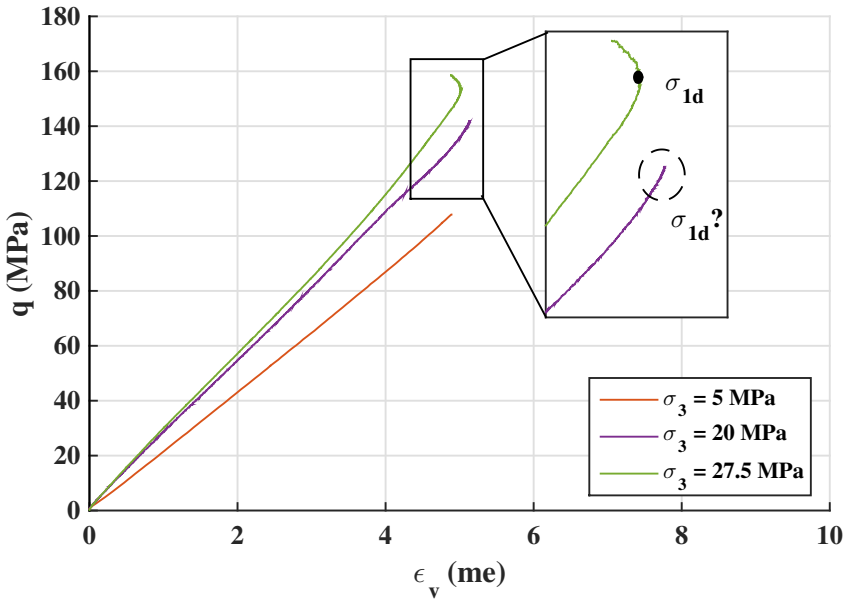

Figure 3.24: **Volumetric strain curves for Failure Multi-Stage tests. Deviatoric load was removed in the vicinity of σ_{1d} for the two first stages.**

MSF

$\beta = 62^{o}$

Figure 3.25: **Post-mortem X-ray CT- scanning images of Marcellus Shale after Failure Multi-Stage triaxial test.**

3.5 Discussion

3.5.1 Pressure Dependency and Non-linearity of Stiffness

Interpretation of shale stiffness from the stress-strain response of triaxial test is not a trivial task. Firstly, the use of the term *stiffness* may lead to confusion because of its general association with *elasticity*, and with the even more general *linear elasticity* (Wood 2004), which is clearly not what we observed. Other studies (Zoback and Byerlee 1975, Sone 2012) have pointed that not only mineral elastic deformation occurs during static measurements, but also energy-dissipative inelastic deformation is induced as a result

of frictional sliding and microcrack growth. This additional plastic deformation clearly changes the structure of the rock, softening the Young's modulus and reflecting material degradation. Moreover, the presence of microcracks, and other defects, may enhance this non-linear behavior.

Pressure Dependency of Stiffness

Previous laboratory analysis and theoretical models have suggested that rock stiffness is a function of the stress state. It was shown in Figures 3.12, 3.14 and 3.21 that shale stiffness increases with confining pressure. This had been corroborated by ultrasonic experiments (Sarout and Guéguen 2008b, Kuila et al. 2011, Dewhurst et al. 2011) where all velocities were found to increase with increasing isotropic stress. In our results, the initial non-linear trend is likely due to the closure of the stress-relief and coring induced cracks (Figure 3.2(b)). Once these 'soft' cracks are closed (around ~ 15 MPa of confining pressure), the initial moduli estimated from both SS and MSE tests show a similar dependency with σ_3, as it can be seen in Figure 3.26.

Figure 3.21(a) compares static Young's modulus estimated upon 1^{st}-loading (E_l), unloading (E_u), and reloading (E_r) during MSE test. Unloading Young's moduli values are about 12% higher on average than E_l. This difference decreases exponentially from 33% (at σ_3 = 5 MPa) to 8% (at σ_3 = 30 MPa) and then keeps constants, suggesting that most of plastic deformation (and/or non-linear crack closure) occurs within the four first stages (i.e. σ_3 = 0$\sim$20 MPa) of the MSE test. Meanwhile, E_r shows intermediate values in between E_l and E_u. Hence, E_u and E_r better reflect the actual elastic behavior of the

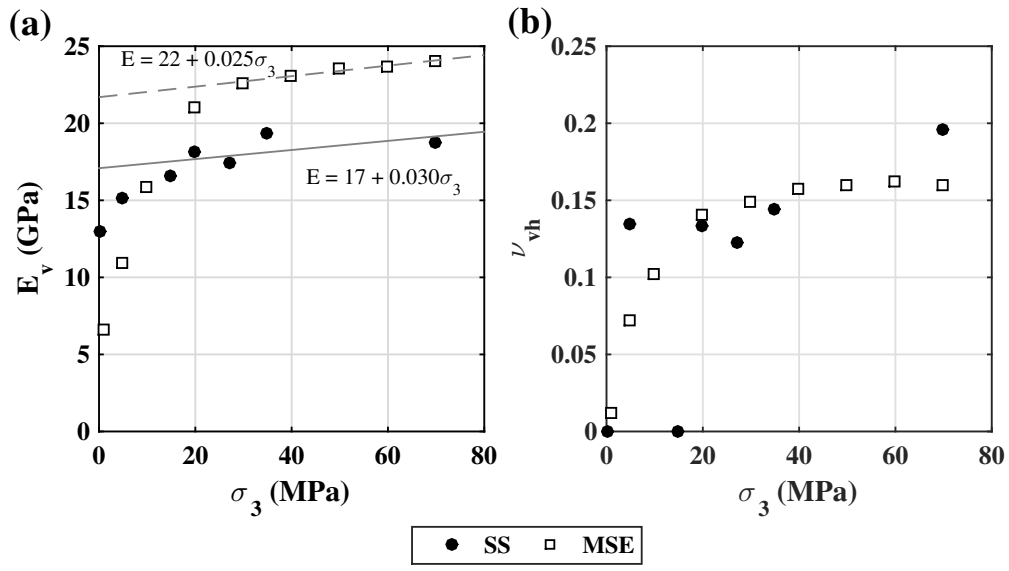

Figure 3.26: **Comparison of static moduli estimated from Single Stage (SS) and Elastic Multi-Stage (MSE) triaxial experiments. (a) Young's modulus and (b) Poisson's ratio vs. confining pressure.**

rock. Sone and Zoback (2013) demonstrated that the unloading/reloading static moduli plots have a one-to-one correspondence in the static-dynamic relations (Sone and Zoback 2013a).

Non-linear Behavior

The deviatoric load may have different effect depending on the amplitude of the load and the direction relative to the bedding. For instance, Kuila et al. (2011) showed that deviatoric loading in the direction perpendicular to the bedding will initially contribute to the closure of cracks oriented parallel to the bedding (increasing stiffness in that particular direction). However, as deviatoric load increases, new cracks perpendicular to the bedding (i.e. parallel to the applied load) will be opened, softening material stiffness.

Therefore, stiffness cannot be uniquely defined for non-linear materials, not even at a given stress level. Non-linear behavior is commonly described by stiffness vs. strain plots (Figure 3.27), which are actually recommended to fully characterize the mechanical behavior. Figure 3.27(a) shows a fairly linear decay of static Young's modulus with axial strain, for most part of the loading. This constant decay does not exhibit any dependence with confinement. Also, note the initial non-linear behavior (sample stiffening) in SS05 and SS20 tests due the stress-relief cracks closure.

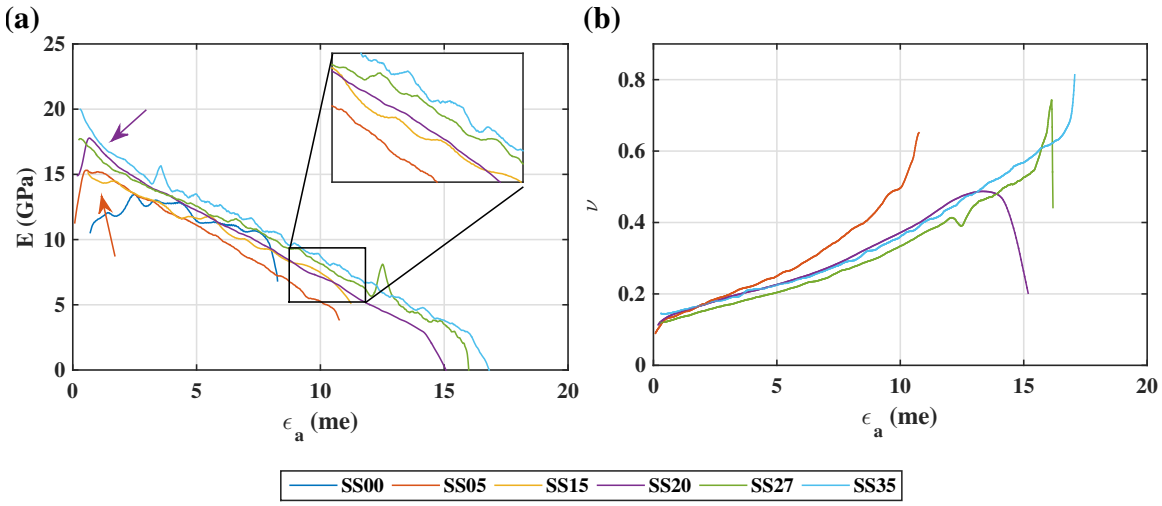

Figure 3.27: **Variation of tangent stiffness of Marcellus Shale in monotonic shearing during Single Stage tests. (a) Static Young's modulus and (b) Poisson's ratio. Arrows point at initial non-linear behavior (sample stiffening).**

Moreover, although plasticity is often sought as the dominant source of nonlinearity, we should acknowledge that some of the truly elastic properties of the shale vary with stress and strain levels (Sarout and Guéguen 2008b, Kuila et al. 2011, Dewhurst et al. 2011). This is especially evident in the MSE test. Figure 3.28 shows the variation of the tangent stiffness due to application of deviatoric load within each confining stage. While one could attributed the apparent *stiffness softening* to the plastic strain at early stages (say $\sigma_3 = 0 \sim 20$

MPa), this would not be completely true at latter stages where plastic deformation is not significant (see Figure 3.20). Nevertheless, a consistent decrease of E_l with deviatoric load is observed for all stages.

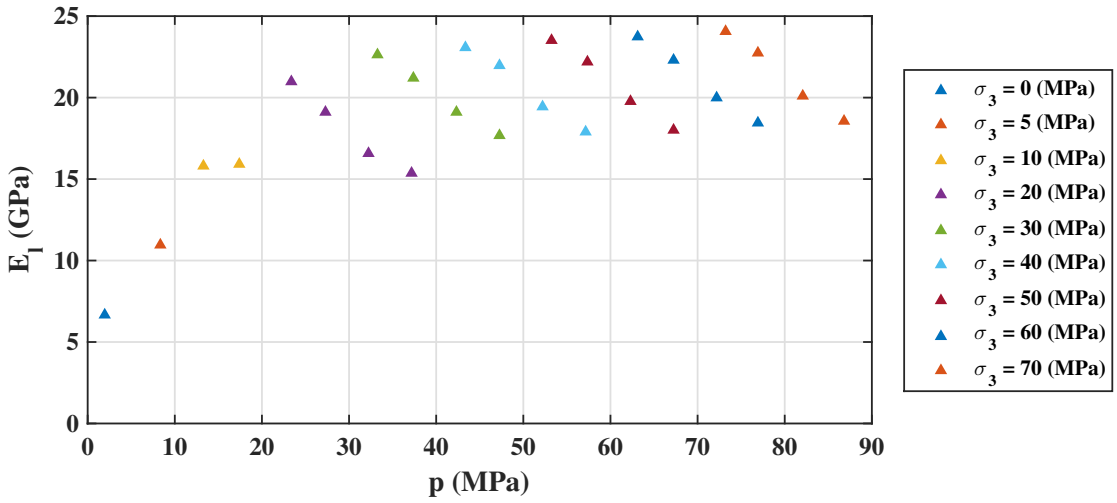

Figure 3.28: **Variation of tangent stiffness of Marcellus Shale during a Elastic Multi Stage test. Each series represents the static Young's modulus estimated during 1^{st}-loading at different deviatoric stress levels. While stiffness increases with confining pressure, σ_3, it also decreases within each stage upon deviatoric loading.**

Meanwhile, Poisson's ratio (Figure 3.27(b)) exhibit a non-linear increase with axial strain up to ν = 0.5, a point where the crack damage threshold is reached. Then, ν continues increasing at a constant rate until the failure onset, where a drastic growth occurs. This is observed for all tests but SS20, where ν decreases after σ_d is reached. Increase in Poisson's ratio is likely to be due the opening of new cracks parallel to maximum principal stress (which enhances radial strain). No dependency with confining pressure is observed.

3.5.2 Anisotropy

Full characterization of geomechanical behavior of VTI media through static measurements is only possible when rock specimens cored in different directions are available. In order to get around the obstacle, we have made use of the VTI coupling model in the triaxial space (Equation 3.3). This model incorporates de coupling modulus J, to acknowledge the contributions of mean and distortional stress increments to distortional and volumetric strains respectively. During isotropic compression, $\delta q = 0$, J gives us an idea of how much axial and radial strains increments differ. Recall, that for isotropic materials axial and radial strain increments are equal upon hydrostatic loading. Therefore, the more isotropic the material is, the higher the absolute value of J should be. Figure 3.29 shows the evolution of J parameter with increasing confining pressure for SS70 test.

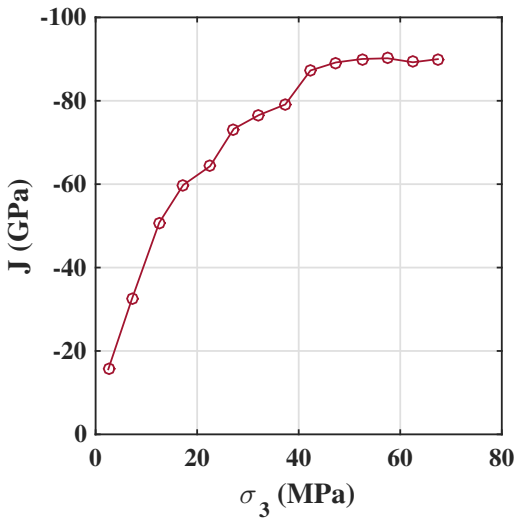

Figure 3.29: **Evolution of the coupling modulus J with increasing confining pressure during SS70 test. Note how the anisotropy degree is reduced (increase in the absolute value of the modulus J) as horizontal microcracks are closed due to increasing confinement.**

As confinement increases, microfractures sub-parallel to bedding are closed first, reducing the compliance in the direction perpendicular to bedding. This stiffening in the axial direction clearly reduces the degree of anisotropy in VTI media. And this is in good agreement with previous experimental studies of shale anisotropy using the single core plug method (Sarout and Guéguen 2008b, Kuila et al. 2011, Dewhurst et al. 2011).

Besides providing some insights about the anisotropy evolution, the J parameter can be used along with K and G, defined in Equation 3.3, in order to estimate the value of the five independent parameters which describe VTI media (Equation 3.1). For instance, if we force certain interdependencies among these five independent parameters (Graham and Houlsby 1983), Equations 3.3.1, 3.3.1 and 3.3.1 can be used to fully characterize VTI media elastic behavior.

3.5.3 Interpretation of Failure Parameters

There are many different ways in which failure data from triaxial tests can be analyzed. For instance, Figure 3.30 presents the failure data in the $\tau - p'$ space using Mohr's circles at failure for SS tests. This allows us to directly interpret both cohesion and the internal friction angle of the rock from the Linearized Mohr-Coulomb (M-C) envelope. The Mohr-Coulomb failure criterion is not only one of the simplest, but also the most widely used criterion in the oil industry.

Furthermore, another common way of presenting strength data are through the $\sigma_1 - \sigma_3$ space (Figure 3.31). The estimated unconfined compressive strength (C_0) for these rocks

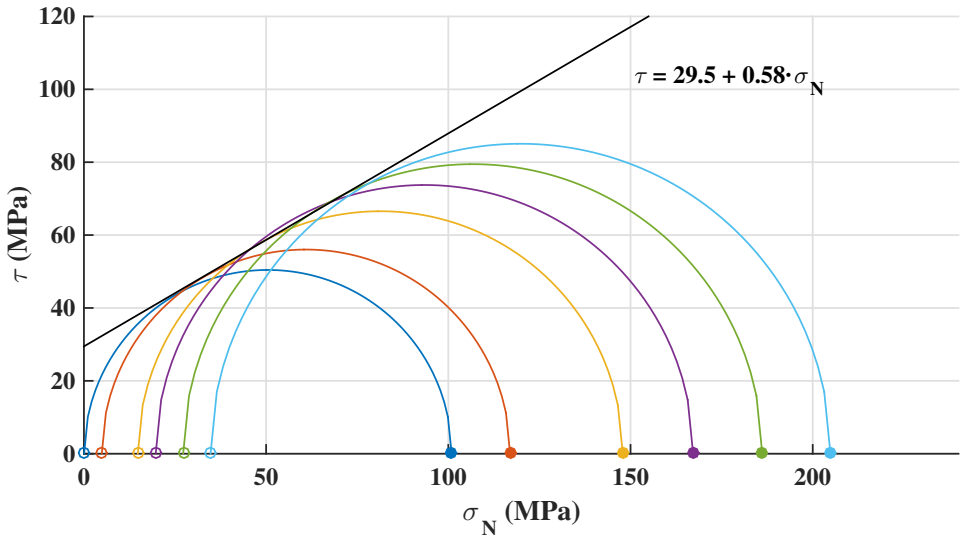

Figure 3.30: **Mohr's circles and failure envelope for Marcellus Shale. Data from Single Stage tests.**

is about 100 MPa, in good agreement with the trend found by Sone and Zoback (2013) given the clay/kerogen content and Young's modulus of our samples. C_0 values for these Marcellus shales fall in the low range found by the latter authors, who characterize a large number of shales from the Barnett, Haynesville, Eagle Ford, and Fort St. John plays (Sone and Zoback 2013a). In contrast, the coefficient of internal friction (ν_i), with a value of about to 0.6, falls in the medium-upper range. On the other hand, the orientation of the failure plane yield by the M-C envelope, $\beta = 60^o$, is within the observed range from the CT-scans (Figure 3.16).

Although the intact strength of these shales was found to behave pretty linearly with confining pressure (σ_3), and the Mohr-Coulomb model fits the data with a reasonably low RMSError value, we also investigated the influence of σ_3 on peak strength of Marcellus shale using the non-linear Hoek & Brown criterion (H-B). Comparison between both M-C

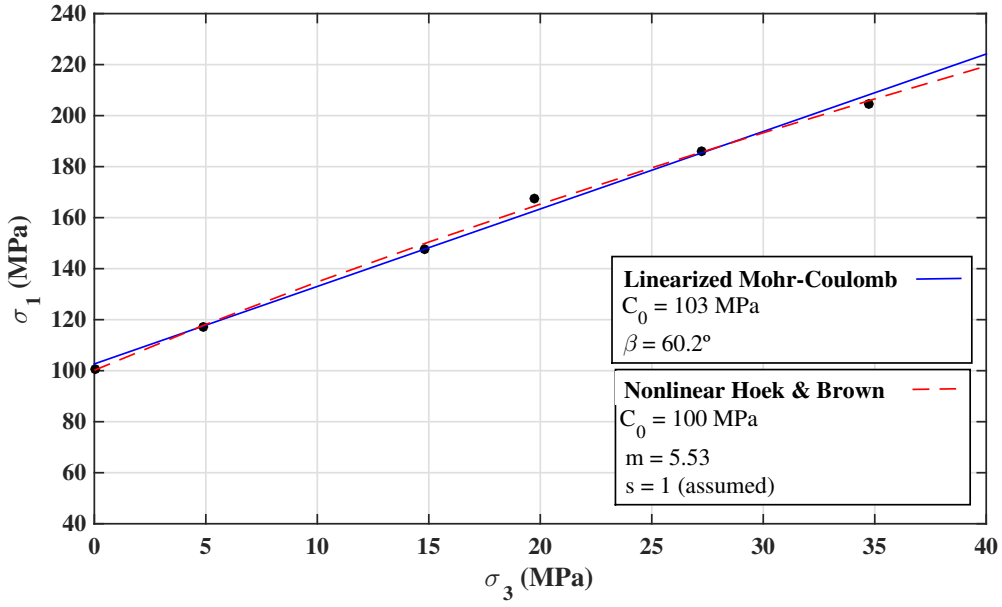

Figure 3.31: **Comparison between the Linearized Mohr-Coulomb and the Empirical Hoek-Brown criteria. Experimental data from Single Stage tests.**

and H-B criteria can be found in Figure 3.31. Model parameters criteria were estimated by least-square regression, and they are presented in Table 3.6. For H-B criterion, by assuming $s = 1.0$ (intact rock), we obtained $C_0 = 100$ MPa and $m = 5.5$, which is a reasonable value for shales (Hoek and Brown 1997). Both criterion are in very good agreement, with the H-B model yielding a slightly lower RMSErr.

Table 3.6: **Mohr-Coulomb and Hoek-Brown criteria parameters for Marcellus Shale.**

Linearized Morh-Coulomb Criterion					**Empirical Hoek-Brown Criterion**			
C_0 (MPa)	β (^{o})	S_0 (MPa)	μ_i	RMS (MPa)	C_0 (MPa)	m	s	RMS (MPa)
103	60.2	29.5	0.58	2.51	100	5.53	1	1.51

Lastly, Figure 3.32 compares the strength parameters measured during SS and MSF experiments. We believe that the close agreement in both stiffness and strength parameters

is due to the relative low number of stages (3), and to the fact that the damage crack threshold was not reached during the two first states. However, the more fractured core resulting from this test (Figure 3.25) might suggest that additional damage occurred during the cyclic loading at high stress levels.

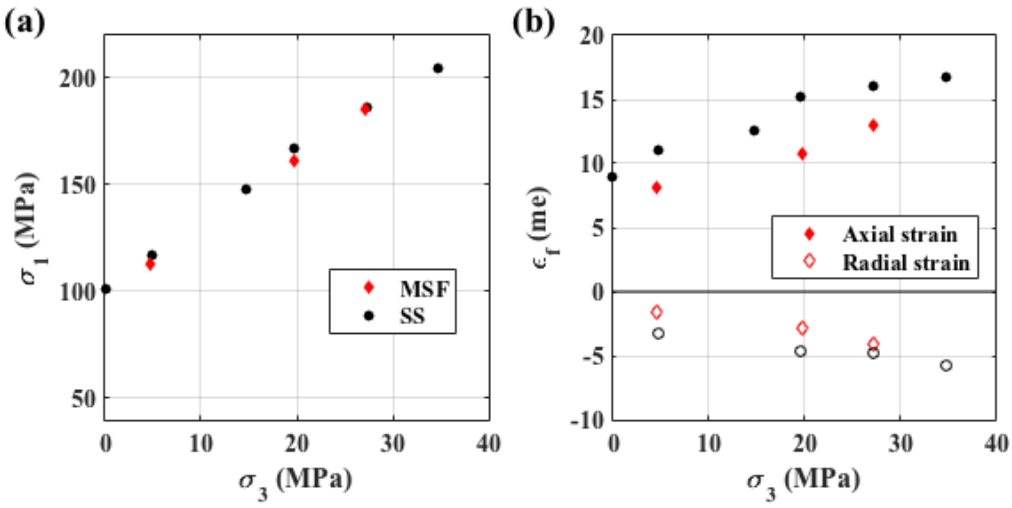

Figure 3.32: **Comparison of stregth parameters measured during Single Stage (SS) and failure Multi-Stage (MSF) triaxial experiments. (a) Failure strength and (b) Strain at failure vs. confining pressure.**

3.5.4 Thermal Effects

The Marcellus shale samples tested in this study have shown a relatively small response to temperature. From the thermal consolidation (Th.C) stage, the linear thermal expansion coefficients (α_T) were estimated for both tests (Table 3.7). We found anisotropic thermal expansion behavior during our tests. It is known that mica minerals and quartz (major constituents of our samples) have a large effect on the anisotropic expansion of rocks (Huotari and Kukkonen 2004).

Table 3.7: **Marcellus shale coefficients of linear thermal expansion (α_T) for the axial and radial directions.**

Test ID	**T** (^{o}C)	α_{Taxial} (K^{-1})	$\alpha_{Tradial}$ (K^{-1})
SS-T60	60	2.9 10^{-6}	1.5 10^{-6}
SS-T120	120	2.2 10^{-6}	1.1 10^{-6}

Experimental results show minimal change in shale stiffness and, limited strength reduction of 8% and 12% at 60 ^{o}C and 120 ^{o}C respectively. Much higher strength (approx. $\sim 40\%$) and stiffness reductions have been reported for colorado shale tested at similar temperature conditions (Mohamadi et al. 2013). Moreover, Bauer et al. (2014) observed significant (up to more than 1%) thermally-induced compaction in Pierre shale (Eseme et al. 2007). We believe that the poor geomechanical response to temperature might be due to the negligible saturation of our samples. Recall, that we used dry samples and the geomechanical behavior in this study just reflect the solid skeleton response to pressure and temperature.

3.6 Conclusions

Marcellus shale samples used in this study were characterized by high clay volume, and moderate total organic content. Mechanical properties and porosity estimates were in good agreement with trends found for other shale gas reservoirs. The fabric in these rocks exhibits primary foliation, and the microstructure reveals a clayey matrix with silt size grains and other various-shape inclusions. The preferential orientation is preserved across scales, presenting a number of stress-relief microcracks oriented sub-parallel to the bedding. It was shown that the presence of such microcracks clearly affects the mechanical behavior of these shales, specially at low confinement levels.

Interpretation of stiffness in these shales is not straightforward given their significant non-linear behavior, and the occurrence of small irrecoverable deformation at small stress levels. Upon isotropic loading, increase in stiffness was observed as a result of the consolidation process and the closure of microcracks. Initial behavior was characterized by high non-linearity, reflecting the closure of soft pore spaces and coring-induced cracks. Static moduli upon unloading were found to be systematically higher than upon loading (+12% on average), due to inelastic strains induced during 1^{st}-loading. During the triaxial stage, application of deviatoric stress perpendicular to the bedding resulted in a linear decay with axial strain for most part of the loading. This decay did not exhibit any dependence with confinement. Nevertheless, it was observed that the truly elastic properties of these rocks vary with stress and strain levels. On the other hand, confining pressure seems to have a limited impact on Poisson's ratio, although this exhibited non-linear increase with monotonic axial loading. Multi stage tests were found as useful tools for the evaluation the stiffness in non-linear elasto-plastic materials.

The laboratory results highlighted the anisotropic nature of these shales, which cannot be dismissed during mechanical characterization. It has been proven that increasing confining pressure clearly reduces the degree of anisotropy. It was shown that the coupling parameter J can be used in order to gain insights about anisotropy evolution.

As for the intact strength of these rocks, we have observed brittle (catastrophic) failure under monotonic loading conditions. Fracture patterns revealed that failure occurs by a combination of tensile and shear mechanisms under unconfined conditions, whereas shear is the principal fracture mechanisms under confinement. Unconfined compression strength of the tested samples was found to be about 100 MPa, and it falls in the low range for shales

gas rocks. In contrast, the coefficient of internal friction (μ_i = 0.6) was estimated to fall within the medium-upper range for shale gas rocks. Whereas the peak strength increases linearly with confining pressure, the crack damage threshold presents a non-linear trend in these rocks. Both Mohr-Coulomb and Hoek-Brown models fit the data very well with a very small RMSErr.

Lastly, the effect of temperature on the mechanical behavior of the solid skeleton of the shale was evaluated. Experimental results revealed a small response to thermal loading, with limited strength reduction ($\sim$10%) and no variation of initial static moduli. We believe that this was due to the relatively low organic content and the dry conditions of our samples.

Nomenclature

σ_1 = Major principal stress (axial stress)

σ_3 = Minor principal stress (confining stress)

p = Mean effective stress (i.e. $p = \frac{\sigma_1+2\sigma_3}{3}$)

q = Deviatoric stress (i.e. $q = \sigma_1 - \sigma_3$)

ϵ_a = Axial strain

ϵ_r = Radial strain

ϵ_v = Volumetric strain (i.e. $\epsilon_v = \epsilon_a + 2\epsilon_r$)

ϵ_s = Distortional strain (i.e. $\epsilon_s = frac23(\epsilon_a - \epsilon_r)$)

σ_d = Crack damage threshold

σ_f = Peak (failure) strength

σ_u = Ultimate strehngth

Note: if d, f, u are accompanied by 1 (e.g. $\sigma_1 d$), this indicates axial pressure (i.e. confining + deviatoric stress)

H.S. = Hydrostatic Stage

MSE = Elastic Multi Stage triaxial test

MSF = Failure Multi Stage triaxial test

SS = Single Stage triaxial test

SST = Single Stage triaxial test at high Temperature

Th.C. = Thermal Consolidation stage

T.S. = Triaxial Stage

VTI = Vertical Transverse Isotropy

Chapter 4

Conclusions and Recommendations

The results presented in this thesis contribute to further the understanding of the mechanical behavior of shale gas rocks. Shale geomechanical properties were explored through an extensive laboratory testing program. A series of hydrostatic and triaxial tests were performed in order to evaluate the elasto-plastic behavior, and and failure response of Marcellus shale under a wide range of pressure and temperature conditions. Additional characterization included mineralogy, porosity, and rock fabric.

Shale rocks are known to be non-linear materials. There are many factors, including induced cracks and their orientation, partial saturation, material heterogeneity and anisotropy, plasticity, strain rate, and temperature that may have an impact on the geomechanical behaviour of these shales. It was shown that the interpretation of stiffness in these shales is not straightforward given their significant non-linear behavior, and the occurrence of small irrecoverable deformation at small stress levels. Mechanical characterization of non-linear elasto-plastic materials is relevant, and it can be successfully

addressed through multi-stage test (eliminating sample variability, and overcoming the problem of sample scarcity).

Ongoing experimental work in the Geo-Energy Lab at UVM (included in the appendices of the present thesis) aims is to investigate the long-term deformation of shales, and how the viscoplastic behavior affects hydrocarbon production. Future research should involve saturation and pore fluid composition impacts on creep behavior. Moreover, full characterization of anisotropic behavior, through either the one core plug method or multiple plugs cored in different directions, would also contribute to the existing understanding of shale geomechanics. If possible, future tests should be conducted on well preserved samples to better characterize in-situ reservoir properties.

Besides experimental work, constitutive modeling of VTI media is an interesting and promising area. We have generated a large volume of data that could be used in the development of such models.

Bibliography

Bauer, A., R. Holt, J. Stenebråten, E. Sø nstebø, and L. Marø en (2014). Thermally Induced Compaction of Shales. In *48th US Rock Mechanics/Geomechanics Symposium*, Minneapolis, Minnesota, USA.

Britt, L. K., J. Schoeffler, and B. Rock (2009). The Geomechanics Of A Shale Play : What Makes A Shale Prospective! In *SPE Eastern Regional Meeting*, Number September, Charleston, WV, pp. 1–9.

Bro, A. (1997). Analysis of multi-stage triaxial test results for a strain- hardening rock. *International Journal ofRockMechanics andMining Sciences 1*(34), 143–145.

Davies, R. J., S. a. Mathias, J. Moss, S. Hustoft, and L. Newport (2012, November). Hydraulic fractures: How far can they go? *Marine and Petroleum Geology 37*(1), 1–6.

Dewhurst, D., J. Saraout, C. Delle Piane, M. Josh, A. Siggins, and M. Raven (2013). Geomechanics and Physics Related to Shale Strength, Stiffness and Anisotropy. In *International Workshop on Geomechanics and Energy – The Ground as Energy Source and Storage Lausanne, Switzerland, 26-28 November 2013*, Number November, Lausanne, Switzerland, pp. 26–28.

Dewhurst, D. N. and A. F. Siggins (2006, April). Impact of fabric, microcracks and stress field on shale anisotropy. *Geophysical Journal International 165*(1), 135–148.

Dewhurst, D. N., A. F. Siggins, J. Sarout, M. D. Raven, and H. M. Nordgå rd Bolå s (2011, May). Geomechanical and ultrasonic characterization of a Norwegian Sea shale. *GEOPHYSICS 76*(3), WA101–WA111.

Engelder, T. (2009). Marcellus 2008: Report card on the breakout year for gas production in the appalachian basin. *Fort Worth Basin Oil and Gas Magazine* (20).

Eseme, E., J. Urai, B. Krooss, and R. Littke (2007). REVIEW OF MECHANICAL PROPERTIES OF OIL SHALES : IMPLICATIONS FOR EXPLOITATION AND BASIN MODELLING. *Oil Shale 24*(2), 159–174.

Fairhurst, C. (2014). Thinking deeper.

Fjær., E., R. Holt, P. Horsrud, A. Raaen, and R. Risnes (2008). *Petroleum Related Rock Mechanics* (2nd ed.). Amsterdam, The Netherlands: Elsevier Ltd.

Ghassemi, A. (2012, May). A Review of Some Rock Mechanics Issues in Geothermal Reservoir Development. *Geotechnical and Geological Engineering 30*(3), 647–664.

Ghassemi, A. and R. Suarez-Rivera (2012). Sustaining Fracture Area and Conductivity of Gas Shal Reservoirs for Enhancing Long-Term Production and Recovery. Technical report, Research Partnership to Secure Energy for America, College Station, TX.

Graham, J. and G. Houlsby (1983). Anisotropic elasticity of a natural clay. *Geotechnique 33*, 165–180.

BIBLIOGRAPHY

Hoek, E. and E. Brown (1997). Practical estimates of rock mass strength. *International Journal of Rock Mechanics and Mining Sciences 34*(8), 1165–1186.

Hoek, E. and E. T. Brown (1980). Empirical strength criterion for rock masses. *J. Geotechnical Engineering Div.* (106), 1013–1035.

Horsrud, P. (2001). Estimating Mechanical Properties of Shale From Empirical Correlations. (June).

Huotari, T. and I. Kukkonen (2004). Thermal expansion properties of rocks: Literature survey and estimation of thermal expansion coefficient for olkiluoto mica gneiss. Technical report, Geological Survey of Finland.

Islam, M. A. and P. Skalle (2013, March). An Experimental Investigation of Shale Mechanical Properties Through Drained and Undrained Test Mechanisms. *Rock Mechanics and Rock Engineering 46*(6), 1391–1413.

Jacobi, D., M. Gladkikh, B. Lecompte, G. Hursan, F. Mendez, J. Longo, S. Ong, M. Bratovich, G. Patton, B. Hughes, and P. Shoemaker (2008). Integrated Petrophysical Evaluation of Shale Gas Reservoirs. In *CIPC/SPE Gas Technology Simposium 2008 Joint Conference*, Calgary, Alberta, Canada, pp. 1–23. SPE.

Jaeger, J. C. and N. G. W. Cook (1979). *Fundamentals of Rock mechanics*. New York: Chapman and Hall.

Josh, M., L. Esteban, C. Delle Piane, J. Sarout, D. Dewhurst, and M. Clennell (2012, June). Laboratory characterisation of shale properties. *Journal of Petroleum Science and Engineering 88-89*, 107–124.

Kargbo, D. M., R. G. Wilhelm, and D. J. Campbell (2010, August). Natural gas plays in the Marcellus Shale: challenges and potential opportunities. *Environmental science & technology 44*(15), 5679–5684.

King, G., L. Haile, J. Shuss, and T. Dobkins (2008). Increasing fracture path complexity and controlling downward fracture growth in the barnett shale. SPE.

Kovari, K. and A. Tisa (1975). Multiple failure state and strain controlled triaxial tests. *Rock Mechanics and Rock Engineering 1*(7), 17–33.

Kuila, U., D. Dewhurst, a.F. Siggins, and M. Raven (2011, April). Stress anisotropy and velocity anisotropy in low porosity shale. *Tectonophysics 503*(1-2), 34–44.

Lings, M., D. Pennington, and D. Nash (2000). Anisotropic stiffness parameters and their measurement in a stiff natural clay. *Geotechnique 50*(2), 165–180.

Loucks, R. G., R. M. Reed, S. C. Ruppel, and D. M. Jarvie (2009). Morphology, genesis, and distribution of nanometer-scale pores in siliceous mud- stones of the mississippian barnett shale. *Journal of Sedimentary Research* (79), 848–861.

Mavko, G., T. Mukerji, and J. Dvorkin (2009). *The Rock Physics Handbook. Tools for Seismic Analysis of Porous Media* (2nd ed.). New York, US: Cambridge University Press.

Maxwell, S. (2011). Microseismic hydraulic fracture imaging: The path toward optimizing shale gas production. *The Leading Edge 30*(3), 340–346.

BIBLIOGRAPHY

Mohamadi, M., X. Gong, and R. G. Wan (2013). Laboratory and Constitutive Modeling of Colorado Shale at High Pressure and Temperature. In A. R. M. Association (Ed.), *47th US Rock Mechanics / Geomechanics Symposium*, San Francisco, CA, USA, 23-26 June 2013, pp. 1–8.

Moronkeji, D., U. Prasad, and J. Franquet (2014). Size Effects on Triaxial Testing from Sidewall Cores for Petroleum Geomechanics. In *48th US Rock Mechanics/Geomechanics Symposium*.

Passey, Q. R., K. M. Bohacs, W. L. Esch, R. Klimentidis, S. Sinha, and E. Upstream (2010). From Oil-Prone Source Rock to Gas-Producing Shale Reservoir – Geologic and Petrophysical Characterization of Unconventional Shale-Gas Reservoirs. In *CPS/SPE International Oil & Gas Conference and Exhibition in China 2010*, Beijing, China, pp. 1707–1735. SPE.

Puzrin, A. M. (2012). *Constitutive Modelling in Geomechanics*.

Rickman, R., M. Mullen, E. Petre, B. Grieser, , and D. Kundert (2008). A practical use of shale petrophysics for stimulation design optimization: All shale plays are not clones of the barnett shale. In *SPE Annual Technical Conference and Exhibition, Denver, Co, September 21-24, 115258.*

Salager, S., B. François, M. Nuth, and L. Laloui (2012, September). Constitutive analysis of the mechanical anisotropy of Opalinus Clay. *Acta Geotechnica 8*(2), 137–154.

Sarout, J. and Y. Guéguen (2008a). Anisotropy of elastic wave velocities in deformed shales : Part 2 — Modeling results. *Geophysics 73*(5), D91–D103.

Sarout, J. and Y. Guéguen (2008b, September). Anisotropy of elastic wave velocities in deformed shales: Part 1 — Experimental results. *Geophysics 73*(5), D75–D89.

Schmitt, L., T. Forsans, and F. Santarelli (1994). Shale Testing and Capillary Phenomena. *31*(5), 411–427.

Sondergeld, C. H., R. J. Ambrose, C. S. Rai, and J. Moncrieff (2010). Micro- structural studies of gas shales: Presented at spe unconventional gas conference. SPE.

Sone, H. (2012). *Mechanical properties of shale gas reservoir rocks and its relation to the in-situ stress variation observed in shale gas reservoirs*. Phd, Standford University.

Sone, H. and M. D. Zoback (2013a, September). Mechanical properties of shale-gas reservoir rocks — Part 1: Static and dynamic elastic properties and anisotropy. *Geophysics 78*(5), D381–D392.

Sone, H. and M. D. Zoback (2013b, September). Mechanical properties of shale-gas reservoir rocks — Part 2: Ductile creep, brittle strength, and their relation to the elastic modulus. *Geophysics 78*(5), D393–D402.

Vermylen, J. P. (2011). *Geomechanical studies of the Barnett shale, Texas, USA*. Phd, Standford University.

Wood, D. M. (2004, April). *Geotechnical Modelling*. Abingdon, UK: Taylor & Francis.

BIBLIOGRAPHY

Xue, L., S. Qin, Q. Sun, Y. Wang, L. M. Lee, and W. Li (2014). A study on crack damage stress thresholds of different rock types based on uniaxial compression tests. *Rock Mechanics and Rock Engineering 47*(4), 1183–1195.

Yang, S.-q. (2012). Strength and deformation behavior of red sandstone under multi-stage triaxial compression. *Canadian Geotechnical Journal 49*(May), 694–709.

Youn, H. and F. Tonon (2010, June). Multi-stage triaxial test on brittle rock. *International Journal of Rock Mechanics and Mining Sciences 47*(4), 678–684.

Zahoor, M. (2014). Rock Behavior under High Pressure and High Temperature (HPHT). *SHALE ENERGY ENGINEERING 2014* (1975), 280–287.

Zoback, M. D. (2007). *Reservoir Geomehanics*. Cambridge, UK: Cambridge University Press.

Zoback, M. D. and J. D. Byerlee (1975). The effect of cyclic differential stress on dilatancy in westerly granite under uniaxial and triaxial conditions. *Journal of Geophysical Research* (80), 1526–1530.

Appendix A: Sample Characterization: Mineralogy

The shale samples to be used in this study were taken from three different locations at the Marcellus play:

(1) *Shallow Marcellus Shale, SMS, (400 ft. deep)*: From a well located at State Game Lands 252, Lycoming and Union counties, Allenwood, Pennsylvania. The rock plugs were drilled in 2008 by Penn State University. All cores are oriented perpendicular to the bedding (vertical samples).

(2) *Marcellus shale outcrop, MSO, (0 ft. deep)*: A set of six cores drilled from an outcrop block was used as an anisotropy set. The rock plugs were cored at 0^o, 90^o and 40^o to the bedding

(3) *Deep Marcellus Shale, DMS, (7,450 ft. deep)*: These cores were retrieved by the US Department of Energy in the late 1970's as part of its Eastern Gas Shale Program. The well is located in Monongalia County, West Virginia. All cores are oriented perpendicular to the bedding.

Mineralogy and petrological properties of these shales were studied via X-ray diffraction (XRD). In this section measurement profiles and quantitative analysis results (WPPF) are included for SMS, MSO, and DMS samples.

A.1 Shallow Marcellus Shale

In order to characterize the rock mineralogy from the State Game Land 252 (SGL) well, six shale samples were selected from different depths, so they were representative of the experiments conducted in this study (Single Stage, Multi Stage, Single Stage at high Temperature, Creep, Creep at high Temperature, Cyclic).

SGL-3 mineralogy analysis was conducted on coarse and fine fractions (separated by centrifugation). In addition, a composite-mineralogy quantification was estimated based on both fractions. On the other hand, although XRD analysis was conducted on SGL-39 sample, no quantitative analysis results are available for this sample.

Figures A.1-A.7 show measurement profiles for the six selected samples of SGL well, wheras Table A.1 summarizes the quantitative analysis results for these samples.

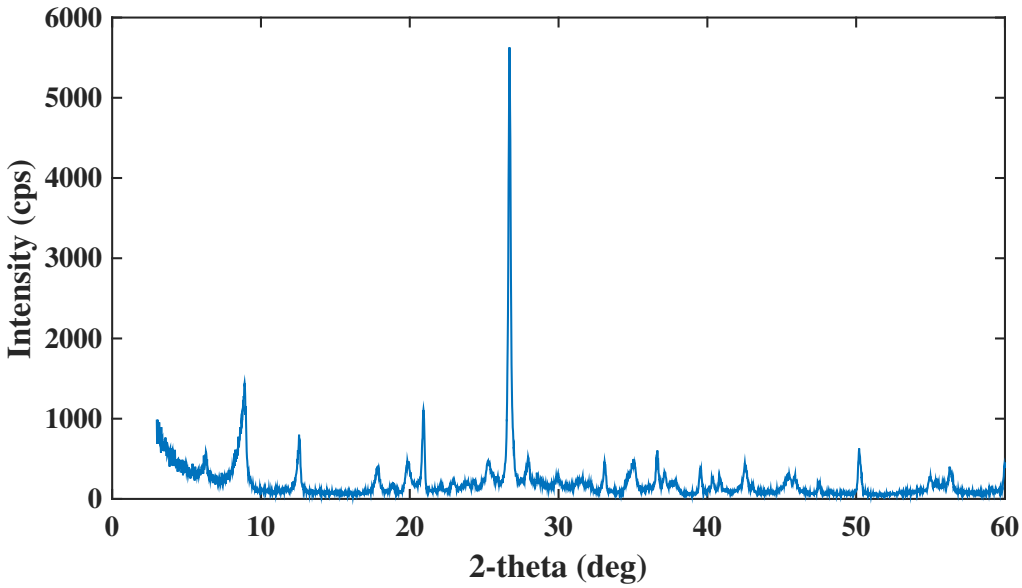

Figure A.1: **SGL-21 Mineralogy Measurement Profile (XRD).**

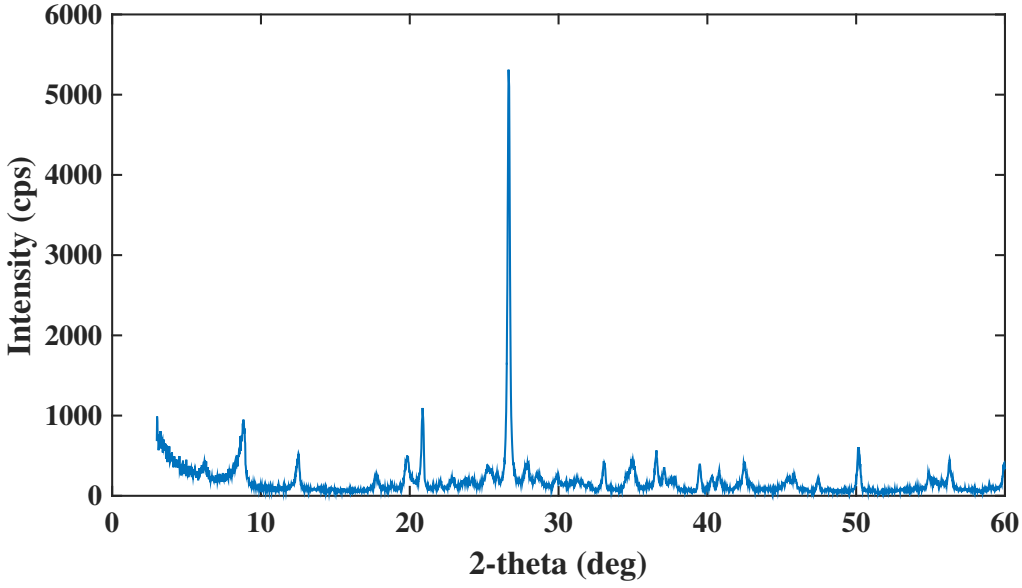

Figure A.2: **SGL-39 Mineralogy Measurement Profile (XRD).**

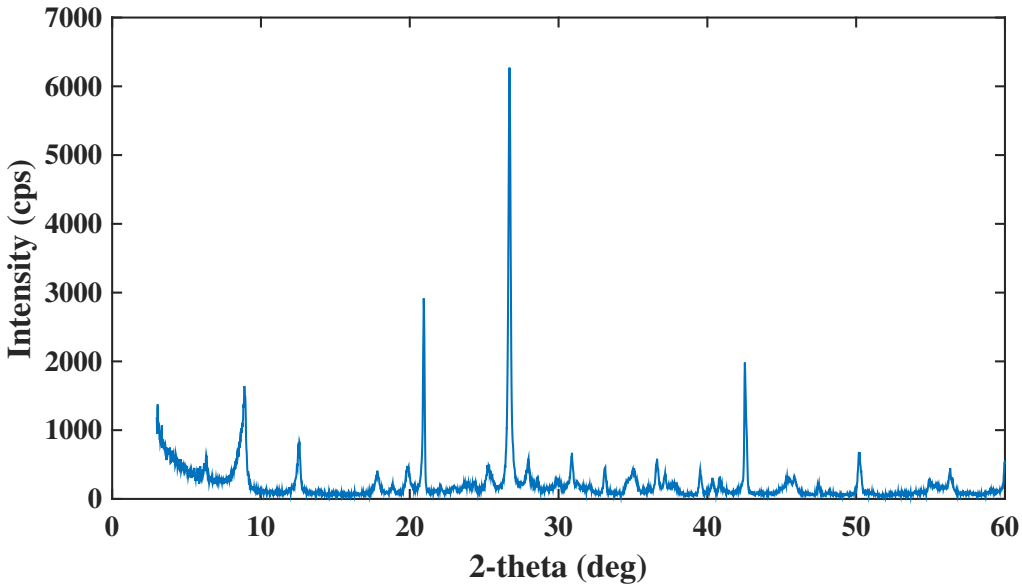

Figure A.3: **SGL-16 Mineralogy Measurement Profile (XRD).**

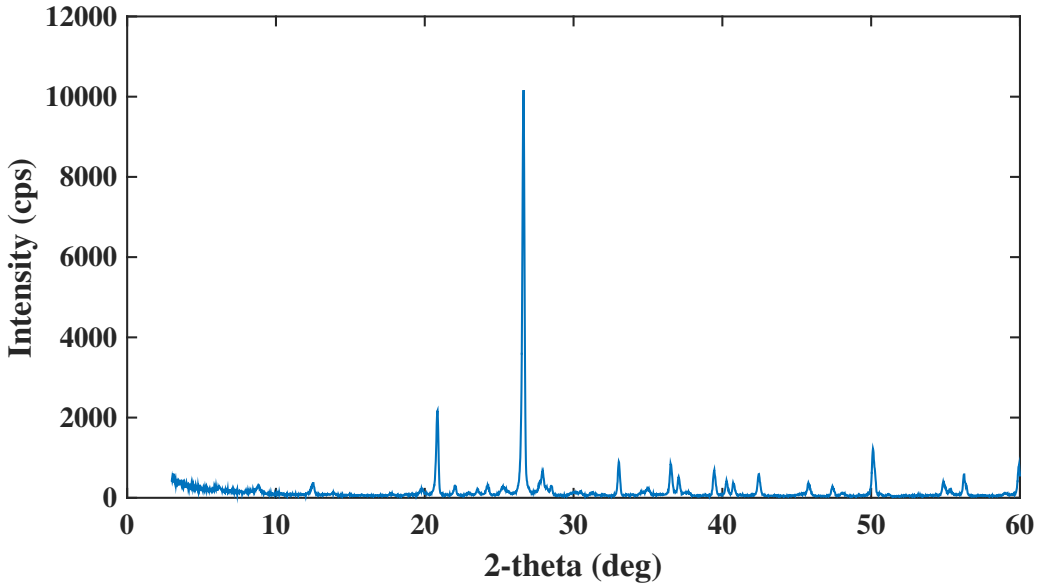

Figure A.4: **SGL-3 (coarse fraction) Mineralogy Measurement Profile (XRD).**

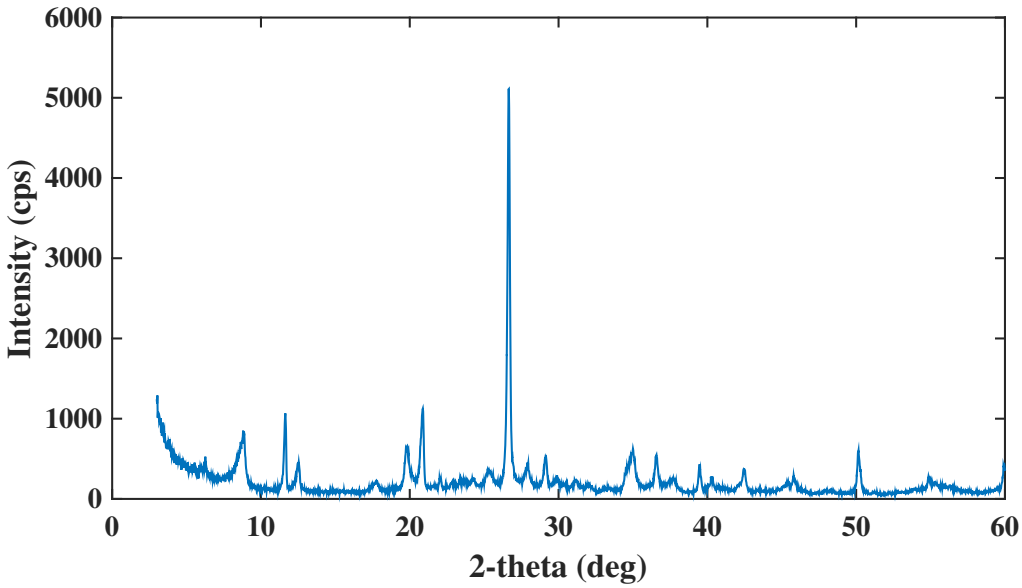

Figure A.5: **SGL-3 (fine fraction) Mineralogy Measurement Profile (XRD).**

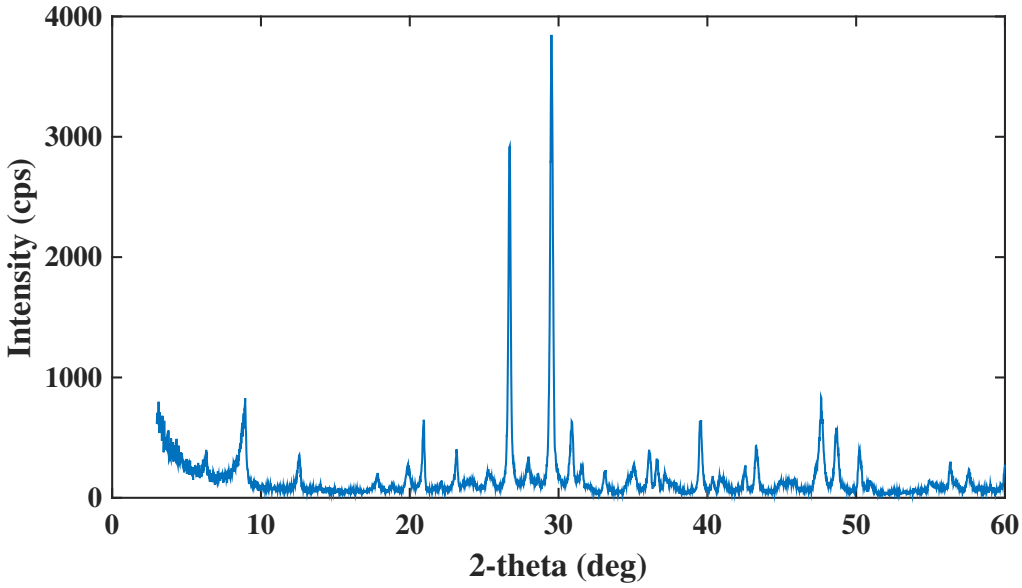

Figure A.6: **SGL-7 Mineralogy Measurement Profile (XRD).**

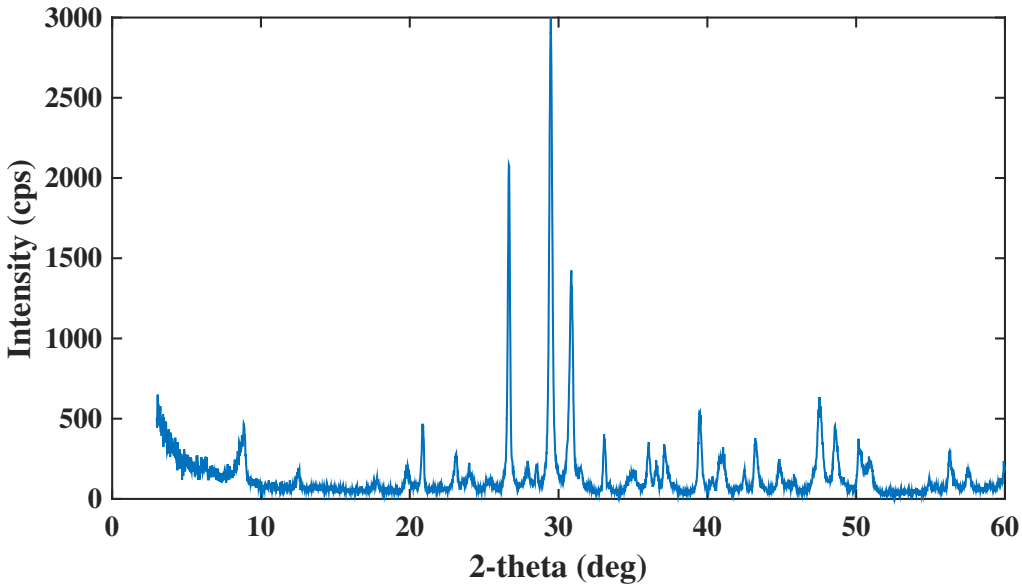

Figure A.7: **SGL-40 Mineralogy Measurement Profile (XRD).**

Table A.1: **Shalow Marcellus Shale Mineralogy Quantitative Analysis (WPPF). Due to an error during quantification, no results are available for SGL-39 sample.**

ID	Depth	ρ	Mineralogy										
	(ft)	(g/cc)	*Clay*					*Tectosilicate*			*Carbonate*		
			Muscovite	Illite	Kaolinite	Chlorite	Mont.	Quartz	Feldespar	Pyrite	Dolomite	Calcite	Gypsum
SGL-21	327	2.59	26.4	-	-	27.3	-	37.5	5.2	3.60	-	-	-
SGL-39	355	2.62	nqa	nqa	nqa	nqa	nqa	nqa	nqa	nqa	nqa	nqa	nqa
SGL-16	370	2.59	52.4	-	7.5	5.1	-	22.30	3.5	1.7	5.5	2.2	-
SGL-3	405		-	54.0	4.4	-	4.0	20.2	2.1	0.9	-	-	-
SGL-7	428	2.54	45.7	-	4.6	3.8	-	13.7	-	0.8	8.5	22.9	-
SGL-40	436	2.72	31.0	-		3.0	-	9.9	-	2.3	29.4	24.40	-

A.2 Marcellus Shale Outcrop

Figure A.8 and Table A.2 present the measurement profile and quantitative analysis for the Marcellus outcrop block.

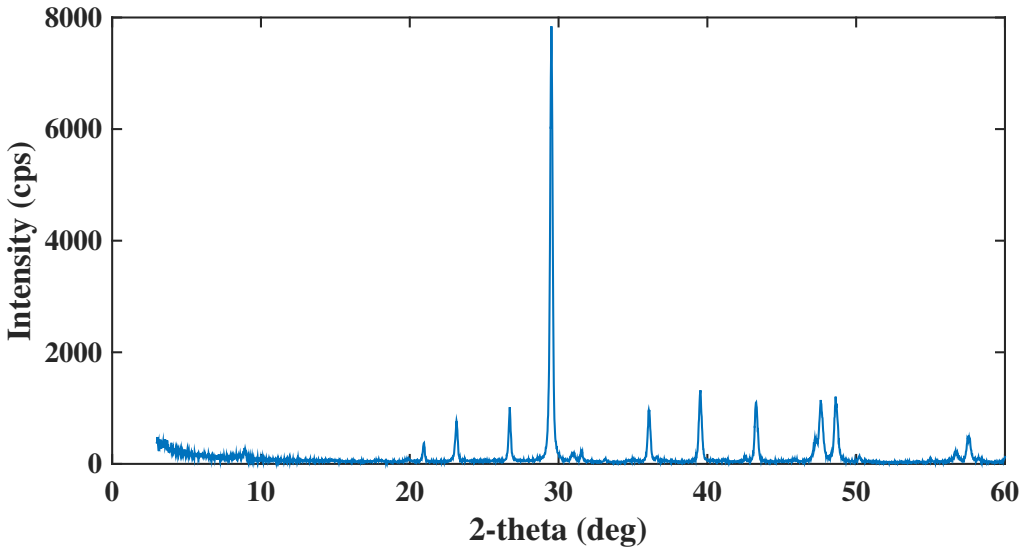

Figure A.8: **MSO Mineralogy Measurement Profile (XRD).**

Table A.2: **Marcellus Shale Outcrop Mineralogy Quantitative Analysis (WPPF).**

ID	Depth	ρ	Mineralogy										
	(ft)	(g/cc)	*Clay*					*Tectosilicate*			*Carbonate*		
			Muscovite	Illite	Kaolinite	Chlorite	Mont.	Quartz	Feldespar	Pyrite	Dolomite	Calcite	Gypsum
MSO	0	2.58	7.0	-	-	-	-	10.0	-	-	3	79.1	-

A.3 Deep Marcellus Shale

Figure A.9 and Table A.3 present the measurement profile and quantitative analysis for the Deep Marcellus Shale.

Table A.3: **Deep Marcellus Shale Mineralogy Quantitative Analysis (WPPF).**

ID	Depth	ρ	Mineralogy										
	(ft)	(g/cc)	*Clay*					*Tectosilicate*			*Carbonate*		
			Muscovite	Illite	Kaolinite	Chlorite	Mont.	Quartz	Feldespar	Pyrite	Dolomite	Calcite	Gypsum
DMS	7,500	2.58*	-	69.0	-	-	-	20.8	-	3.1	-	2.9	4.1

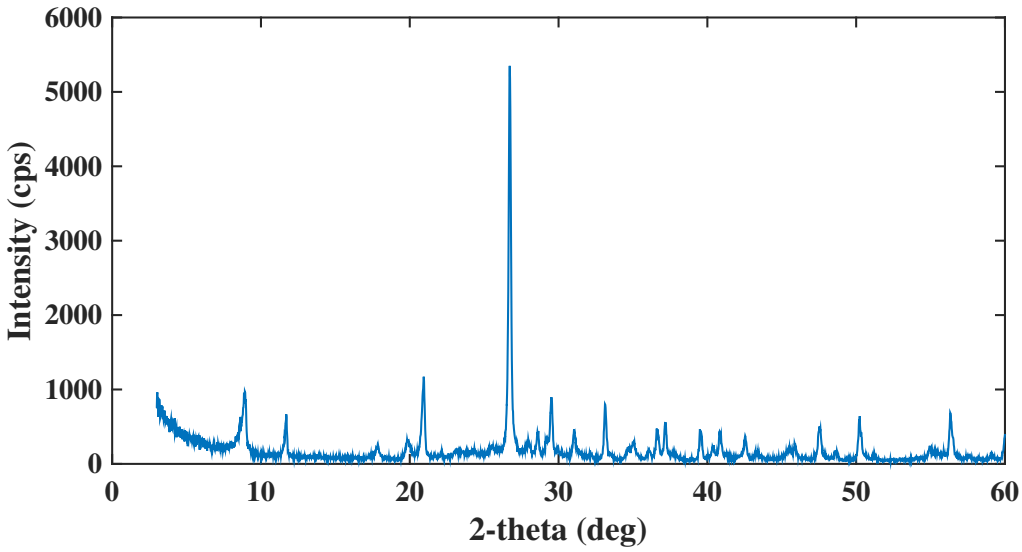

Figure A.9: **DMS Mineralogy Measurement Profile (XRD).**

A.4 Comparison

With the objective to provide comparability across the samples we have grouped minerals into three major categories: clays (muscovite, illite, kaolinite, chlorite, montmorillonite), tectosilicates (quartz, feldespar, pyrite, dolomite), and carbonates (dolomite, calcite) + gypsum. Figure A.10 and Table A.4 show mineralogy results for all samples (SMS, MSO, DMS) using such ternary system.

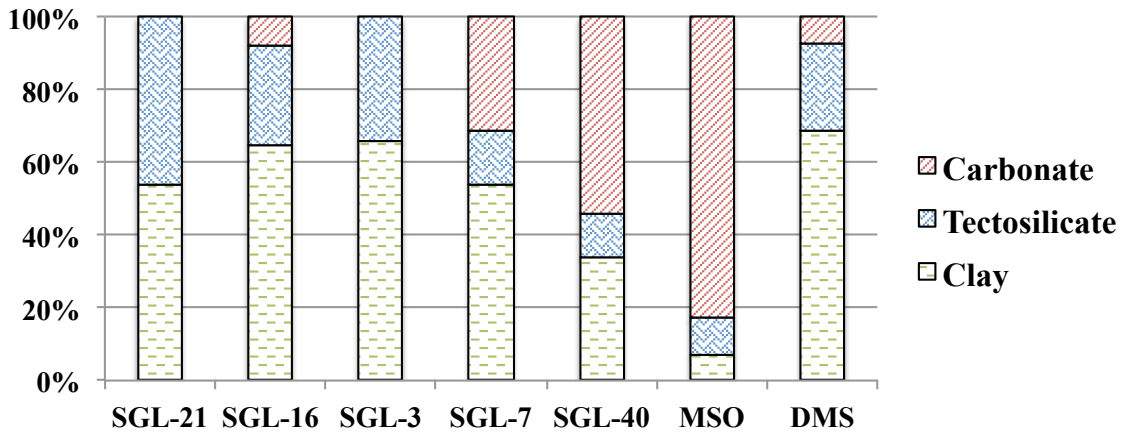

Figure A.10: **Mineralogy Comparison (ternary system).**

Table A.4: **Mineralogy Comparison (ternary system).**

Core ID	Exp. ID	Depth (ft) (ft)	ρ (g/cc)	Mineralogy (%)		
				Tectosilicate	Carbonate	Clay
SGL-21	SS35	327	2.59	46.3	0.0	53.7
SGL-39	SS25	355	2.62	-	-	-
SGL-16	CR35-65	370	2.59	27.4	7.7	64.9
SGL-3	Preliminar Anal.	405	2.57	34.1	0.0	65.9
SGL-7	CR-T	428	2.54	14.5	31.4	54.1
SGL-40	DS	436	2.72	12.2	53.8	34.0
MSO	MSO	0	2.58	10.1	82.8	7.1
DMS	DMS	7,500	2.58*	23.9	7.0	69.1

Appendix B: Geomechanical Testing of Rocks at High Pressure Conditions

B.1 Details of the Triaxial Apparatus and Experimental Setup

The triaxial apparatus described here is an AutoLab 1500_70 built by New England Research (Figure B.1). This is a fully servo-controlled triaxial machine designed to perform standard coupled process petrophysical and rock mechanics experiments at reservoir conditions of overburden pressure, pore pressure, and temperature on specimens up to 50 mm (2.0 in) in diameter. Unlike many other triaxial systems, a load frame does not generate the force parallel to the core axis. Instead, a movable piston divides the pressure vessel into two chambers where pressure is generated independently by high-pressure servo-hydraulic intensifiers. Isotropic confining pressure is applied to the sample in the lower chamber by

the confining fluid, while differential stress is exerted on the specimen by the generation of a differential pressure between both upper and lower chambers (NER).

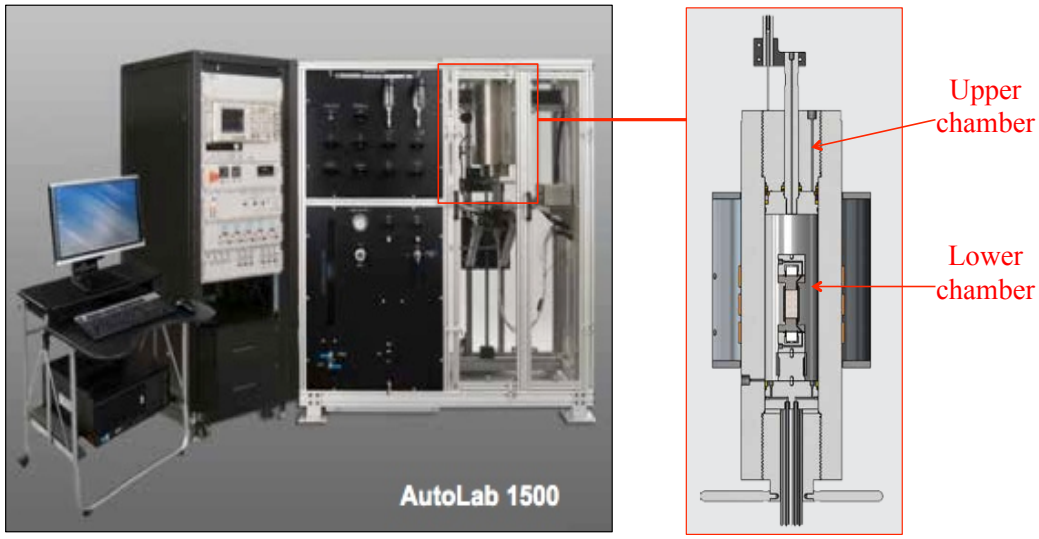

Figure B.1: **Photograph of the AutoLab 1500 triaxial apparatus (left) and schematic of the pressure vessel (right). Source: Modified from NER.**

The AutoLab 1500_70 model can generate up to 70 MPa (10,000 psi) of confining pressure and pore pressure. Axial force at rated confining pressure is 175,000 lbs, while maximum axial force at unconfined experiments is 315,000 lbs.

During the experiments, deformation can be measured using LVDTs or strain gauges. Pore pressure intensifiers are also compatible with water, brine, oil and gas (including CO2), which allow us to perform multiple useful experiments for the energy field. Depending on the required measurement, different coreholders and electronic and software modules

are necessary to control the sequencing, acquisition, and processing of the data. The coreholders available for the system are the following:

(1) *PS2 Ultrasonic Transducer*: These coreholders allow for the measurement of P-wave and cross-polarized S-wave velocities at different pressures and temperature conditions.

(2) *Steady State Permeability*: This method is designed for permeabilities between 0.1 and 500 nD. Two pore pressure intensifiers control a constant pore pressure gradient across the sample. Then, flow rate can be used to compute permeability.

(3) *Transient Permeability:* : This technique also measures permeabilities between 0.1 and 500 mD. A small pore pressure perturbation (0.4 MPa or 50 psi), or pulse, is generated at the upstream side of the sample, and the pore pressure response at the downstream side is monitored. Permeability is then computed by fitting the data to analytic solutions. This short duration method (10 seconds) enables measurement of permeability at in situ conditions.

(4) *Low Permeability*: Materials with permeabilities in the range of 5 nD to 50 μD require the use of this special coreholder, which utilizes the transient method for permeability analysis.

(5) *Complex Electrical Impedance*: IResistivity can be measured using this coreholder. It uses both two and true four electrode techniques (frequencies between 0.02 Hz and 100 kHz).

B.2 Sample Preparation

Sample preparation starts with drilling core plugs from the original cores. While doing this, one needs to be consistent with respect to drilling direction, since rock properties often are anisotropic. In shales, special attention must be paid when drilling normal to the bedding since weak planes may be present. Applying a small axial load inside the coring bit may be helpful. It is also recommended to avoid sampling the outer centimeter of the core, due to potential alteration. If a drilling fluid is used, it should be chemically compatible with the rock. In this sense, it is especially important to use an inert fluid (e.g. mineral oil) for shale samples, since contact with water may induce large capillary effects that may change the structure and properties of the shale.

International standards require that samples are right, circular cylinders with a length to diameter ratio between 2 and 3, facilitating the occurrence of the failure plane through the side walls so no additional support is provided. End surfaces should be flat within ± 0.01 mm (Figure B.2), the sides smooth and straight, and the parallelism better than $\Delta L/L = 0.001$.

Then, several measurements must be recorded including the sample length to the nearest 1.0 mm, the diameter to the nearest 0.1 mm, and the mass to the nearest 0.01g. (Figure B.3). Additionally, water content should always be estimated before the mechanical test.

The next step involves installation of a copper sleeve. The sleeve sheet must be cut so it covers the side walls. A piece of paper can be used as a template as shown in Figure B.4.

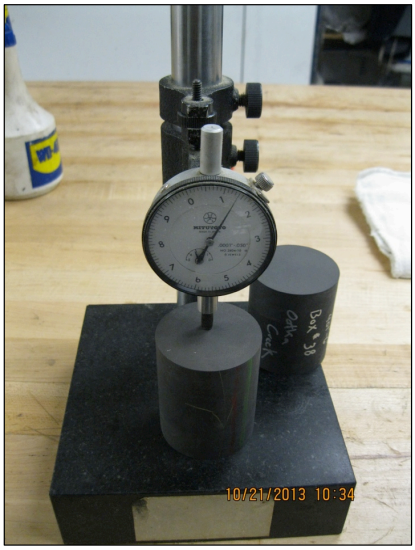

Figure B.2: **International standards require that end surfaces should be flat within $\pm$0.01 mm. This can be checked using a flatness gauges (as shown here).**

Once the copper sleeve is cut to an appropriate size, it is wrapped around the sample and the free ends are soldered together. Rubber bands can be used to assist with soldering (Figure B.5).

After the soldering is completed, the sample must be placed into a confining vessel (Figure B.6)) in order to seal the sleeve to the rock. For this, a heat-shrink Viton jacket can be used to seal the sample from the confining fluid. Steel cylinders are also needed at the opened ends to avoid damaging the sample.

Last step of sleeve installation consists in filing the excess solder from the joint to create a smooth surface. It is also important to sand the copper sleeve where strain gauges are to be attached (Figure B.7)).

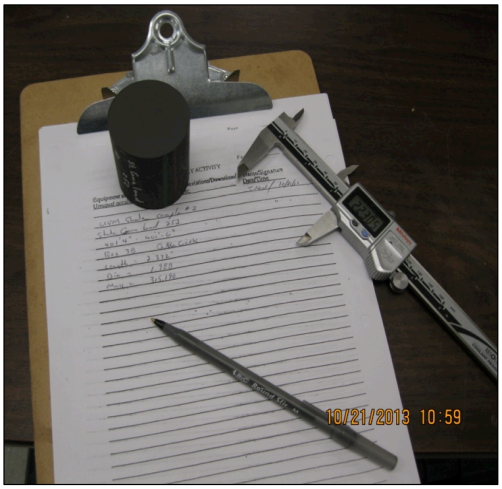

Figure B.3: **Calibers can be used for measuring diameter and length prior to the experiment. Diameter can be measured by averaging two perpendicular measurement.**

Finally, axial and radial strain gauges are epoxied to the sanded copper sleeve (Figure B.8)). While the epoxy dries (which may take several hours), it is recommended to wrap the sample using parafilm, a Viton jacket, and rubber bands to securely seal the gauges to the sleeve.

B.3 Experiment Setup

After sample preparation is completed, the next step is to couple the sample to the coreholder. First, the coaxial ports must be soldered to the strain gauges. In order to seal the joint between the specimen and the coreholder, a Viton jacket and two wires can

Figure B.4: **The sleeve separates the sample from the confining fluid. It is cut from a copper sheet, and should be large enough to cover completely the side walls.**

be used for each side (Figure B.9). It is important to note the alignment of coreholder since some transducers, such as pore pressure transducers, have to be placed face to face. Once the coupling is complete, it is necessary to measure the column height to check if it fits into the confining vessel.

If acoustic measurements are to be made, a thin layer of grease gel or another viscous fluid is needed (Figure B.10). This ultrasonic couplant facilitates the transmissivity of waves across the interface. Acoustic signals are extremely sensitive to the coupling between the transducers and the specimen. It is important that the couplant layer is thin enough not to contribute significantly to the measured transit time. When coupling shear wave transducers, one has to make sure that the transmitting and receiving transducers are placed face to face (i.e. polarization points in the same direction). It is good practice to

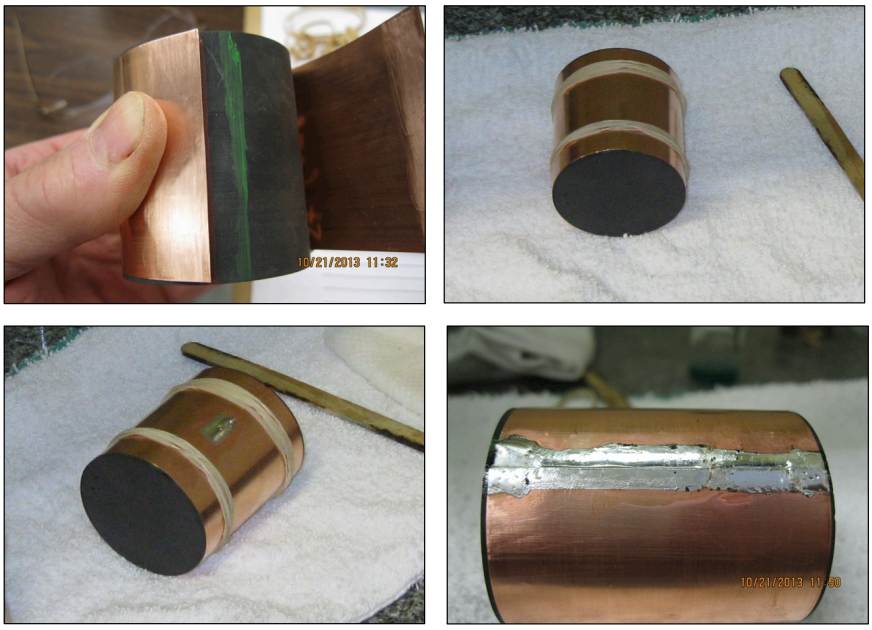

Figure B.5: **Two rubber bands can be placed at the top and the bottom of the sample in order to maintain joined end sides during soldering. The easiest way is to start from the center of the joint line and move towards one end while maintaining one rubber band at the opposite side.**

mark bedding direction on the sample surface before preparation to assist with transducer placement; bedding direction often controls the anisotropy of the rock properties.

The last step involves connecting the sensors and verifying that they work. Verification is done by monitoring the sensor signal via the electronic controller. After verification, the column can be placed into the confining vessel. After screwing it to the top, one should release a small amount of pressure by unscrewing it $1/2$ turn.

Finally, strain gauges and load cell calibration have to be performed according to the manufacturer.

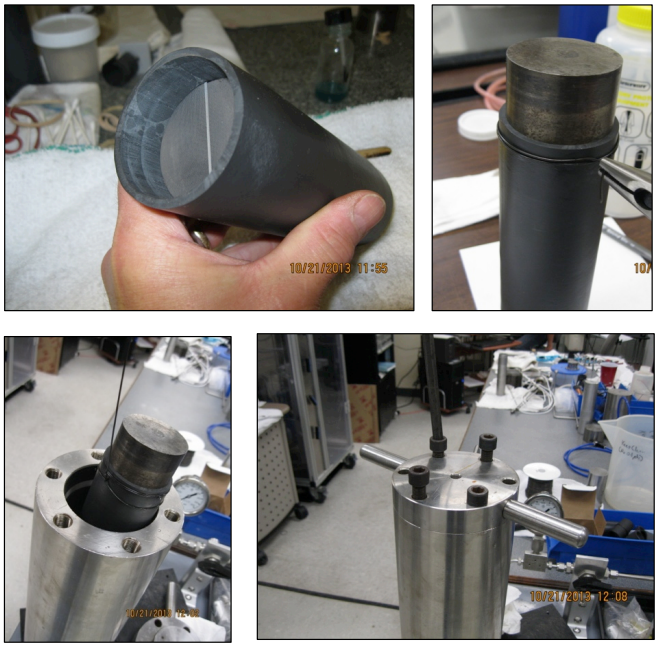

Figure B.6: **Sealing the sleeve to the rock is an important step, so it deforms jointly with the rock. The sample has to be completely isolated from the confining fluid during this process. If a separated confining vessel (bottom pictures) is not available, the confining vessel of the triaxial apparatus can be used instead.**

APPENDIX B. GEOMECHANICAL TESTING OF ROCKS AT HIGH PRESSURE CONDITIONS

Figure B.7: **Prior to the strain gauges installation, the excess of solder should be filed. The side wall where gauges are to be glued, should be sanded as well.**

Figure B.8: **The last step involves the installation of strain gauges. Prior to epoxying the gauges, the surface should be cleaned with acetone. While the epoxy dries, it is recommended to wrap the sample using parafilm, a Viton jacket, and rubber bands, so the gauges are completely sealed to the sleeve.**

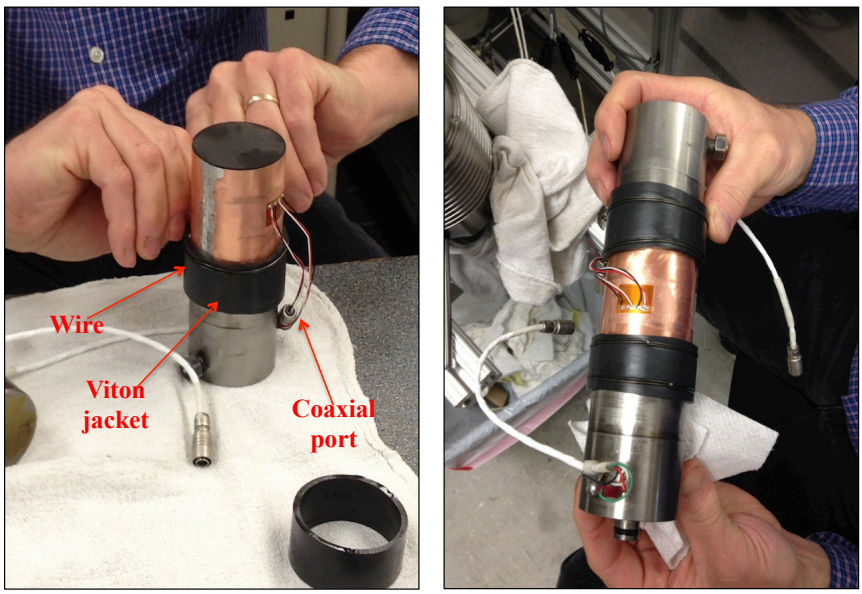

Figure B.9: **A Viton jacket and two wires can be used for sealing the joint between the sample and the coreholder. During coupling process, special attention has to be paid to the alignment of transducers.**

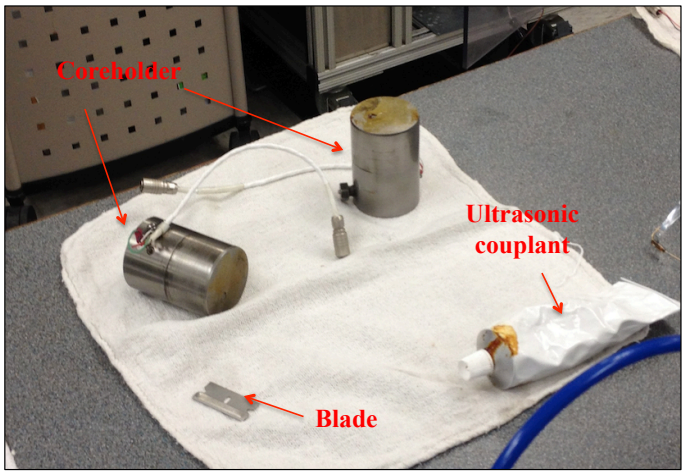

Figure B.10: **A small blade can be used in order to spread the ultrasonic couplant onto the acoustic coreholder. This layer should be homogeneous and as thinnest as possible.**

Appendix C: Ductile Behavior

C.1 Introduction

The loss of productive fracture area and fracture conductivity in shale formations has a major economic impact on gas production (Ghassemi 2012). As gas is initially produced, pore pressure is drawn down resulting in an increase in the effective pressure that eventually leads to the closure of fractures and microfractures resulting in a reduction of permeability on multiple scales (Vermylen 2011, Ghassemi 2012). Moreover, creep deformation also affects the transport properties in the long term as well as the regional stress state that has a major impact in hydraulic fracturing success. Therefore, understanding the causes and the rate of decline of production/permeability is a key factor in the management and operational design of shale gas reservoirs.

The viscoelastic-plastic behavior of these formations has been investigated to a limited extent (Ghassemi 2012, Sone 2013a). Creep strain was correlated with Young's modulus, and clay and organic content of the shale sample. Results from these studies showed that creep behavior can be described using a power-law strain-time model during both

hydrostatic and triaxial stage as:

$$\epsilon^c = k\sigma t^n \tag{C.1}$$

Where ϵ^c is the time-dependent component of the creep only. Nevertheless, during triaxial stage creep behavior is better described by a mechanical system known as Burgers model (Findley et al., 1976), which response can be modeled as:

$$\epsilon = \frac{\sigma}{E_1} + \frac{\sigma}{\eta_1}t + \frac{\sigma}{E_2}\left(1 - e^{-\frac{E_2}{\eta_2}t}\right) \tag{C.2}$$

This system is composed of a series of springs (E_1,E_2) and dashpots (η_1, η_2), which are able to reproduce the elastic and viscous response of creep. Both studies also observed that creep strain is smaller in the radial direction indicating a volume loss, most likely accommodated by microcrack and pore closure (Ghassemi 2012, Sone 2013a).

C.2 Methods

This experiment was designed to study the effect of both pressure and temperature on the creep behavior of shale rocks. Five tests were performed at three different confinement levels (5, 35 and 60 MPa) and different temperatures (30 ^{o}C, 60 ^{o}C, and 120 ^{o}C) following the same stress path shown in Figure C.1. During the hydrostatic stage, confining pressure, CP, was applied following a multistep-wise loading increments of 5 MPa at a constant rate of 0.333 MPa/sec, and then held for an hour to ensure uniform consolidation at each step. After the target confining pressure was reached, deviatoric stress, DS, was applied in 4 stages. For each stage, pressure was increased at a rate of 0.333 MPa/sec, then it was held

constant for 12 hours to observe the creep response. In addition, during the first loading in each step the DS was partially decreased and increased again when it reaches the mid point for the loading step in order to measure the unloading/reloading constants. At the end of each test, DS was removed to observe how much viscoelastic deformation is recovered. Details and experiment objectives are summarized in Table C.1.

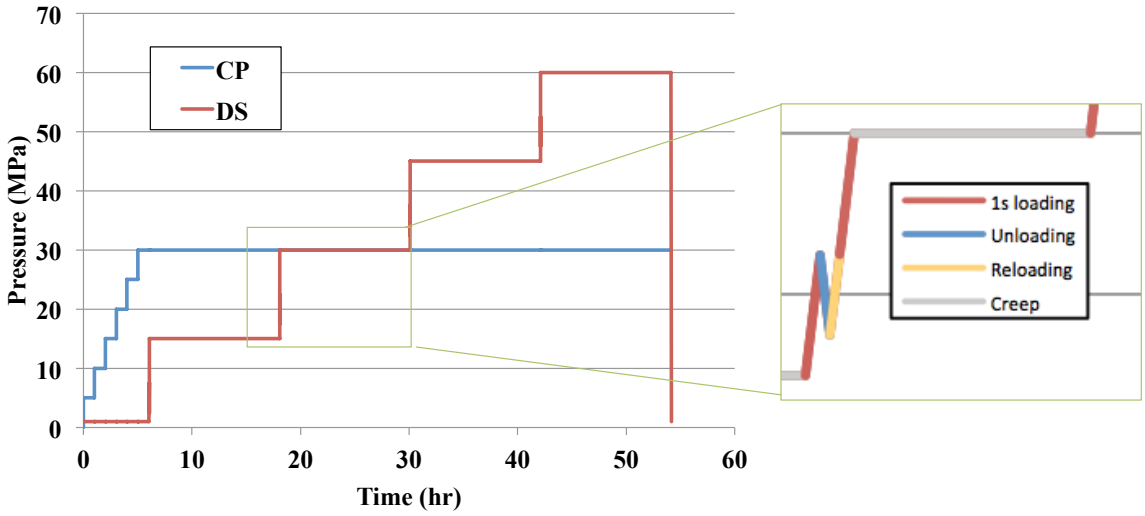

Figure C.1: **Ductile creep test with four stages (σ_3 = 30 MPa).**

Table C.1: **Ductile Creep Experiment Summary**

CP (MPa)	5, 35, 65 (T = 30 ^{o}C)
T (^{o}C)	30, 60, 120 (CP = 35 MPa)
Experimental parameters	Axial and Radial strains, stress
Experimental outcome	Creep behavior, Elastic moduli (E, ν, G, K), Pressure dependence

C.3 Results

C.3.1 Sample Variability

Figure C.2 compares the mineralogy of the samples used in this experiment with the composition of Single Stage tests samples. While mineralogy is very similar between SS and CR samples, CR-T samples present a higher carbonates content. This higher carbonate (and lower clay) content seems to have an important effect on specimen stiffness as it can be seen in Figure C.3.

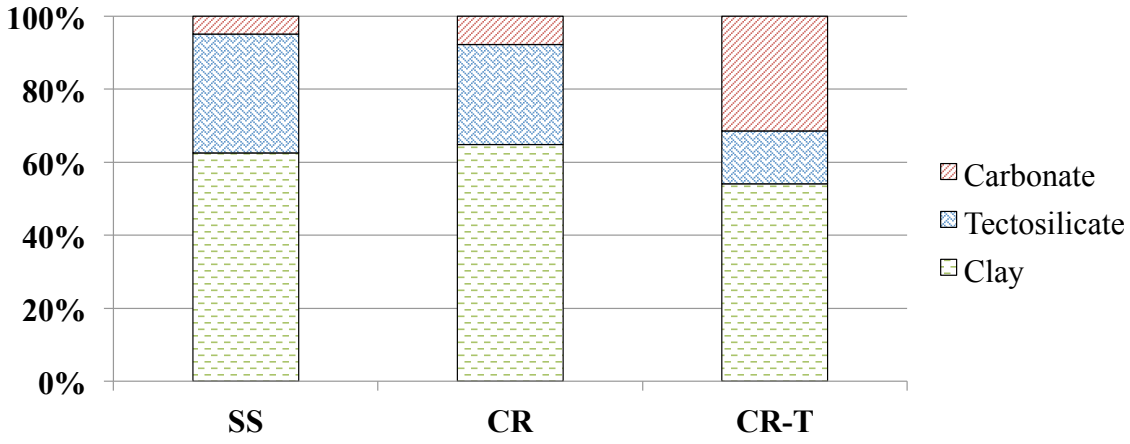

Figure C.2: **Comparison of mineralogy. SS = Single Stage tests, CR = Ductile Creep tests (T = 30 ^{o}C), CR-T = Ductile Creep tests at high Temperature (T = 60, 120 ^{o}C).**

C.3.2 Static Parameters

Figures C.4, C.6 and C.8 show the strain response of Marcellus shale during the Triaxial Stage of Ductile Creep tests. Static Youngs'a moduli were estimated upon 1st-loading,

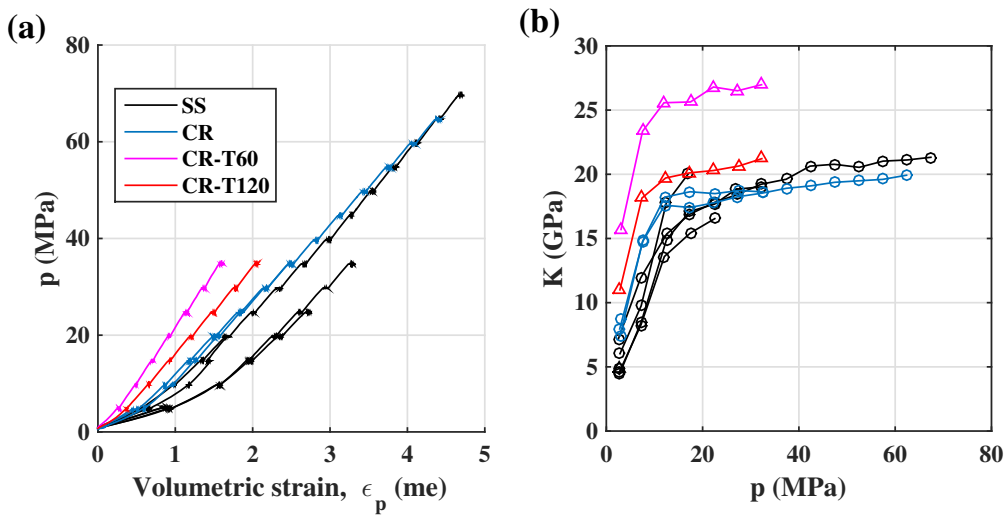

Figure C.3: **Comparison of mechanical behavior between Single Stage (SS) and Ductile Creep (CR, CR-T) tests during Hydrostatic Stage.**

unloading and reloading (Figures C.5, C.7 and C.9). Note the zig-zag trend for E_{1st} as a consequence of creep stages. This feature was not observed during SS tests. Small pressure dependence is observed in these tests.

C.3.3 Ductile Creep

Figures C.10, C.11 and C.13 present the 12-hour creep at different deviatoric stress steps for the three confining pressure levels. Figure C.13 compares the axial strain after the 12-hour creep for all experiments.

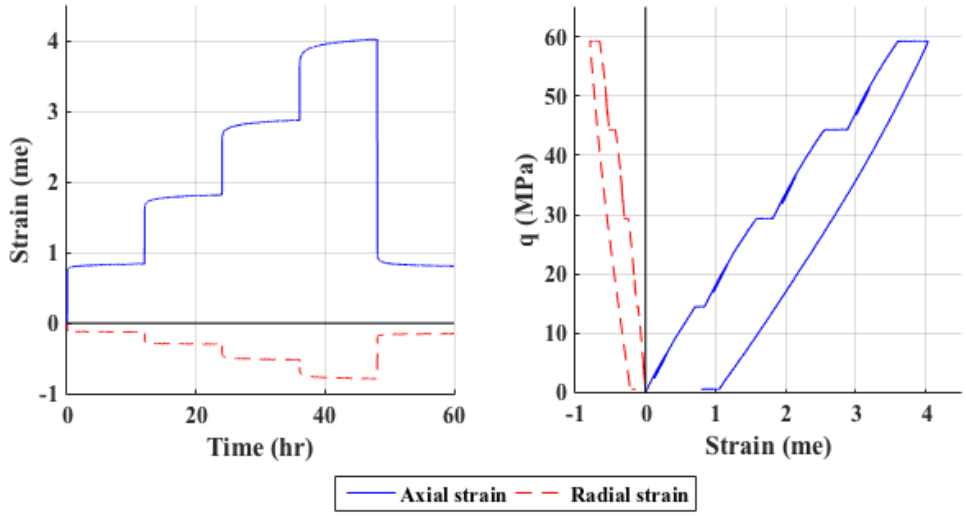

Figure C.4: **Ductile Creep test at CP = 5 MPa. Triaxial Stage**

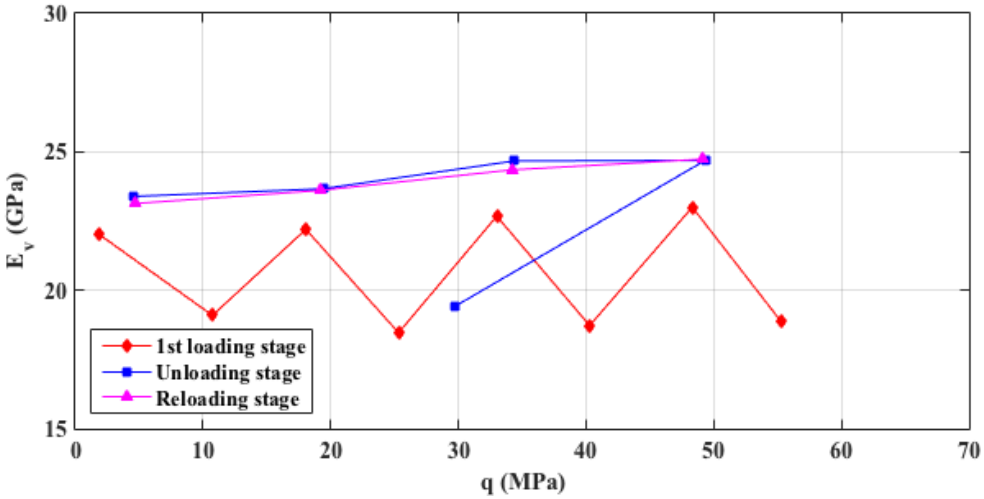

Figure C.5: **Ductile Creep test at CP = 5 MPa. Static Young's moduli**

C.3.4 Intact Strength

Figure C.14 compares the mechanical behavior between Single Stage and Ductile Creep tests upon monotonic loading. We believe that both the small length-diameter ratio, and

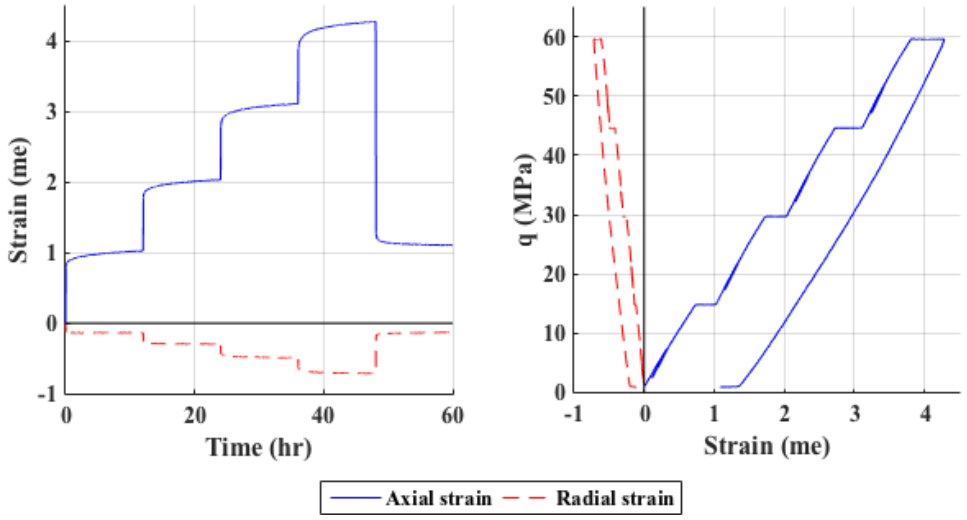

Figure C.6: **Ductile Creep test at CP = 35 MPa. Triaxial Stage**

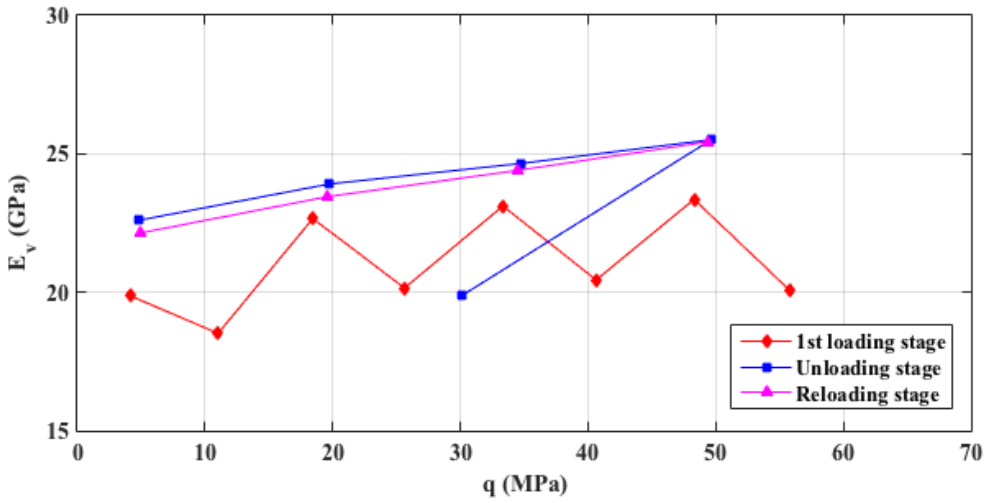

Figure C.7: **Ductile Creep test at CP = 35 MPa. Static Young's moduli**

sample variability, seem to have an important effect on intact strength. Note the impact of loading history on mechanical behavior for deviatoric levels below 60 MPa.

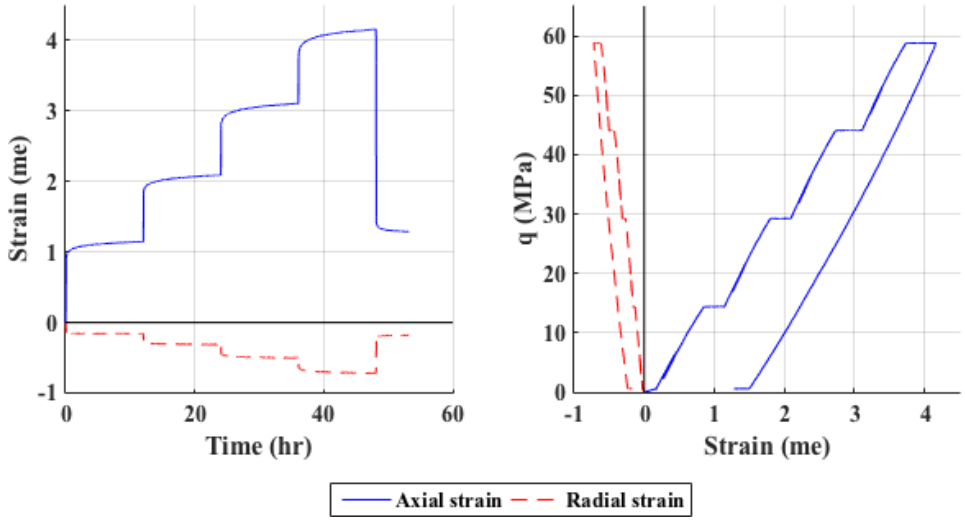

Figure C.8: **Ductile Creep test at CP = 65 MPa. Triaxial Stage**

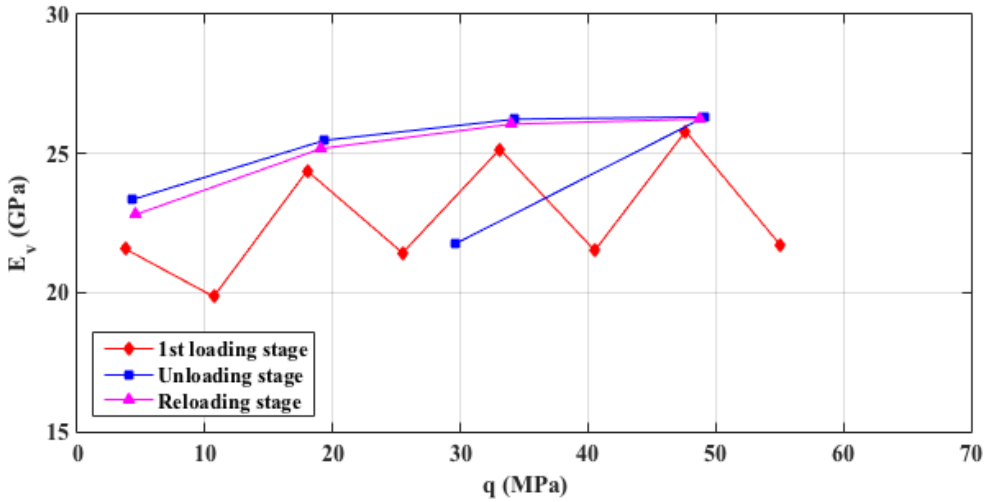

Figure C.9: **Ductile Creep test at CP = 65 MPa. Static Young's moduli**

C.3.5 High Temperature Tests

Finally, Figures C.15, C.16 and C.17 explore the impact of temperature on creep response. Because of the high sample variability, it is very difficult to derive any conclusion from

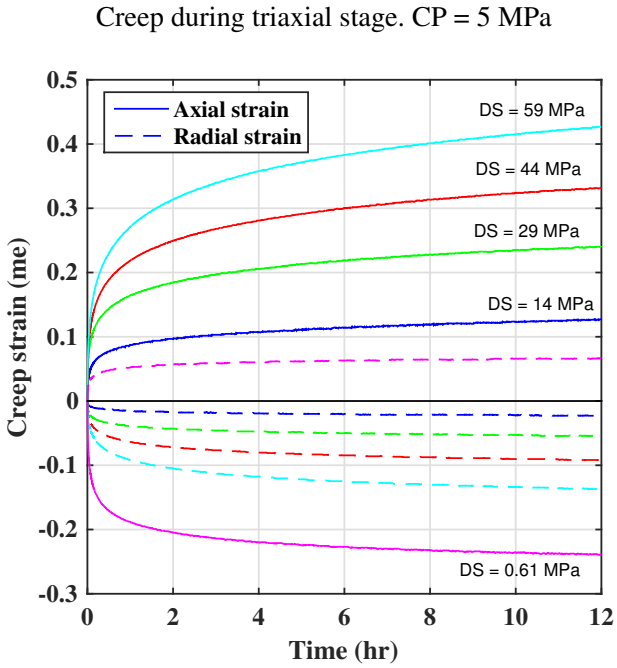

Figure C.10: **Ductile Creep test at CP = 5 MPa. Time-delay behavior**

this experiment. However, if we compared CR-T60 with CR-T120 we can observe a considerable impact of temperature. Whereas CR-T60 seems to be stiffer than CR-T120 upon hydrostatic loading (Figure C.3), the latter shows a much more softer mechanical behavior after thermal loading.

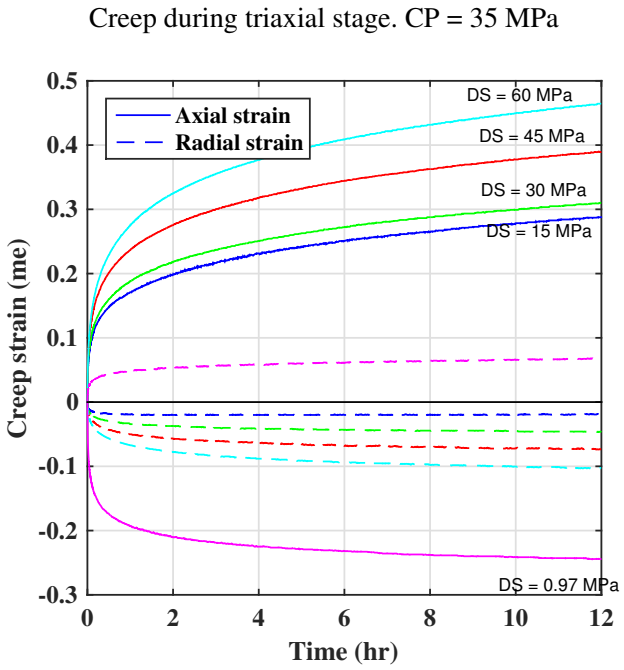

Figure C.11: **Ductile Creep test at CP = 35 MPa. Time-delay behavior**

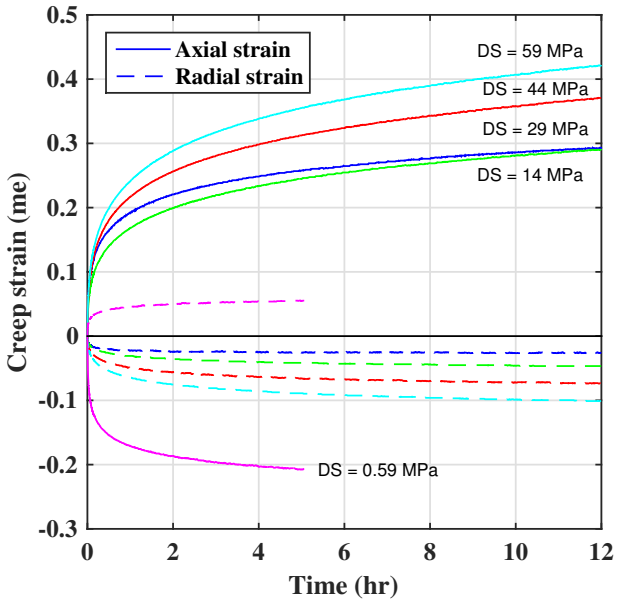

Figure C.12: **Ductile Creep test at CP = 65 MPa. Time-delay behavior**

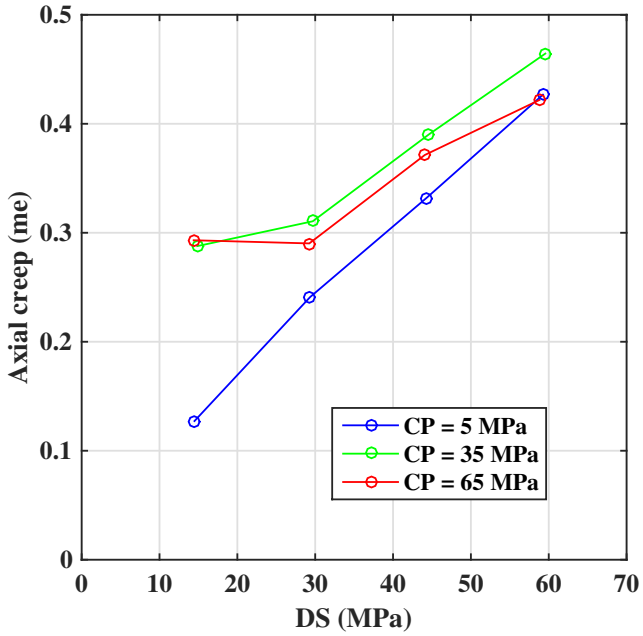

Figure C.13: **Triaxial 12-hour creep for 4 DS steps at different confining levels.**

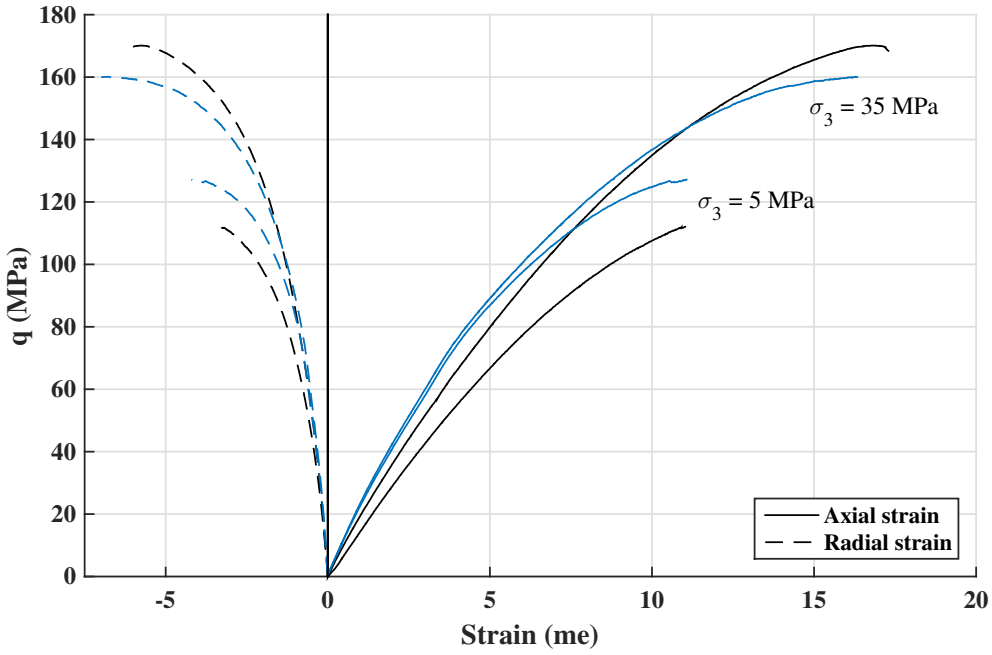

Figure C.14: **Comparison of mechanical behavior between Single Stage (black lines) and Ductile Creep (blue lines) tests during monotonic loading.**

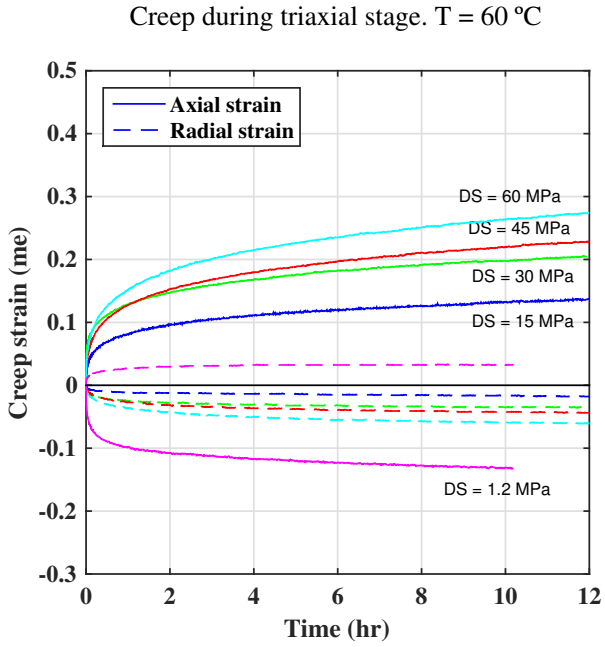

Figure C.15: **Ductile Creep test at T = 60 ^{o}C. Time-delay behavior**

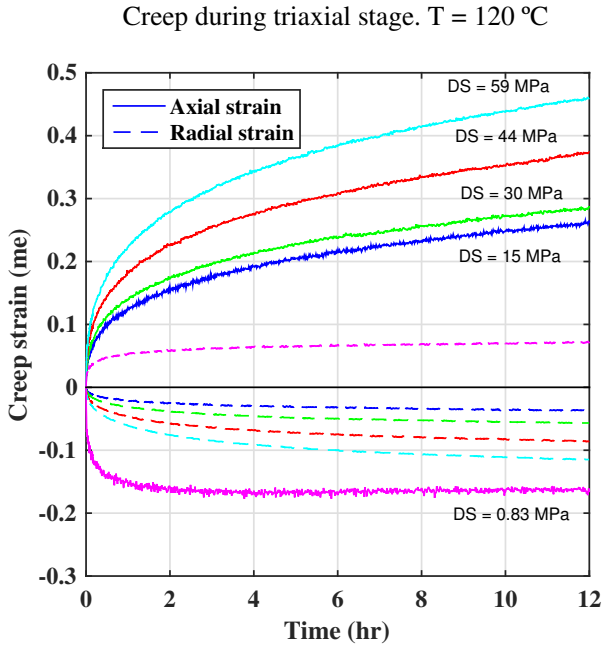

Figure C.16: **Ductile Creep test at T = 120 ^{o}C. Time-delay behavior**

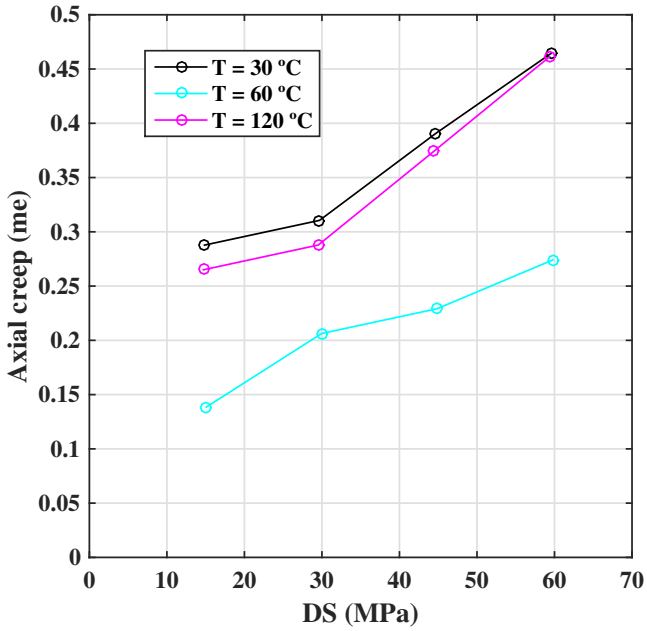

Figure C.17: **Triaxial 12-hour creep for 4 DS steps at different temperature conditions.**

Appendix D: Dense Shale

D.1 Introduction

During our experiments, we found some rock plugs with an unusual high bulk density (2.75 g/cc). XRD analysis revealed high carbonate content (Figure D.1).

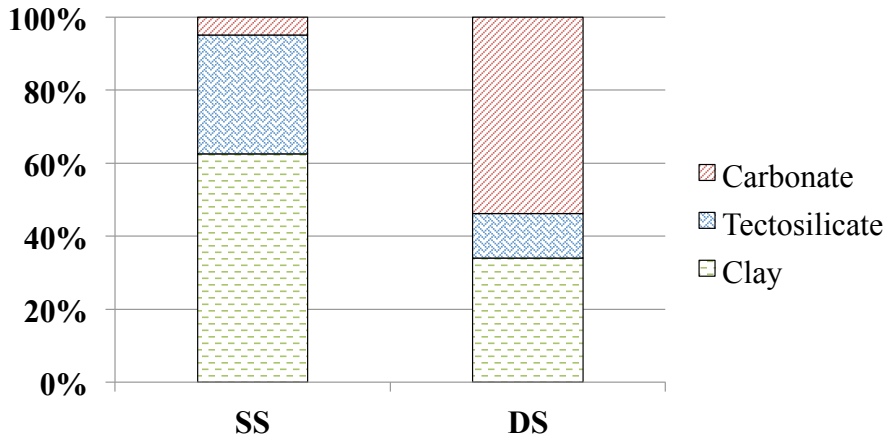

Figure D.1: **Comparison of mineralogy. SS = Single Stage tests, DS = Dense Shale.**

D.2 Methods

In order to characterize the mechanical properties of these dense shale (DS) samples, one Elastic Multi-Stage (DS-MSE) test and two Singe Stage (DS-SS) tests were conducted. The DS-SS test were performed as described in section 3.2.3, at two different confining pressures (5 and 15 MPa). On the other hand, the DS-MSE test consisted of 9 stages following the same stress path shown in section 3.2.3.

D.3 Results

A summary of the test specimens for Dense Shale, along with the elastic and strength parameters results are presented in Tables D.1 and D.2.

Table D.1: **Dense Shale SS triaxial tests results: Elastic moduli. Static moduli are estimated from initial slope.**

Test ID	**Core**			**Test Conditions**		**Elastic Moduli**				
	Ratio L:D	ρ (g/cc)	Depth (ft)	σ_3 (MPa)	T (^{o})	E_v (GPa)	ν_{vh}	K (GPa)	G (GPa)	J (GPa)
DS-SS05	1.8	2.7	436	5	30	59.7	0.23	32.2	21.6	198
DS-SS15	1.8	2.8	436	15	30	69.9	0.28	59.3	27.1	2,200

Table D.2: **Dense Shale SS triaxial tests results: Strength parameters.**

Test ID	**Test Conditions**		**Strength**				
	σ_3 (MPa)	T (^{o})	σ_{1d} (MPa)	σ_{1f} (MPa)	σ_{1u} (MPa)	ϵ_{af} (me)	ϵ_{rf} (me)
DS-SS05	5	30	184.5	186.1	185.5	3.69	-1.11
DS-SS15	15	30	249.3	249.7	248.2	3.85	-3.3

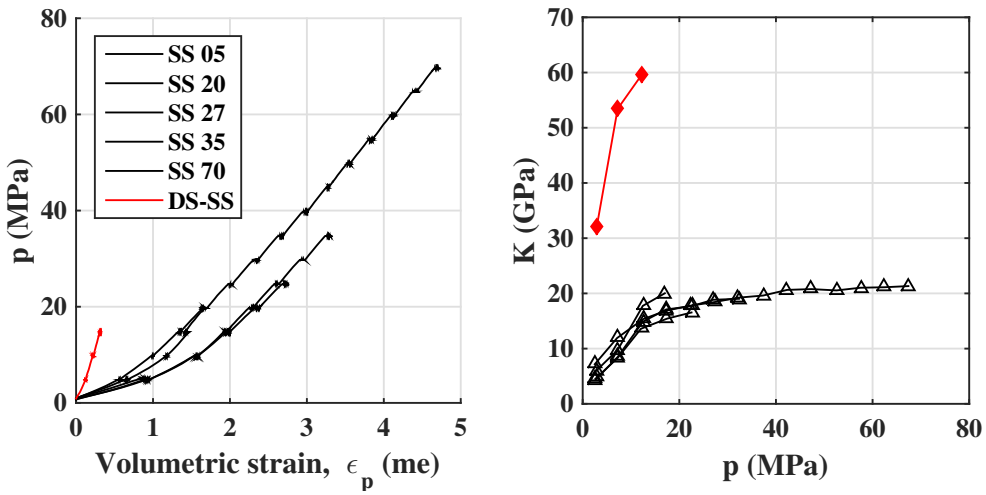

Figure D.2: **Hydrostatic stage of Dense Shale (red) triaxial experiments. Results from SS tests (black) are included for comparison.**

Results from the hydrostatic stage (DS-SS15) are shown in Figure D.2 and Table D.1. They revealed a much stiffer sample compared to SS tests, with an increase of +540% and +2,100% in Bulk's and Coupling moduli respectively. Also, note the positive sign of the J modulus, indicating higher deformation in the radial direction upon hydrostatic loading. This sample is very close to isotropy due to the high J value.

On the other hand, results from the triaxial stage (DS-SS05 and DS-SS15) are shown in Figure D.3 and Tables D.1 and D.2. Young's modulus of DS was found to be more than three times higher than SS moduli. Also, Poisson's ratio was estimated to be close twice the value found for SS samples. Moreover, intact strength was found to increase +180% (Figure D.3).

Finally, MSE results are shown in Figures D.5 and D.5. This test was conducted on DS-SS05 core (prior taken it to failure). Surprisingly, Young's modulus was found to initially

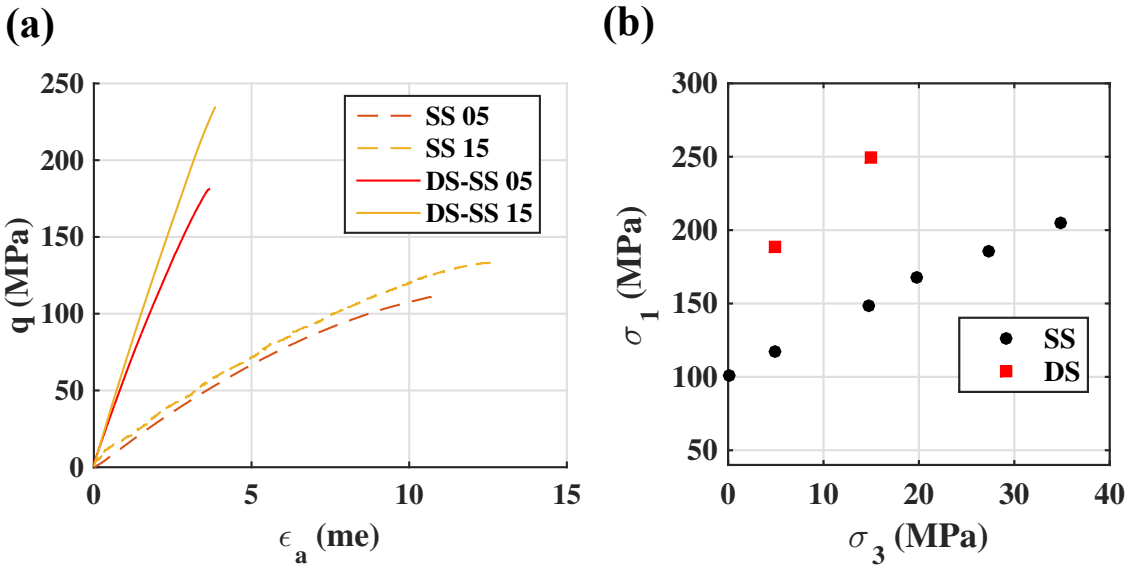

Figure D.3: **Triaxial stage of Dense Shale (solid lines and red squares) triaxial experiments. Results from SS test (dashed lines and black circles) are included for comparison. (a) Stress-strain curves and (b) Intact strength results.**

decrease with σ_3. We believe this reflects high material degradation that may have occurred in early stages. As expected, stiffness decreases within each stage upon deviatoric loading.

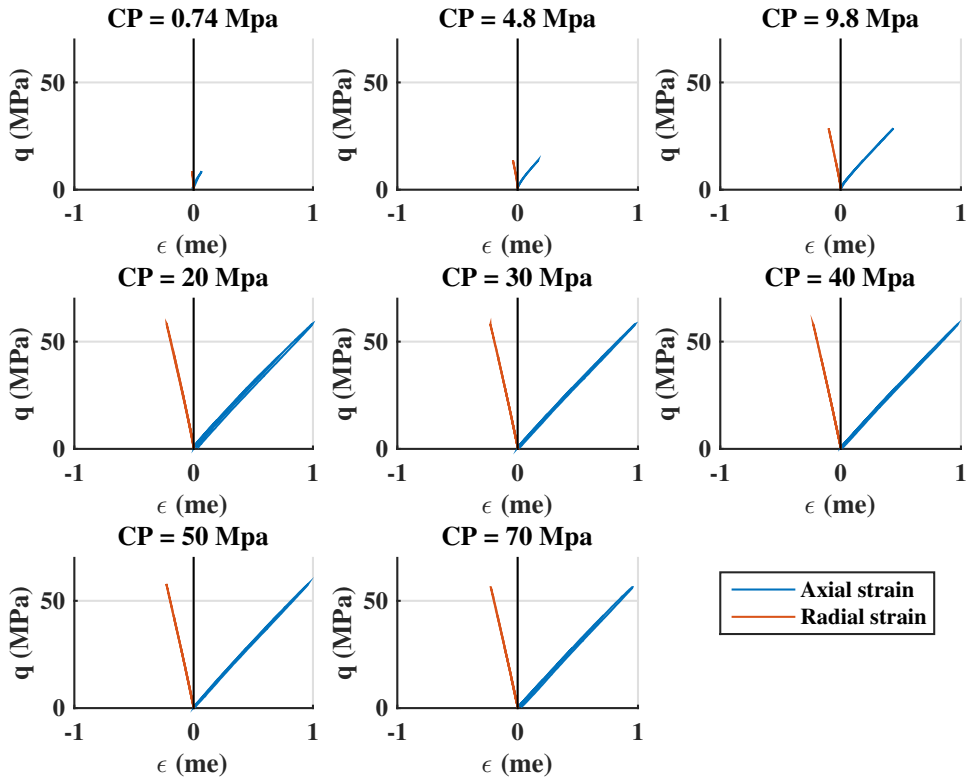

Figure D.4: **Elastic Multi-Stage test on Dense Shale. Stress-strain plots for all 8 stages (σ_3 = 0, 5, 10, 20, 30, 40, 50 and 70 MPa).**

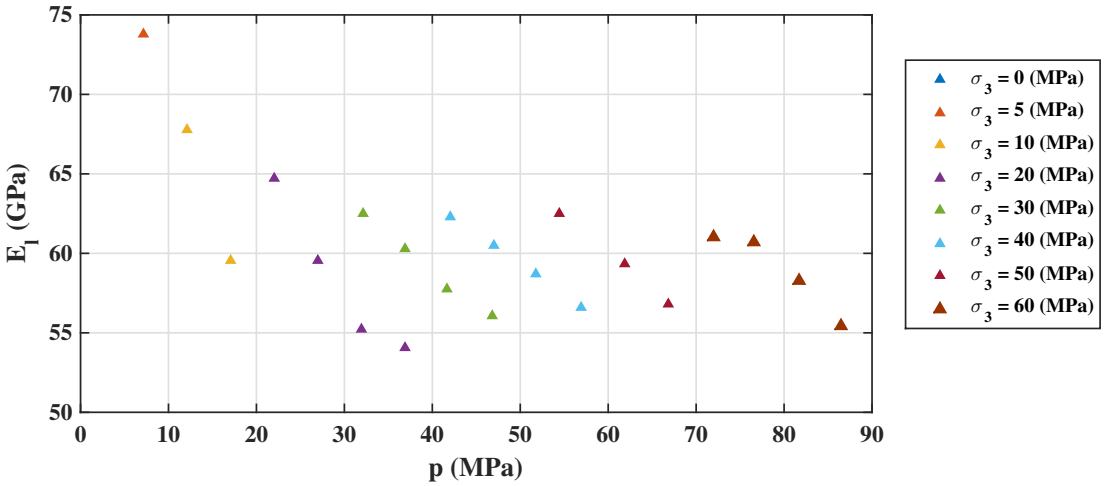

Figure D.5: **Variation of tangent stiffness of Dense Shale during MSE test. Each series represent the static Young's modulus estimated during 1^{st}-loading at different deviatoric stress levels. Stiffness decreases within each stage upon deviatoric loading. Note: E(σ_3 = 0 MPa) = 115 GPa is not shown.**

Appendix E: Deep Marcellus Shale

E.1 Introduction

These cores were retrieved by the US Department of Energy in the late 1970's as part of its Eastern Gas Shale Program. The well is located in Monongalia County, West Virginia. The cores are oriented perpendicular to the bedding, and come from an average depth of 7,500 ft. In this study they will be referred as Deep Marcellus Shale (DMS) cores (Figure E.1) .

Figure E.1: **Deep Marcellus Shale samples.**

The XRD test revealed that clay and quartz minerals are the major constituents of these samples (see Figure E.2 and Table E.1). DMS was found to have a very similar composition compared to Stage Game Lands 252 (SGL) samples tested in SS and MSE experiments.

Table E.1: **Deep Marcellus Shale Mineralogy Quantitative Analysis (WPPF). Bulk density was assumed based on mineralogy composition.**

ID	Depth (ft)	ρ (g/cc)	Mineralogy				
			Illite	Quartz	Pyrite	Calcite	Gypsum
DMS	7,500	2.58*	69.0	20.8	3.1	2.9	4.1

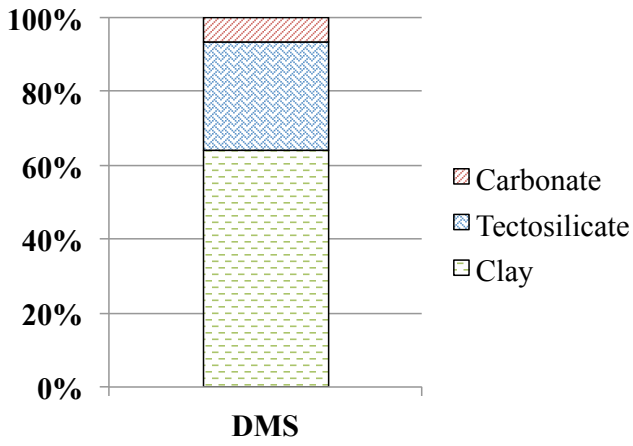

Figure E.2: **Mineralogy Composition of Deep Marcellus Shale.**

E.2 Methods

Due to the deteriorated nature of the DMS cores, only one subcore was successfully drilled. An elastic multi-stage triaxial test with ultrasonic velocities was performed on this core (σ_3 = 0-60 MPa). Then, the specimen was taken to reservoir conditions of pressure and

temperature, and a ductile creep test was conducted. Details and experiment objectives are summarized in Table E.2.

Table E.2: **Deep Marcellus Shale Experiment Summary**

CP (MPa)	0-70 MPa
T (^{o}C)	30, 60
Test	Elastic Multi-Stage + Ductile creep
Experimental parameters	Axial and Radial strains, Stress, Ultrasonic velocities
Experimental outcome	Creep behavior, Elastic moduli (E, ν, G, K), Pressure dependence

E.3 Results

E.3.1 Elasticity

Static Moduli

Results from MSE test are presented in Figures E.3 - E.9. Stress-strain plots for all 8 stages (σ_3 = 0 - 60 MPa) are shown in Figure E.3. A first inspection suggests significant non-linear behavior, and high plastic deformation (especially during the first stages). In addition, high (axial/radial) strains reveal that these samples are much more softer than SGL ones. This is probably due to the high deterioration of samples and the presence of horizontal fractures (recall that mineral composition is pretty similar among DMS and SGL samples) .

Figure E.4 compares elastic moduli of DMS upon loading-unloading-reloading cycles. Differences between 1^{st}-loading and unloading-reloading static moduli are important during first stages, but decreases with subsequent stages (same as observed with SGL

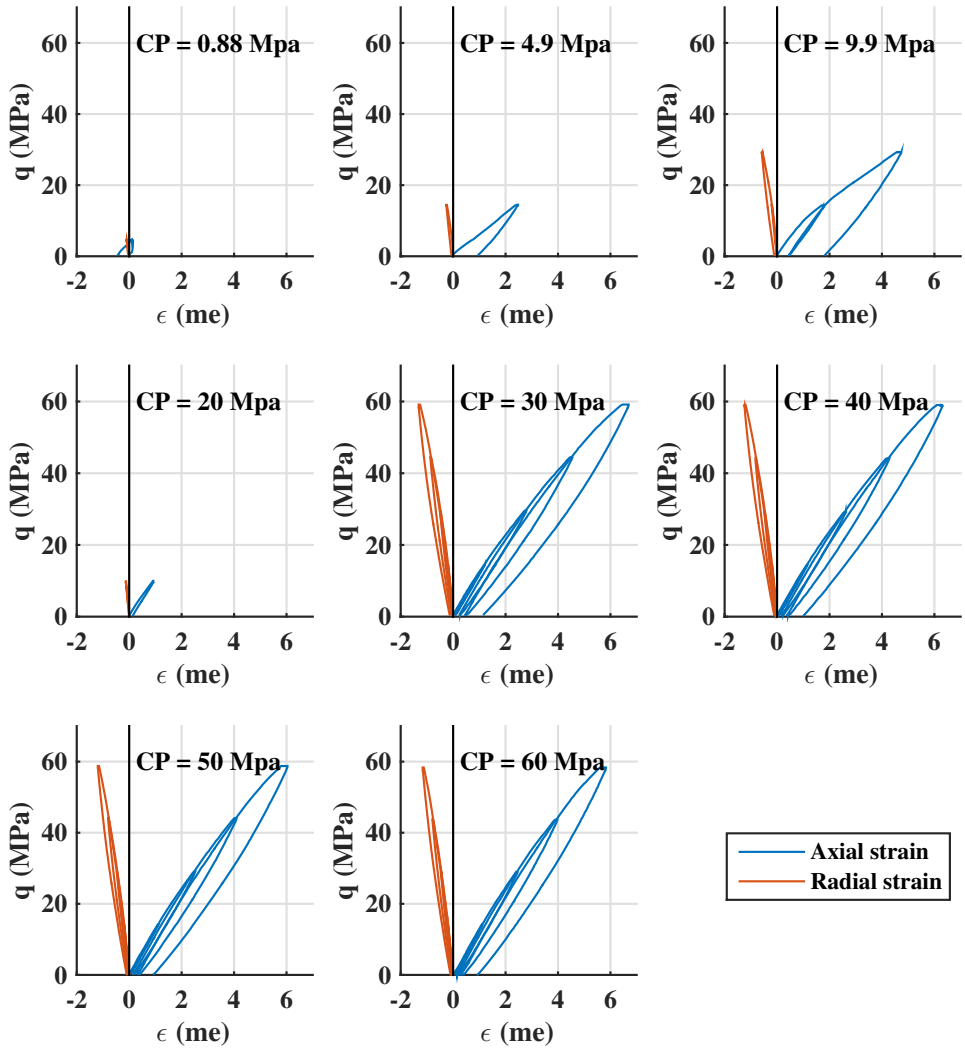

Figure E.3: **Elastic Multi-Stage test on Deep Marcellus Shale. Stress-strain plots for all 8 stages (σ_3 = 0 - 60 MPa).**

samples). Both Young's modulus and Poisson's ratio increase nonlinearly with confining pressure. While Young's modulus is a 43% lower compared with SGL one, Poisson's ratio was estimated to be a 12% higher.

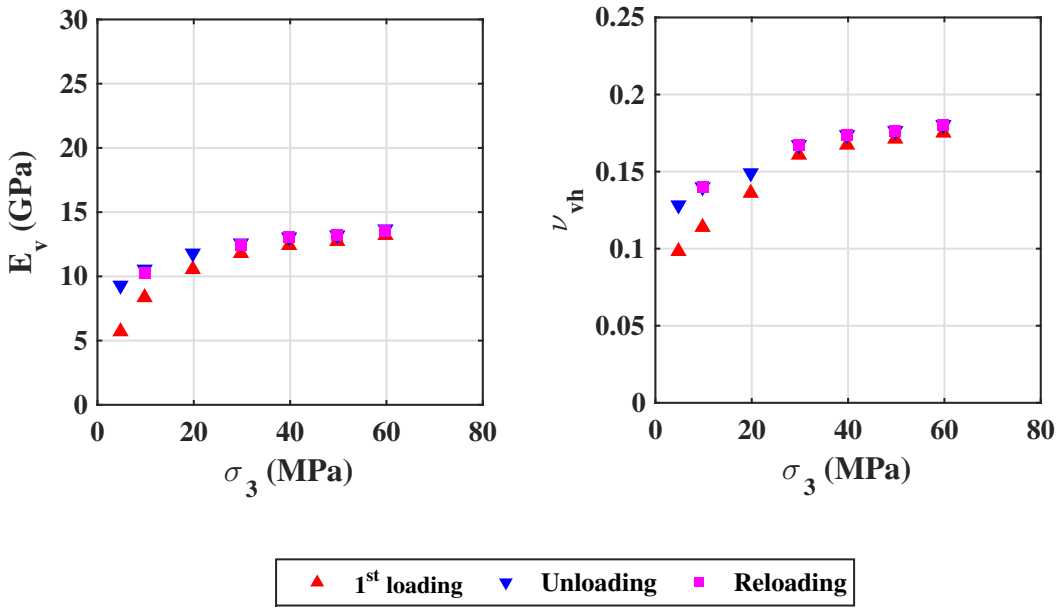

Figure E.4: **Elastic moduli of Deep Marcellus Shale from Elastic Multi-Stage test (MSE). (a) Young's modulus and (b) Poisson's ratio vs. confining pressure. 1st-loading and unloading parameters are estimated by linear regression from the first cycle of each stage (i.e. DS = 5-15 MPa), while reloading parameters correspond to initial moduli of the second cycle.**

On the other hand, Figure E.5 presents the variation of tangent stiffness of Deep Marcellus Shale during MSE test. Each series represent the static Young's modulus estimated during 1st-loading at different deviatoric stress levels. As in the SGL case, stiffness decreases within each stage upon deviatoric loading. Same conclusions can be derived in this case.

Dynamic Moduli

Rock cores are the principal sources for rock mechanical characterization. However, they are not always available since their extraction is complicated. Also, they do not fully

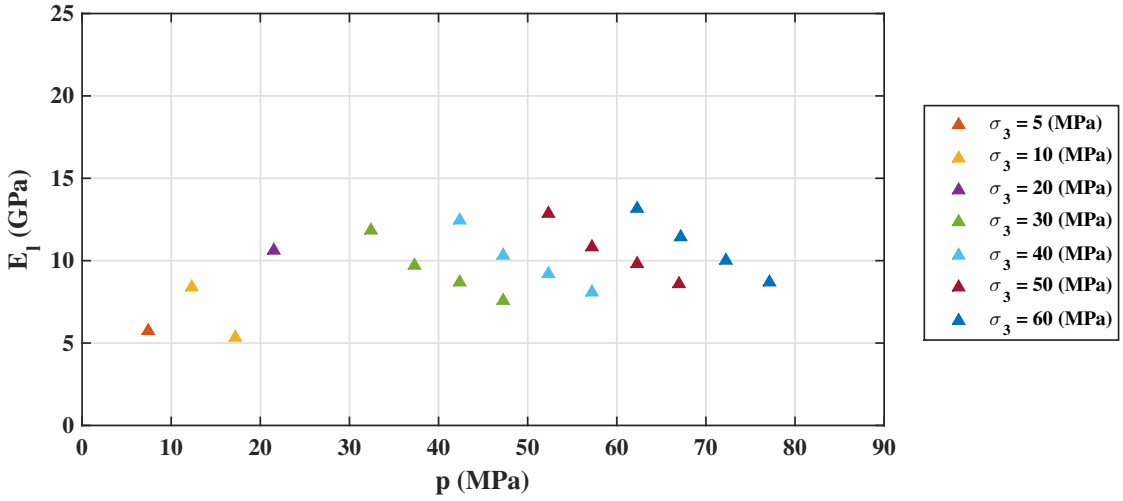

Figure E.5: **Variation of tangent stiffness of Deep Marcellus Shale during MSE test. Each series represent the static Young's modulus estimated during 1^{st}-loading at different deviatoric stress levels. Stiffness decreases within each stage upon deviatoric loading.**

represent the target formation as they come from discrete levels. Instead, in the field, elastic properties are often measured by dynamic techniques, which are capable to characterize large areas. During this experiment, P-wave (v_p) and cross-polarized S-wave (v_{s1} and v_{s2}) velocities were measured by ultrasonic transducers embedded in the coreholders (i.e. wave propagation perpendicular to the bedding). The frequency used for these dynamic measurements was 750 kHz.

In order to asses the impact of stress anisotropy on shale stiffness, ultrasonic velocities were measured at different stress levels during the MSE test. Figure E.6(a) presents v_p and both v_{s1} and v_{s2} ultrasonic velocities results under hydrostatic conditions. As expected, v_p is consistently higher (about 50%) than v_{s1} and v_{s2}, which are equal due to VTI symmetry. Figures E.6(b) and E.6(c) show dynamic Young's modulus (E_{iso}) and Poisson's ratio (ν_{iso})

respectively. Dynamic moduli were estimated from ultrasonic velocities by assuming complete isotropy.

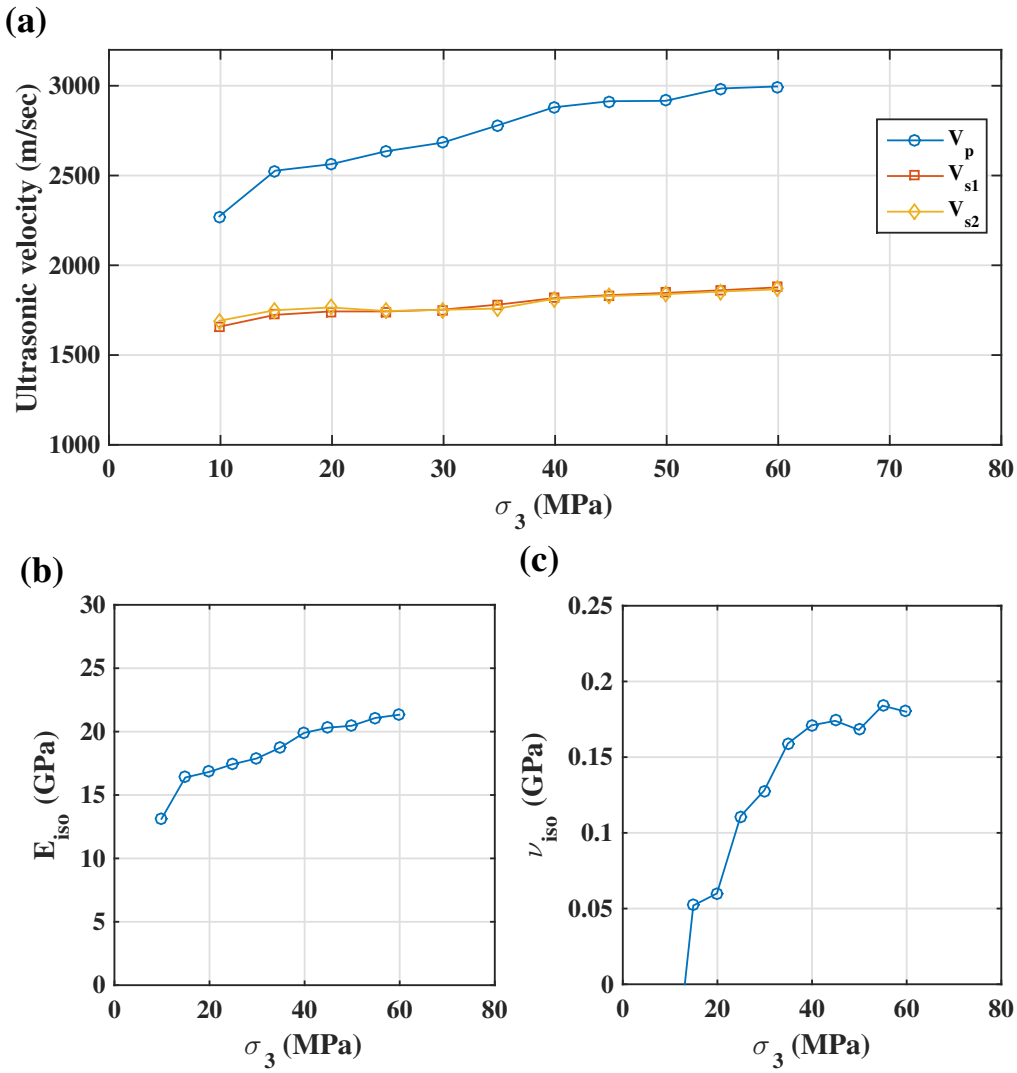

Figure E.6: **Dynamic moduli results: hydrostatic conditions. (a) Ultrasonic velocities propagating perpendicular to the bedding; (b) Young's modulus and (c) Poisson's ratio estimated from ultrasonic velocities. Isotropic conditions are assumed.**

By comparison of Figures E.6(b) and E.5, one can observe a significant difference between the elastic moduli obtained from acoustic velocities and those estimated from stress and strain measurements. While dynamic E_{iso} is consistently higher than static E_v (about 60%), dynamic ν_{iso} seems not to correlate static ν_{vh}. At early stages ν_{iso} is much smaller than ν_{vh}, increasing nonlinearly with confining pressure. At later stages, ν_{iso} and ν_{vh} agree pretty well to each other.

Elastic moduli measured from dynamic techniques are generally larger than those estimated by static means (Fjaer 2008). In this experiment, static moduli have been estimated from the slopes of stress-strain curves by linear regression (recall that the strain amplitude during static measurements is about 4 orders of magnitude larger than for the corresponding dynamic ones). Plasticity and nonlinear effects explain to some extent the difference between these moduli. In addition, the heterogeneous microstructure of the rocks is also related to this discrepancy (Fjaer 2008) .

On the other hand, Figure E.7 shows the impact of stress anisotropy on dynamic velocities and moduli. As expected, an increase in mean effective stress within each series (i.e. due to an increase in axial deviatoric load) resulted in ultrasonic velocity increase (Figure E.7(a)). This translate into an increase of dynamic Young's modulus upon application of deviatoric loading (Figure E.7(b)), which contrasts with static results shown in Figure E.5. Furthermore, stress anisotropy does not seem to have any impact on ultrasonic velocities in terms of mean effective stress. Ultrasonic velocities increase in the same manner with mean effective stress independently the latter is due to increase in deviatoric load or confinement.

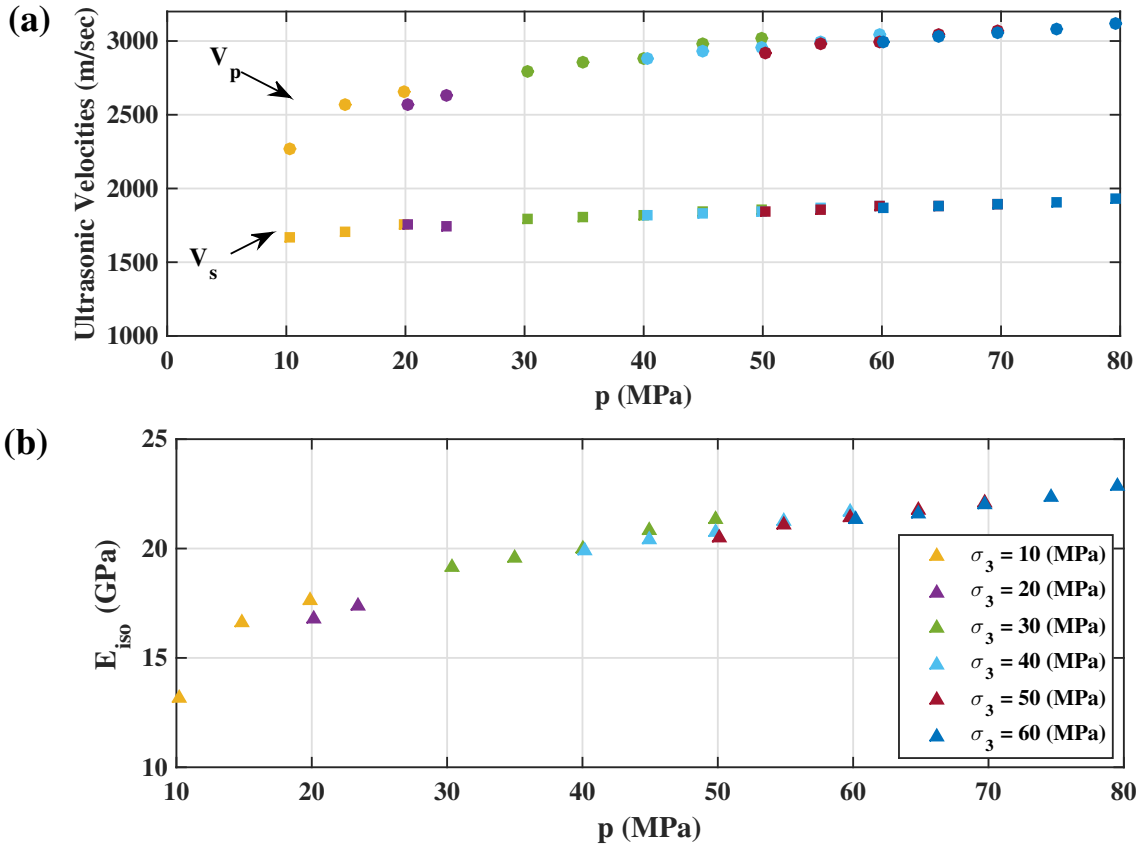

Figure E.7: **Dynamic moduli results: impact of stress anisotropy. (a) Ultrasonic velocities propagating perpendicular to the bedding (v_s represents the v_{s1} and v_{s2} average). (b) Young's modulus estimated from ultrasonic velocities. Isotropic conditions are assumed.**

Finally, we should acknowledge that significant plastic deformation took place during both MSE and Creep tests. With this in mind, two additional MSE test were performed after the Ductile Creep test in order to further investigate the pure elastic properties of the DMS. Dynamic results are shown in Figures E.8 and E.9.

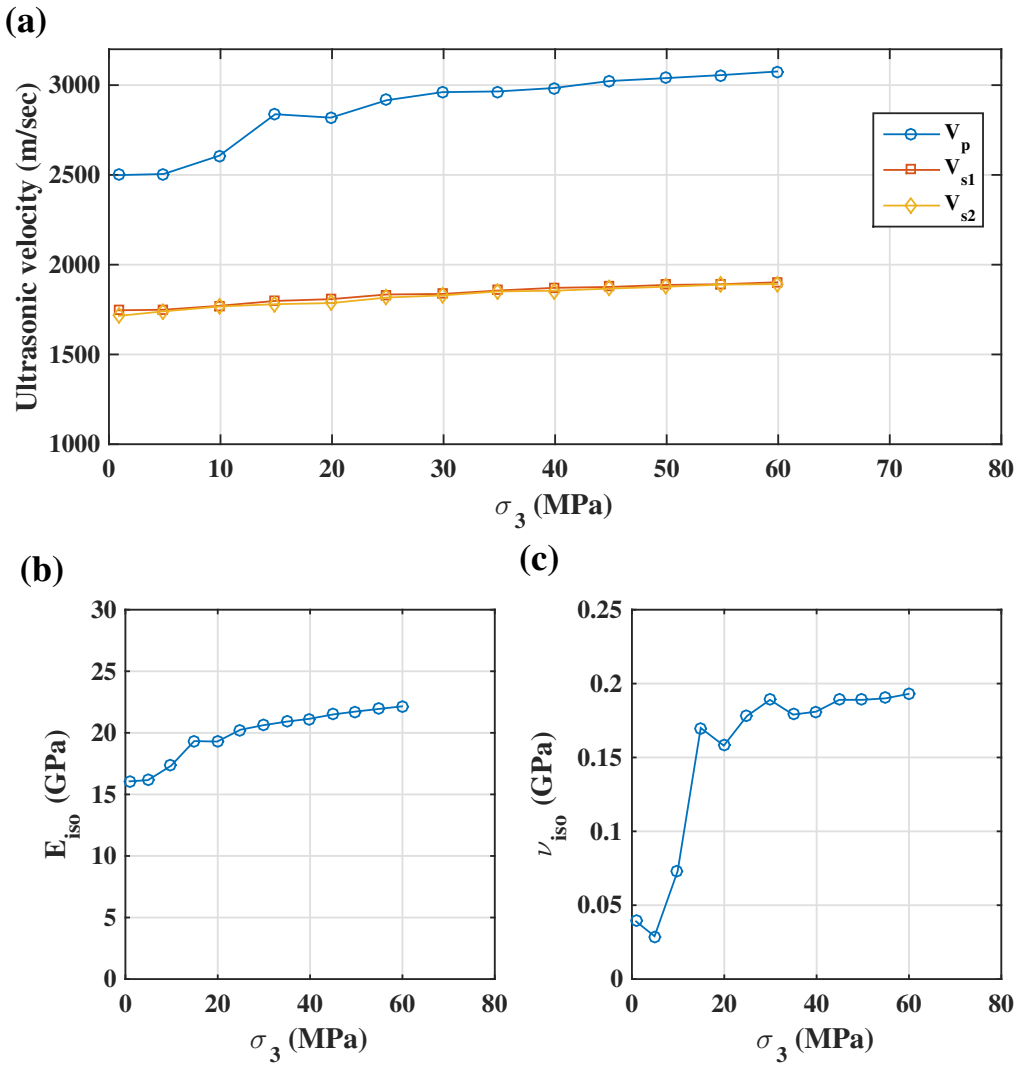

Figure E.8: **Dynamic moduli results: hydrostatic conditions (second MSE). (a) Ultrasonic velocities propagating perpendicular to the bedding; (b) Young's modulus and (c) Poisson's ratio estimated from ultrasonic velocities. Isotropic conditions are assumed.**

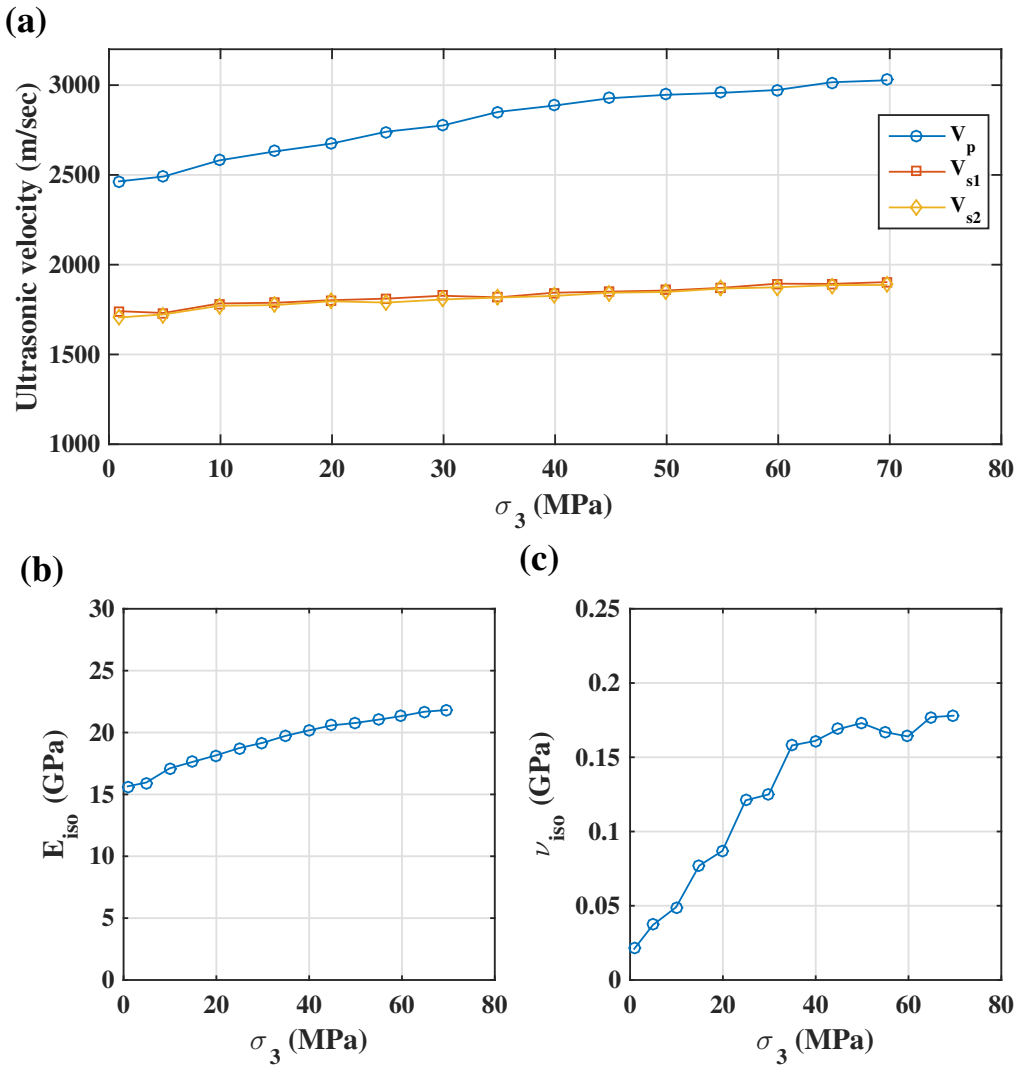

Figure E.9: **Dynamic moduli results: hydrostatic conditions (third MSE). (a) Ultrasonic velocities propagating perpendicular to the bedding; (b) Young's modulus and (c) Poisson's ratio estimated from ultrasonic velocities. Isotropic conditions are assumed.**

E.3.2 Ductile Creep

After finishing the first elastic multi-stage, the DMS sample was taken to reservoir conditions of pressure and temperature. Based on well logs, confining pressure and

temperature were estimated to be 30 MPa and 50 ^{o}C respectively. Thermal consolidation stage was extended for approximately 15 hours in order to dissipate previous viscoelastic effects from MSE test. Once equilibrium was reached, deviatoric load was applied following the same stress path as shown in Figure C.1.

Figure E.10 shows the strain response of DMS during triaxial stage. Significant discrepancy was observed between both axial strain readings.

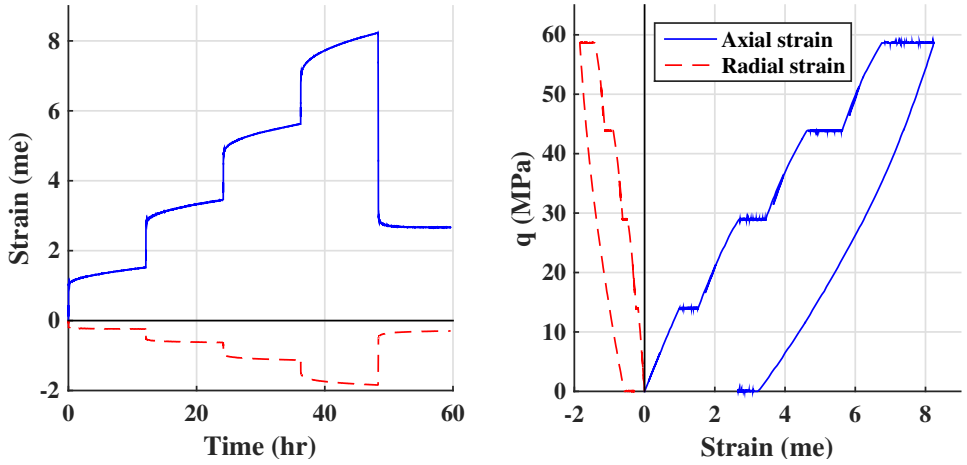

Figure E.10: **Ductile Creep of Deep Marcellus Shale. Triaxial Stage**

Figure E.11 presents the 12-hour creep at different deviatoric stress steps for the Deep Marcellus Shale sample.

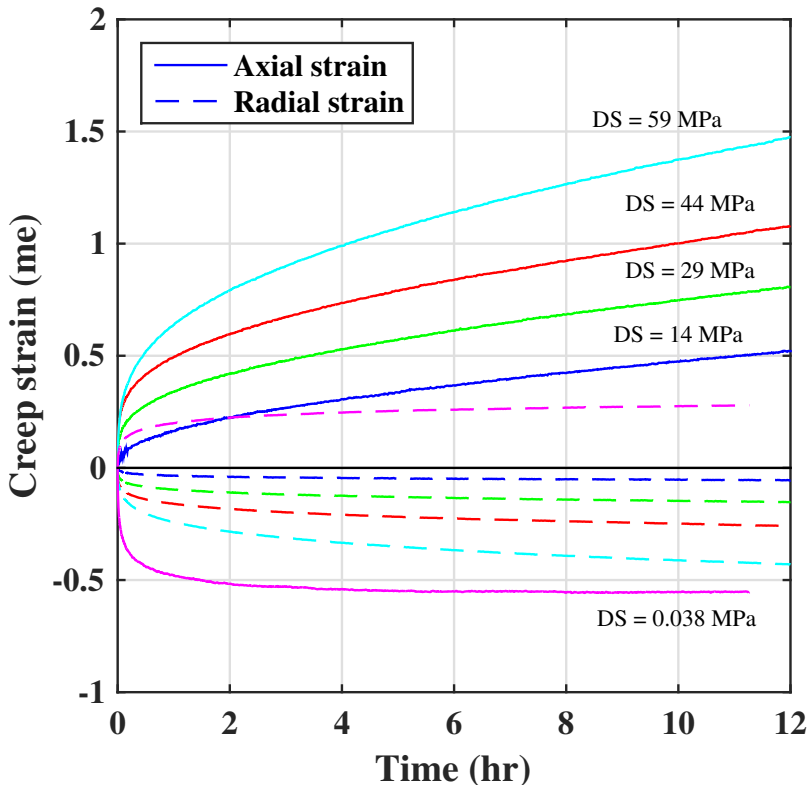

Figure E.11: **Ductile Creep of Deep Marcellus Shale. Time-delay behavior**